Modified Mesoporous Supported Ni(Co)Mo-S For Hydrodesulfurization Applications

BY

Abdulkadir Tanimu

A Dissertation Presented to the

DEANSHIP OF GRADUATE STUDIES

KING FAHD UNIVERSITY OF PETROLEUM & MINERALS

DHAHRAN, SAUDI ARABIA

In Partial Fulfillment of the
Requirements for the Degree of

DOCTOR OF PHILOSOPHY

In

CHEMISTRY

MAY, 2019

KING FAHD UNIVERSITY OF PETROLEUM & MINERALS

DHAHRAN- 31261, SAUDI ARABIA

DEANSHIP OF GRADUATE STUDIES

This thesis, written by **Abdulkadir Tanimu** under the direction of his thesis advisor and approved by his thesis committee, has been presented and accepted by the Dean of Graduate Studies, in partial fulfillment of the requirements for the degree of **DOCTOR OF PHILOSOPHY IN CHEMISTRY.**

Dr. Khalid R. Alhooshani
(Advisor)

Dr. Khalid R. Alhooshani
Department Chairman

Dr. Abdulaziz A. Al-Saadi
(Co-Advisor)

Dr. Salam A. Zummo
Dean of Graduate Studies

Dr. Mazen Khaled
(Member)

9/5/19
Date

Dr. Musa M. Musa
(Member)

Dr. Syed Ali
(Member)

Dedicated to my family members

ACKNOWLEDGMENTS

All praise be to Allah, Lord of the world. The most beneficent the most merciful. You alone we worship and you alone we ask for assistance. May His peace and blessings be onto our Prophet, the seal of prophets, Muhammad S.A.W, his household, his companion and those that follow their path until the last day.

My special appreciation goes to my Supervisor, Dr. Khalid R. Alhooshani, whom through his expertise, excellent human relationship and high moral standard, I was able to complete this PhD program while enjoying my stay in the research group. Indeed, the program was never boring courtesy of the good leadership style demonstrated by the Supervisor. Similarly, the contributions of the co-advisor, Dr. Abdulaziz A. Al-Saadi and committee members: Dr. Mazen Khaled; Dr. Musa M. Musa and Dr. Syed Ali toward successful completion of this program, particularly in preparing the dissertation are very well appreciated.

My sincere appreciation also goes to Dr. Saheed A. Ganiyu, with whom I have learnt good part of the catalyst synthesis and characterization techniques, and Dr. Sajid Jillani, a friend and colleague for his support and advice. I would like to extend my appreciation to all our group members for their cooperation, support, patience and understanding. Sincerely, you mean a lot to me and I owe you for that.

The journey to M.S and PhD (Chemistry) may remain a dream without the support of the Kingdom of Saudi Arabia, through the King Fahd University of Petroleum and Minerals. This kind gesture will forever remain in my memory, may Allah continue to bless the Kingdom of Saudi Arabia.

The warm and welcoming nature of the Nigerian Community in KFUPM is something I found really amazing. I must confess that the community is a home away from home. To all the Nigerians and other African nationalities staying in KFUPM, I say a big thank you for your continuous support.

Finally, I would like to express my profound gratitude to my family, both immediate and extended for their continuous support and prayers. My parents, sisters and brothers, I thank you all. And to my darling wife, my daughter and son, you are indeed part of this struggle, you stood by me through all the huddles and painful moments, you were so patient with me and you were so much supportive. Most importantly, I am glad you are alive to witness this success.

I thank everyone for being part of my success.

TABLE OF CONTENTS

LIST OF TABLES

LIST OF FIGURES

LIST OF ABBREVIATIONS

SBA-15	:	Santa Barbara Amorphous-15
HDS	:	Hydrodesulfurization
HYD	:	Hydrogenation
DDS	:	Direct desulfurization
TEOS	:	Tetraethyl orthosilicate
$Ce(i\text{-}PrOH)_4$	:	Cerium isopropoxide
DBT	:	Dibenzothiophene
THDBT	:	Tetrahydrodibenzothiophene
MDBT	:	Methyldibenzothiophene
XRD	:	X-ray Diffraction
TPR	:	Temperature-Programmed Reduction
TPD	:	Temperature-Programmed Desorption
XPS	:	X-ray photoelectron spectroscopy
FESEM	:	Field Emission Scanning Electron Microscopy
MSI	:	Metal Support Interaction
TEM	:	Transmission electron microscopy
FTIR	:	Fourier transform infra-red

ABSTRACT

Full Name : [Abdulkadir Tanimu]

Thesis Title : [Modified Mesoporous Supported Ni(Co)Mo-S for Hydrodesulfurization Applications]

Major Field : [Chemistry]

Date of Degree : [May 2019]

Hydrodesulfurization (HDS) of fuel is an important aspect of hydroprocessing technology for clean fuel production and other applications involving catalytic converters. Stringent environmental regulations have put the HDS of transportation fuels as urgent necessity amongst the industrial processes in the petroleum refining. Of the areas of emphasis in the HDS catalyst development is the design and development of large surface area mesoporous support that will have the optimum acidity, metal support interaction and chemical and thermal stability. The research gap in this area lies in developing or modifying the support properties to meet the required criteria for efficient and long lasting HDS catalyst. In this work, series of HDS catalysts have been developed through support modifications such as incorporation of heteroatom(s) to the framework of SBA-15 and the effect of the support modifications were studied on the HDS of dibenzothiophene in both model fuel and in commercial diesel. The modification of SBA-15 with ceria at 1-10 wt.% loading and subsequent impregnation of Co and Mo gave an appreciable conversion of above 99 % at 2.5 wt. ceria loading. The experimental and modeled kinetic parameters have demonstrated the role of ceria in the catalyst conversion and product selectivity. Subsequent modification of SBA-15 with ceria and zirconia biheteroatoms and loading of Ni and Mo presented higher DBT conversion in commercial diesel which was correlated to the electronic effect

due to the biheteroatoms modification. The last part of this study was dedicated to developing a greener approach for the sulfidation of the metal oxide catalyst. The HDS catalyst is inactive when in the oxide form and the general approach to sulfidation is considered unsafe due to the use of hydrogen disulfide. Therefore, the use of (3-Mercaptopropyl)trimethoxysilane as sulfidation source in addition to the silica support is proposed. This approach has eliminated the direct use of a highly toxic gas, hydrogen disulfide.

ملخص الرسالة

الاسم الكامل: عبدالقادر تانيمو

عنوان الرسالة: Ni(Co)Mo-S المعالج ذو المسامات البينية المدعوم لتطبيقات إزالة الكبريت بالهدرجة

التخصص: كيمياء

تاريخ الدرجة العلمية: مايو 2019

تعتبر ازالة الكبريت بالهدرجة من الوقود من اهم الجوانب من المعالجات الحرارية لإنتاج وقود نظيف وتطبيقات أخرى تتعلق بالمحولات الحفزية. بسبب اللوائح البيئية الصارمة تم اعتبار ازالة الكبريت بالهدرجة لوقود النقل ذو أهمية قصوى وسط العمليات الصناعية في عمليات تنقية تكرير البترول. من اهم نواحي تطوير الحفازات الخاصة بعملية ازالة الكبريت بالهدرجة هو تطوير مواد داعمة ذات مساحة سطح عالية ومسامات بينية والتي ستوفر حمضية، ترابط بين المعدن والمادة الداعمة و ثباتية كيميائية وفيزيائية مثلى. وتمكن فجوة البحث في هذا المجال في تطوير او تعديل خواص المادة الداعمة لتقابل الخواص المطلوبة لحفاز ذو كفاءة وثبات عالي. في هذا البحث، سلسلة من الحفازات تم تطويرها عن طريق تعديل المادة الداعمة بإضافة ذرة او ذرات مختلفة لاطار SBA-15 وتمت دراسة تاثير المعالجة للمادة الداعمة بإزالة الكبريت بالهدرجة للدايبنزوثيوفين في كلا عينة ديزل نموذجية وعينة تجارية. معالجة SBA-15 بالسيريا بنسبة وزنية 1-10% ومن ثم ادخال ال Co و Mo اعطى نسبة إزالة مقدرة و هي99 % بنسبة وزنية 2.5% للسيريا. تم استخدام الحركية عمليا ونظريا لشرح دور السريا في تحويل وانتقائية الحفاز. تم عمل معالجة لاحقة ل SBA-15 بذرتي السريا والزركونيا و تحميل الNi و Mo أظهرت نسبة تحويل اعلى ل DBT في عينة ديزل تجارية ويعزى ذلك للأثر الالكتروني بسبب المعالجة بإضافة الذرتين المختلفتين. الجزء الأخير من هذه الدراسة كرس لتطوير طريقة صديقة بيئا لإضافة الكبريت لحفاز لأوكسيد المعدن. حفاز ازالة الكبريت بالهدرجة يكون غير فعال في هيئة الأوكسيد والطريقة العامة لاضافة الكبريت غير امنة بسبب استخدام الهيدروجين دايسلفايد. لذلك تم استخدام (3-ميركابتوبروبايل) ترايميثوكسي سيلين كعامل إضافة كبريت لمادة السيليكا الداعمة. هذه الطريقة الغى الحوجة للاستخدام المباشر لغاز هيدروجين دايسلفايد عالي السمية.

CHAPTER 1

INTRODUCTION

1.1 Background Information

There is currently an apparent increase in demand for fossil fuel energy in some countries, but the need for mitigating the effects of the use and acquisition of non-renewable energy sources on the environment has gained global attention [1–3]. The increased demand for fossil fuels is a result of continuing increase in population, especially in the developing countries where the energy options are limited, and the global interest in offsetting and/or eliminating the effects of burning these fossil fuels highlights the severity in consequence of large scale industrial and automobile emissions. Such emissions are leading to climate change, more specifically global warming [4], but they also pose many risks on the environment and human health [5]. For example, sulfur (iv) oxide, a major emission of combusted fuel, can cause severe respiratory and other several health problems when inhaled, and in the atmosphere, it forms the acid rain which can harm sensitive ecosystems [5]. In addition to being linked to health and environmental problems, sulfur in fuel is known to cause damage by deactivating the reforming catalysts and resulting in the corrosion of pipelines, pumps, and refinery equipment [6]. Due to these undesirable consequences, environmental regulations have prompted restraining the level of sulfur in the fuel, and a recent regulation by the European Emission Standard (Euro VI) targeted

zero sulfur in the transportation fuel [7]. With so many countries gradually adopting this policy and transiting to zero sulfur transportation fuel (**Fig. 1.1a and b**), the refineries are being forced to find ways to meet the newly increasing demand for ultra-low sulfur fuel, which ultimately requires that the refineries invest in research. Recently, Honeywell, an oil and gas technology inventor and manufacturer, developed an ULTIMet™ catalyst that was designed to address the challenge of the refineries by having more active sites for chemical reaction, thus resulting in an increased hydrotreating performance [8]. According to the company, the catalyst can as well work in-tandem with the conventional hydrotreating catalyst in the hydrotreating plant, thus saving refineries the cost of redesigning an additional hydrotreating unit for ultra-low sulfur fuel production. Though catalyst producers like Honeywell and ExxonMobil have achieved a great milestone in catalysts' designs, their technology is mostly trademarked or patented, which make access to vital scientific information quite difficult. We do know that in the hydrotreating plants of most refineries, the technology of removing sulfur from the transportation fuel involves hydrodesulfurization (HDS) [9]. However, other methods such as oxidative desulfurization, supercritical water desulfurization, and adsorptive desulfurization [10] are still used by a few refineries, albeit less frequently than HDS.

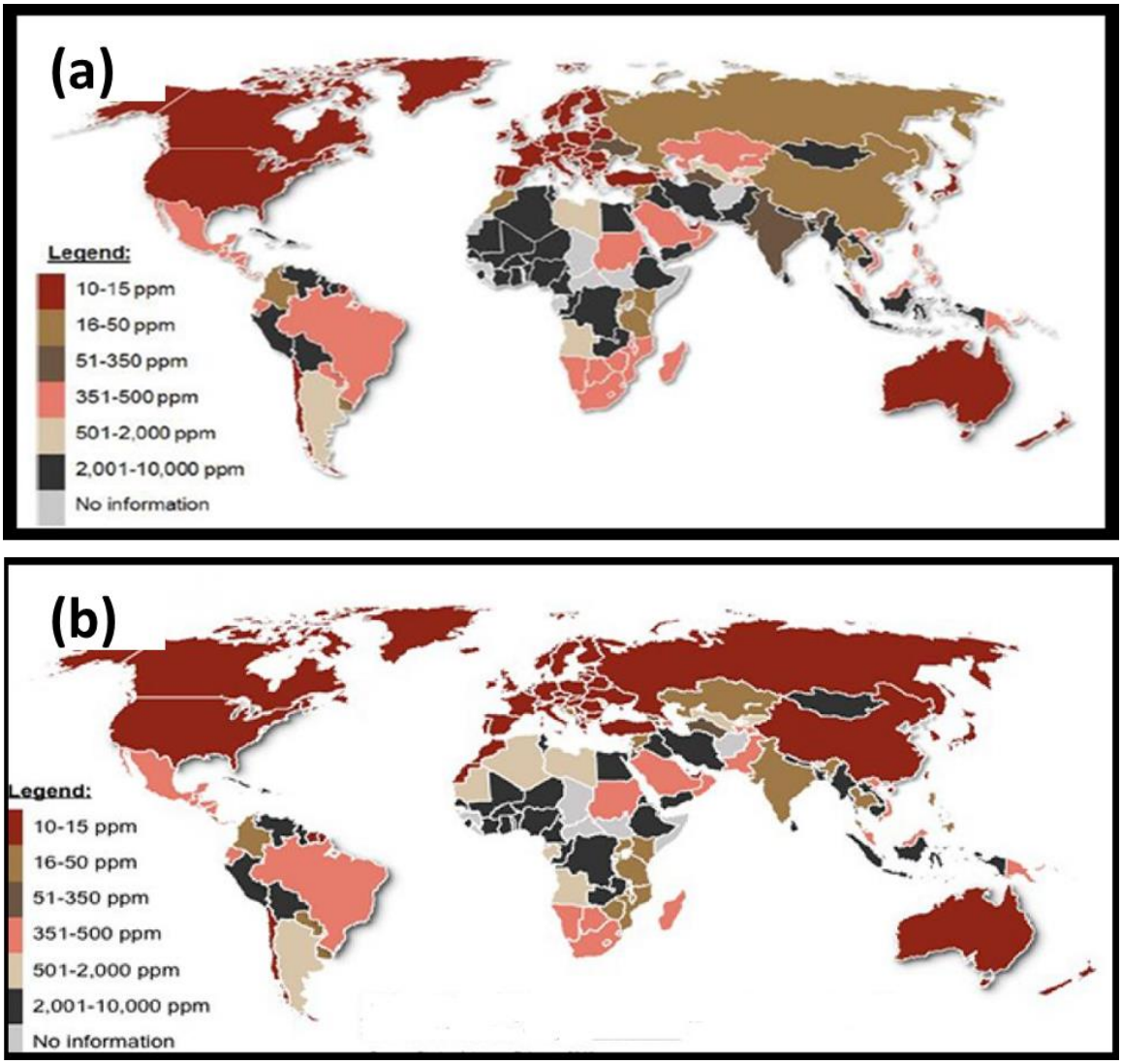

Figure 1. 1: Worldwide on-road diesel sulfur limit, sourced from Stratas Advisors, (a) October, 2015 and (b) February, 2018 [11].

Although HDS is the most commonly used chemical technology for removing organic sulfur from crude oil and transportation fuel such as gasoline, jet fuel, and diesel [12], it is often considered pricey. The HDS technology is known to be financially tasking in terms of its operational conditions, which require an active solid catalyst as well as high temperature and hydrogen gas pressure conditions. Though HDS technology has its financial drawbacks, its desulfurization performance is unmatched by other desulfurization technologies. Because of its high efficiency of removing sulfur, refractory sulfur compounds such as dibenzothiophene (DBT), 4-methyldibenzothiophene (4-MDBT), 4,6-dimethyldibenzothiophene (4,6-DMDBT), and benzonaphthothiophene (BNT) (**Fig. 1.2**) which are mostly found in heavy gas oil and vacuum gas oil can be treated easily with a highly robust HDS catalyst. Since the crude oil reserve in many parts of the world is becoming heavy nowadays, the demand for highly robust HDS catalysts has dramatically increased. Additionally, the continuous emergence of alternative energy supply sources (e.g. biofuel and solar energy) has contributed to the drop in the value of crude oil in the international market; therefore, cheaper but efficient HDS technologies are continuously being sought.

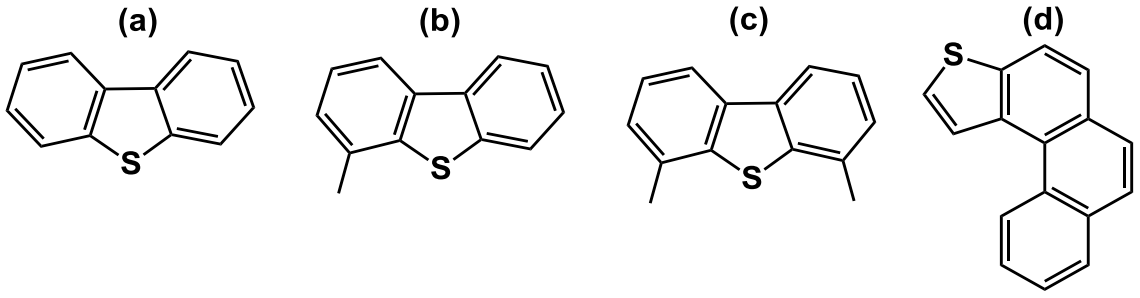

Figure 1. 2: Some refractory sulfur compounds: (a) dibenzothiophene; (b) 4-methyldibenzothiophene; (c) 4,6-dimethyldibenzothiophene; (d) benzonaphthothiophene

1.2 Mechanism of Hydrodesulfurization

The mechanism of hydrodesulfurization reaction of DBT and alkyl DBT has been well established [13], and typically occurs via two main parallel pathways: direct desulfurization (DDS) and hydrogenation (HYD) (**Fig.1.3**). The former involves a single step C-S bond cleavage to form biphenyl while the later involves multi-steps hydrogenation of one of the benzene rings of the DBT to form tetrahydrodibenzothiophene (THDBT) which later undergoes C-S bond cleavage and subsequently form the desulfurized cyclohexyl benzene product. Previous studies have shown that the DDS pathway is most preferred especially for the unsubstituted DBT [14–17]. The alkyl substituted DBT such as 4,6-DMDBT suffers the steric hindrance effect, due to the alkyl substituent, which slow down the end-on adsorption of the thiophenic sulfur on the catalytic active sites and consequently decrease its HDS reaction. And in the case of side-on adsorption interaction involving the π-electrons of the aromatic ring, it has been argued that the substituent effect slows down the C-S bond cleavage [18,19]. Furthermore, it has been reported that the alkyl substituted DBT has more preference for the HYD pathway due to the relative ease of partial saturation of one of the biphenyl rings which warrant the isomerization of the alkyl substituent and the hitherto sterically hindered sulfur becomes more accessible for adsorption (**Fig. 1.4**).

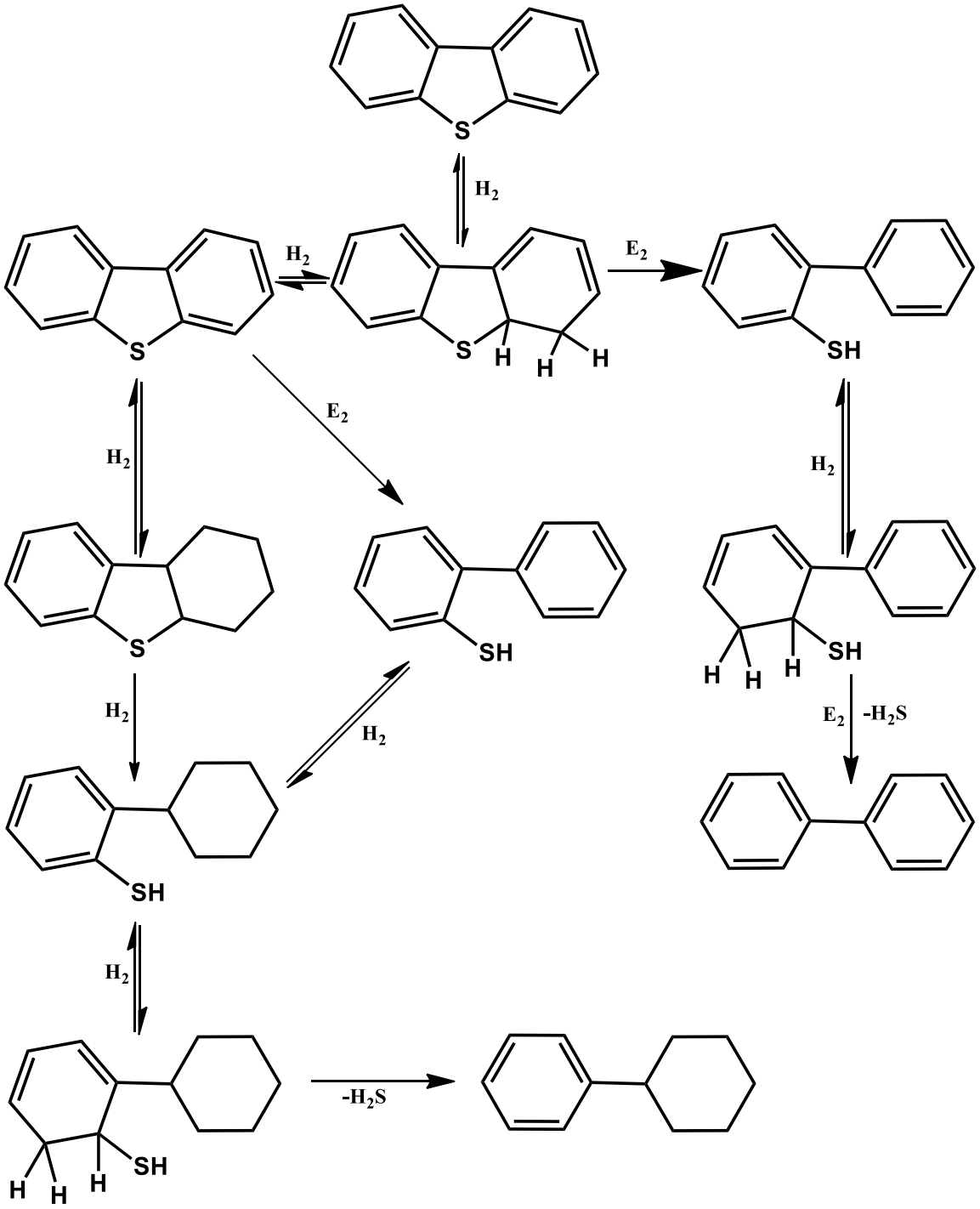

Figure 1. 3: The various steps of HDS of DBT through both DDS and HYD pathways. E2 is a C-S bond cleavage through an β-elimination process involving sulfur anion as basic site [20].

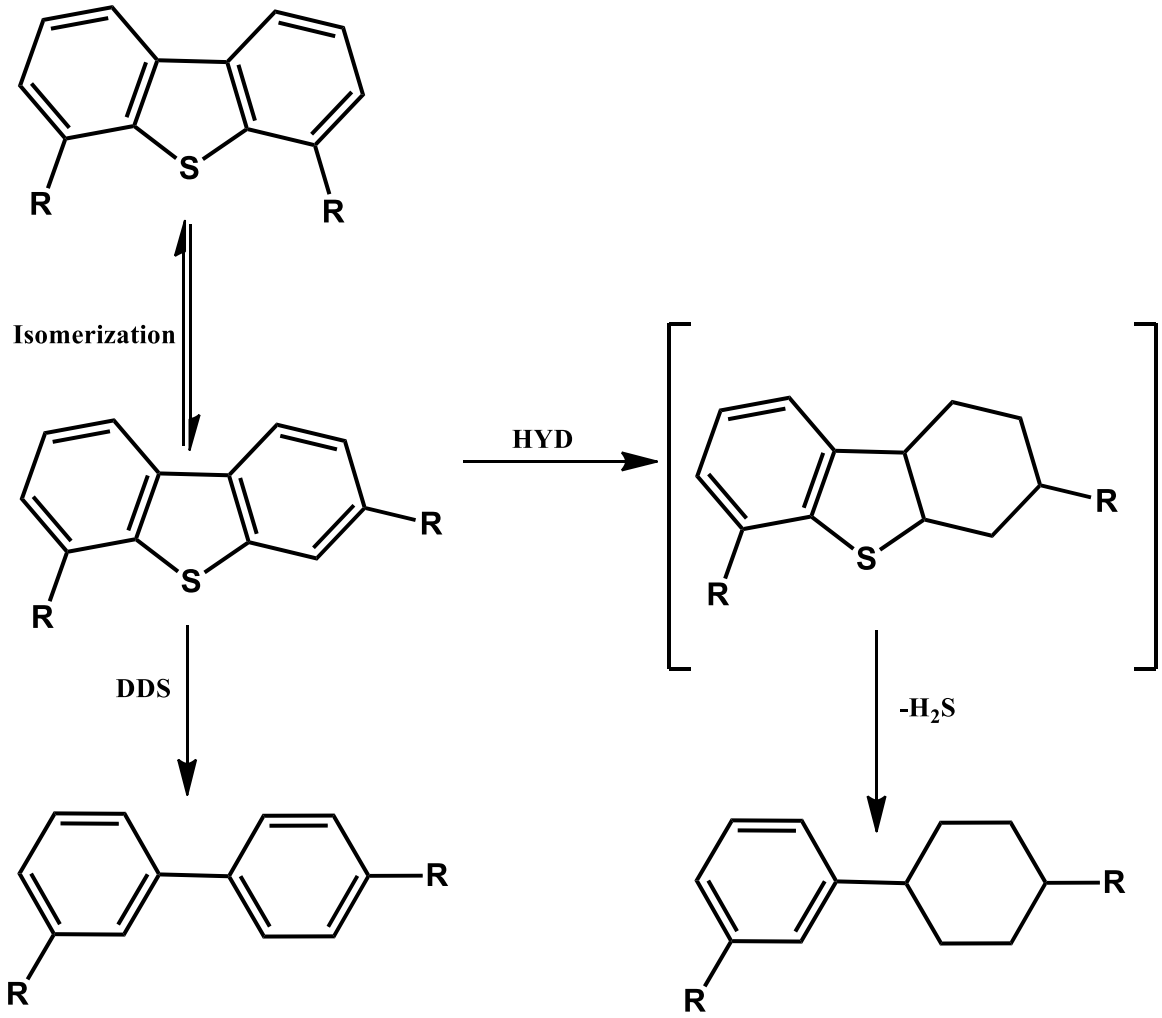

Figure 1. 4: Transformation of 4,6-DMDBT through isomerization route over acid containing hydrotreating catalysts [20].

1.3 Hydrodesulfurization Catalysts

The predominant metals often used as the active species in the HDS catalyst design are Co(Ni)Mo(W). These active species have been used for more than a century as bulk catalyst and later as a supported catalyst in an effort to cut cost and increase the active metals dispersion and HDS activity. Interestingly, the approach to HDS has somewhat drastically evolved through the years although the active species have not been able to be completely replaced. We now have a better grasp on the role that active sites play in the reaction pathway and product selectivity. These advances have enabled development of interesting synthesis strategies that yielded unique supports and minimized the cumbersome nature and the large energy consumption that are both associated with the synthesis steps.

1.4 Supported Hydrodesulfurization Catalysts

One of the bold steps taken when specializing catalysts is to minimize the cost of catalyst production and increase catalyst activity by using exceptionally cheap yet highly mesoporous active metals supports, such as alumina and silica [21–25]. The supports must have properties suitable for catalytic application, such as 1) mechanical strength to minimize catalyst attrition [26–29], 2) a large surface area to enhance fast interaction of active phases with the organo-sulfur reactants [30,31], 3) an availability of acidic sites to improve the dispersion of active metals [32–34], and 4) moderate metal-support interaction for easy reduction and sulfidation of the active phases [35,36]. Based on the required support properties of HDS catalysis, catalyst producers have since aligned their interest more on alumina support. Even though it deactivates quickly due to the strong metal-

support interaction, it has not been easily replaced because of its unique mechanical strength and textural properties [37–39]. The main disadvantage of alumina support is the strong metal-support interaction that exist between Mo oxides and alumina, which results in the formation of strong tetrahedral molybdenum oxide that coordinate tetrahedrally mainly with other Mo oxides monolayers [40]. Unlike the octahedral molybdenum oxide that is easily reduced and sulfided, the strongly bounded tetrahedral molybdenum oxides tend to resist reduction and sulfidation [41]. This has strongly motivated researchers both in refineries R&D and in academics to search for a better HDS catalyst support that would have moderate metal-support interaction in addition to excellent textural properties and mechanical and thermal stabilities.

1.5 Research Objectives

The search for highly stable supported HDS catalyst that has the required surface acidity, metal support interaction, textural and mechanical properties is on-going business. The current research trend is toward modification of the SBA-15 framework via incorporation of heteroatoms such as Al, Ti and Zr. The support modification increases the metal support interaction in SBA-15 from weak to moderate and also enhance the support acidity. The acidity of the catalyst inhibits it's poisoning by H2S and promote the isomerization of alkyl group in sterically hindered sulfur compounds. This dissertation focuses on the modification of SBA-15 using ceria heteroatom, and a combination of ceria and zirconia heteroatoms. The role of the heteroatom(s) modification on the SBA-15 support was studied in the HDS of dibenzothiophene after the incorporation of Ni(Co)Mo-S as the active metals. The study was also extended to new strategy for the sulfidation of supported

metal oxide catalyst in a bid to eliminate the direct use of toxic chemicals such as H_2S or CS_2. The catalysts' physico-chemical properties are determined by different characterization techniques such as; X-ray diffraction (XRD), Raman spectroscopy, N_2-physisorption, temperature programmed techniques by desorption and reduction (TPR and TPD), Fourier transform infra-red (FTIR) and FTIR-pyridine, X-ray photoelectron spectroscopy (XPS), Scanning electron microscopy (SEM), and transmission electron microscopy (TEM). The highlighted objectives are studied and reported under each chapter of this dissertation;

Chapter 3: Synthesis, application and kinetic modeling of CeO_x-Si-CoMo catalysts for hydrodesulfurization of dibenzothiophene.

Chapter 4: Synergy of ZrO_x-CeO_y on active sites formation of NiMoS catalyst supported on SBA-15 for hydrodesulfurization of dibenzothiophene in diesel.

Chapter 5: A greener and efficient approach to the sulfidation of supported metal oxide catalysts for hydrodesulfurization applications.

CHAPTER 2

LITERATURE REVIEW

2.1 Mesoporous Silica and Other Molecular Sieve Supports

In general, silica and silica-based materials have drawn attention as catalysts support for heterogeneous catalysis [42–44] but also for HDS in particular [45–47]. These silica-based materials are desirable because of their highly ordered pore size and volume and their large surface area, but it is important to note that these materials have also demonstrated a weak metal-support interaction. Because of this low metal-support interaction in silica, it became essential to be able to modify the support to increase the metal-support interaction. Recently, there has been a lot of effort to improve the metal-support interaction and active phase dispersion of silica-based supported HDS catalysts. The use of heteroatoms such as alumina, titania and zirconia to modify the mesoporous silica properties have been extensively studied [48–52]. The work of Jiang et al. studied the effect of Si/Al ratio on the NiMo/Al-SBA-15 catalytic properties [53]. It was observed that the total acidity of the NiMo/Al-SBA-15 catalysts and the metal-support interaction increase with Si/Al ratio; however, the BrØnsted acidity was highest when Si/Al ratio is 10. Furthermore, the average stacking number of NiMoS slab decreased with Si/Al ratio while the layer length was shortened at Si/Al ratio of 10. A curved fullerene-like morphology due to 1) the excellent dispersion of MoS2 active phase on the Al- or Ti-modified SBA-15 support and 2) the stabilization of the Co-promoted MoS_2. The latter effect is reported to impact on the HDS activity of the Al- or Ti-modified SBA-15 CoMo catalyst [54]. Zirconia modification of

SBA-15 was found to increase the promoter dispersion due to the Co-support interaction, and this enhanced the promotion effect of the Co on MoS_2 active phase. Additionally, the inactive β-$CoMoO_4$ phase, which is often detected in CoMo/SBA-15 catalyst, was not observed after support modification with ZrO_2 [55]. Further studies on how to increase the dispersion of active phase through the Ti-Zr bi-heteroatom modification of SBA-15 support demonstrated that the electronegativity difference between the Ti and Zr further stabilized the inactive and undesirable MoO_4^{2-} phase, which leads to low sulfidation [56]. Indeed, the poor performance of Ti-Zr bi-heteroatom modified SBA-15 supported CoMo catalyst has deterred further studies into the use of bi-heteroatom to modify the SBA-15 properties even though different heteroatom combination could likely result in different electronic and structural re-arrangement. Gutiérrez et al. reported the effect of four different supports: γ-Al_2O_3, SBA-15, Zr-SBA-15 and Ti-SBA-15 for the simultaneous HDS of DBT and hydrodenitrogenation (HDN) of o-propylaniline (OPA). The Zr and Ti modification of the SBA-15 considerably decreased the SBA-15 surface area; however, more active sites were observed (due to increased Lewis acid sites) in the Ni promoted Zr- and Ti-SBA-15-Mo catalysts than in the unmodified SBA-15-Mo catalyst [25]. Dinh et al. optimized the loading of TiO_2 on calcined SBA-15 support for CoMo catalyst [46]. Within the range of 10-40 wt.% nanocrystallites TiO_2 loading, an excellent dispersion of the active phase was observed at 20 wt.%. At lower TiO_2 loading (below 20 wt.%), the inactive $CoMoO_4$ phase was observed, and at higher loading, large aggregates of TiO_2 were noticed. Both are detrimental to the HDS activity of the CoMo catalyst. The effect of Ti-SBA-15 and γ-Al_2O_3 hybrid as a support for NiMo catalysts was also compared with that of the Ti-SBA-15 and γ-Al_2O_3 counterparts in the HDS of DBT and 4,6-DMDBT, and it was reported that the

incorporation of Ti-SBA-15 to alumina inhibits the formation of the inactive MoO4 phase [57]. In addition, the hybrid supported NiMo catalysts performs 40% more than NiMo/γ-Al2O3 in the HDS of 4,6-DMDBT even though nearly the same conversion was recorded for the HDS of DBT. Trimetallic catalysts have also been supported on SBA-15 to form highly active HDS catalysts. The work of Mendoza-Nieto et al. compared the efficiency of NiMoW/SBA-15 catalysts over the bimetallic NiMo/SBA-15 and NiW/SBA-15 catalysts and discovered that the $Mo(W)S_2$ active phases were better dispersed on the support than in the bimetallic systems [58]. More so, the highest number of active phases are located on the edge sites of the catalyst, which afforded the catalysts highest DDS and HDS activity (**Fig. 2.1**).

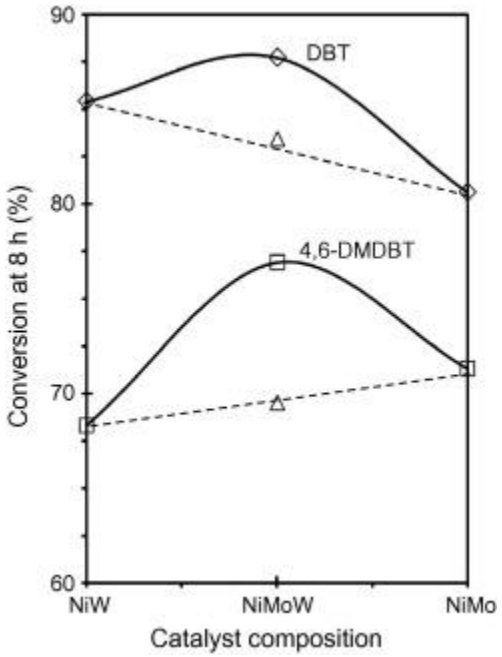

Figure 2. 1: Comparison of the catalytic activity of NiMo, NiMoW and NiW catalysts supported on SBA-15 in HDS of DBT (◊) and 4,6-DMDBT (□). Open triangles correspond to the results obtained with trimetallic NiMo-NiW/SBA-15 catalyst prepared by mechanical mixing of corresponding bimetallic counterparts. Reprinted with permission from [58].

Mechanically mixed SBA-15 and SBA-16 support for CoMoW catalyst has also proved to be better support than the individual SBA-15 or SBA-16. The mixed support contains mixed porosity, which may be the reason for the better diffusion of active phase precursor solution through the support medium (thus inhibit external mass transfer limitation) [59].

KIT-6 and KIT-5 silica are another class of mesoporous molecular sieves that have shown great potential as HDS support catalyst [60–63]. The three-dimensional (3D) mesoporosity of KIT-6/KIT-5 afford it an extra advantage of better catalyst dispersion, higher reducibility of the Mo oxides, and faster diffusion of reactants and products over other 2D molecular sieves (e.g., SBA-15) [31]. Similar to SBA-15, modification of the KIT-6/KIT-5 properties by incorporating heteroatoms such as Al, the metal-support interaction and surface acidity have been enhanced, which in turn has increased the HDS performance of catalysts [60,64]. Zeolites are a class of materials with unique pore architectures that can be made to fit almost any chemical conversion, and these materials have easily accessible active sites [65]. As such, zeolites have also found application as support in HDS reaction [19,66]. However, the small pore size of many zeolites hinders the diffusion of large sulfur molecules. For example, the molecular size of 4,6-DMDBT (0.78 × 1.13 nm by DFT calculations) was larger than the pores of BETA (0.65–0.68 nm) and ZSM-5 (0.55 nm) mesoporous zeolites [67]. Furthermore, most zeolites are characterized with excessive acidity, which causes cracking more than the HDS activity [68]. Therefore, the zeolites are mostly used as HDS support after their pores have been expanded and their acidity has been reduced. Tang et al. have developed parallel mesopore channels in the nanofiber of microporous mordenite and have efficiently dispersed the CoMo in both the micropores and mesopores of the mordenite support [69]. The active phase in the micropores

significantly affect the overall HDS activity of the mordenite supported CoMo catalyst by producing a large amount of spillover hydrogen that later diffuse onto a nearby CoMo active phase in the mesopores, consequently boosting the HYD pathway of the catalyst. An in-depth study into the HDS mechanism of thiophene over a zeolite L-supported CoMo catalyst using computational calculations revealed that the zeolite L acted as an electron donor and that its pore framework decreased the HYD energy barrier, which made the HYD pathway more favorable [70]. The work of Quan Huo et al. demonstrated the modification of zeolite L by slowly adding the zeolite to a solution of CTAB in water and later adjusting the pH to 9.6 [71]. The solution was heated at 100 ^{o}C for 2 days in a Teflon-lined autoclave to yield the micro-meso molecular sieve composite with increased textural properties and moderate acidity, which resulted in better metal dispersion and HDS activity. Y-zeolite porosity and surface acidity was easily modulated by direct incorporation of Ga in the Si-O-Al framework. Thus, some of the strong acid sites (Si–O(H)Al) in the Y-zeolite got substituted by weak acid sites (Si–O(H)Ga). Moreover, the Ga species promoted the sulfidation of both Ni and Mo species and changed the morphology of the active phases [72]. With small amounts of Ga species, more Ni atoms were easily doped into MoS_2 crystals to form more NiMoS active phase. Composite materials made up of mixed supports of highly acidic microporous zeolites and weakly acidic mesoporous molecular sieves have been characterized with combined oxides properties such as presence of micro and meso porosity, moderate acidity, and hydrothermal stability. The combined effect of ZSM-5 and KIT-6 as mixed support lead to the formation of hierarchical porous structures that allows efficient diffusion of reactants and products [62]. Furthermore, the BrØnsted surface acidity of the NiMo/ZSM-5-KIT-6

catalyst was found suitable for the efficient HDS of 4,6-DMDBT, especially via the isomerization pathway (**Fig. 2.2**). Similarly, improved textural properties, acidic strength and edge-cornered MoS_2 sites were achieved when a mixed support of zeolite L and KIT-6 was used to support CoMo active metals [61].

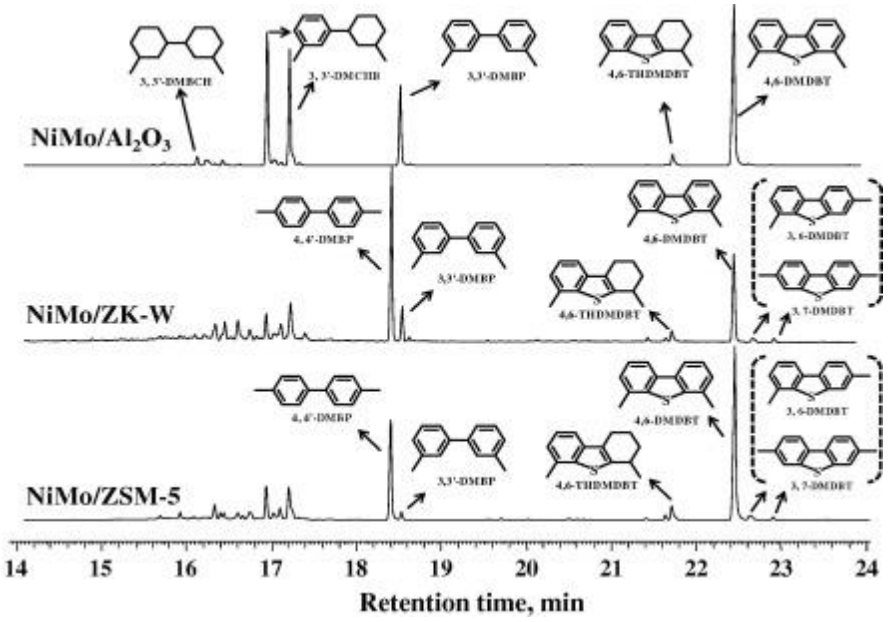

Figure 2. 2: Comparison of GC peaks of the products in the HDS of 4,6-DMDBT over $NiMo/Al_2O_3$, NiMo/ZK-W, and NiMo/ZSM-5 at LHSV = 120 h^{-1}. Reprinted with permission from [62].

Series of composite supports (ZS) consisting of ZSM-15 and SBA-16 in specific ratios have been adopted as support for NiMo metals, and the support's morphological properties as depicted in **Fig. 2.3** were considered as a major determinant of the catalysts HDS activity [73]. The uniform spherical aggregates morphology of ZS-3 consisted of uniform hexagonal-prismatic ZSM-5 monocrystals enabled the transfer of spillover hydrogen that had formed in the micropores of ZSM-5 onto nearby MoS_2 active phases in the mesopores of SBA-16. Moreover, the enhanced reactants and products diffusion and active phase accessibility by reactants have been attributed to the ZS-3 uniform morphology. Further incorporation of cation additives (K^+, Mg^{2+}, Mn^{2+}, Zn^{2+}, and Cu^{2+}) to the ZS series using inorganic salts of the cations changed the textural properties, acidity, metal-support interaction, and morphology of the supports [74]. The NiMo/ZS-Mg catalyst presents exceptionally higher HDS activity than the other series of cation-modified ZS supported NiMo catalysts due to its desired catalytic properties, which include the distribution of pores, acidity, and metal-support interaction. Similarly, a ZSM-5/KIT-6 composite mesoporous sieve had been developed with interesting support properties and more interestingly, the pore structure was successfully tuned by varying the mole ratio of support precursors [75].

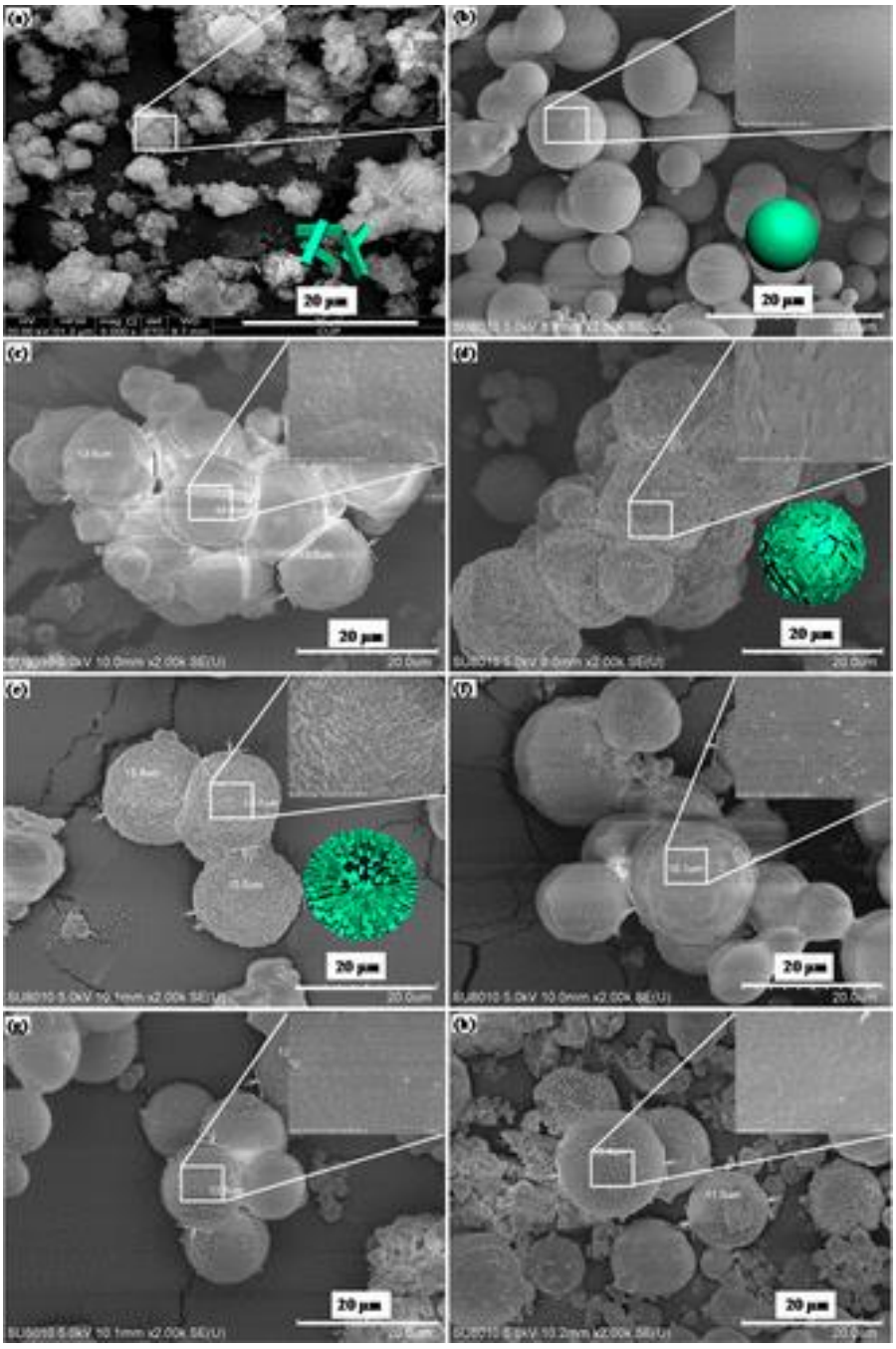

Figure 2. 3: SEM images of the series ZS and pure SBA-16 supports: (a) ZSM-5; (b) SBA-16; (c) ZS-1; (d) ZS-2; (e) ZS-3; (f) ZS-4; (g) ZS-5; (h) ZS-Mechanical. Reprinted with permission from [73].

CHAPTER 3

SYNTHESIS, APPLICATION AND KINETIC MODELING OF CeO_x-Si-CoMo CATALYSTS FOR HYDRODESULFURIZATION OF DIBENZOTHIOPHENE

ABSTRACT

Ultradeep hydrodesulfurization (HDS) of fuel with highly robust catalyst is one of the emphases of the petroleum refiners to achieve clean and safe environment. We report in this study series of CeO_x-Si-CoMo catalysts for efficient HDS activity of DBT in a batch reactor. The dispersion and catalytic activity of the active species (CoMoS) is greatly influenced by the CeO_x-Si network in the support, and the structural-reactivity of the catalysts are extensively studied. The BET surface area, X-ray diffraction (XRD) and Raman spectroscopy results showed that Ce up to 2.5 wt.% incorporated into the silica network of SBA-15 demonstrated the optimum support properties. The ease of metal oxide reducibility and the existence of MoS_2 phase in the sulfided 2.5CeO_x-Si-CoMo catalyst revealed that moderate metal-support interaction between the active metals and the supports is achieved at 2.5 wt.% of ceria, which resulted in higher HDS activity. The HDS and hydrogenation (HYD) rate constants for 2.5CeO_x-Si-CoMo catalyst were the largest compared to the rate constants of other catalysts, indicating higher catalytic activity. The 2.5CeO_x-Si-CoMo catalyst directed the HDS reaction towards the HYD pathway more than the other catalysts.

3.1 Introduction

Energy demand is always on the increase due to increasing population and civilization [76]. The major source of energy until now remain the fossil fuel [77]. This fuel has recently shown increasing amount of sulfur due to continuous oil exploration. In addition, regulatory bodies such as European commission have put a limit (< 10 ppm) to the amount of sulfur emitted from the exhaust of vehicles due to pollution. These stringent sulfur regulations have put refineries in a very challenging situation of searching for new hydrotreating catalysts that can work effectively to bring down the sulfur level to below 10 ppm. Research emphasis has been on developing new large surface area support that can combine both support acidity and moderate metal support interaction properties for high metal dispersion [78].

Silica based mesoporous materials with large surface area and relatively weak acidity such as SBA-15 have recently gain much attention as active metals support for hydrodesulfurization (HDS) applications. The silica support has also been modified by incorporating heteroatom such as Al, Ti and Zr to improve the metal support interaction to a moderate level [41,79,80]. The impact of heteroatoms and the preparation condition on both support properties and active metals dispersion are continuously being investigated. Recent studies on the role of Al on the support properties of KIT-6 mesoporous silica revealed that the metal incorporation increased support interaction with the active phases, and subsequently enhanced the HDS performance of the CoMo catalyst [60]. By inserting tetragonal zirconia to the alumina support framework using zirconium isopropoxide, the Mo – alumina interaction was reported to be decreased, which gives better dispersion of

NiMoS phase [81]. Franklin et al. reported an increase in dispersion of MoO_3 species with the incorporation of alumina, niobia, titania and zirconia into the framework of MCM-41 support. The increased dispersion, due to incorporation of the heteroatoms, was explained based on the increased active metal – support interaction [82]. By adjusting the pH of reaction mixture, Shuo et al. was able to incorporate a large amount of Al and Ti to the mesoporous walls of pure silica SBA-15 with almost all in 4-coordinated environments [83]. The obtained material has high ordered mesostructure with uniform size distribution and large surface area. High dispersion and uniform distribution of octahedral Ni and Mo species on SBA-15 was observed when Ti was attached to the framework of the SBA-15. The NiMo/TiSBA-15 catalyst showed much better catalytic performance in HDS and hydrodenitrogenation than its NiMo/SBA-15 counterpart [84]. We were motivated by the effect of these reported heteroatoms to study the role of ceria on the dispersion and catalytic activity of SBA-15 supported CoMo catalysts. In addition to its redox properties, the acid-base property is yet another exploitable property of ceria [85–87] that has been utilized in developing a lot of catalysts for different applications such as hydrogenation [88] and hydrogenolysis [89].

To the best of our knowledge, there is no reported work on the role of ceria on the performance of HDS catalysts for organosulfur compounds removal. Therefore, we report herein the modification of silica framework of SBA-15 support by incorporation of ceria (using as-prepared ceria isopropoxide precursor), and the resultant effect on the sulfided-CoMo catalyst for HDS of DBT. The role of ceria on the product selectivity and kinetic parameters of the HDS process are well studied and a plausible mechanism is thus proposed.

3.2 Experimental Section

3.2.1 Synthesis of Ceria Modified SBA-15 Supports and Catalysts

Series of mesoporous ceria modified SBA-15 supports of varying cerium loading (1 – 10 wt.%) were synthesized following the synthesis procedure of SBA-15 [51,90]. The 1 – 10 wt.% ceria loading were incorporated to SBA-15 by addition of equivalent amount of as-prepared cerium isopropoxide to acidic solution mixture of TEOS and Pluronic P123 after stirring for 1.5 h. The synthesis procedure for cerium isopropoxide has been previously reported [91].

The ceria modified SBA-15 supported CoMo catalysts were prepared by impregnation of the Co and Mo active phase on the supports via excess wet solution method in deionized water. The method involves stirring 3 wt.% equivalent amounts of $CoCl_2$ and 10 wt.% ammonium molybdate (vi) tetrahydrate at 50 ^oC for 1h, followed by addition of dispersed solution of the supports in deionized water. The mixture was further stirred until nearly all the deionized water is evaporated. The remaining solution was later dried in an oven at 80 ^oC for overnight, and subsequently calcined at 550 ^oC for 5 h at ramping of 10 ^oC/min. The powdered metal oxide catalysts were pelletized to within 300 -500 microns.

Full description of the developed supports and catalysts studied in this work is presented in **Table 3.1**.

Table 3. 1: Supports and Catalysts Description

Code	Description
SBA-15	Mesoporous silica
yCeO_x-Si	SBA-15 modified with y wt.% ceria
Si-CoMo	SBA-15 impregnated with Co and Mo
yCeO_x-Si CoMo	yCeO_x-Si impregnated with Co and Mo

3.2.2 Characterization of Supported Catalysts

The textural properties such as surface area, pore size and pore volume of the prepared catalysts were recorded on a Micromeritics ASAP 2020 using N_2 adsorption-desorption isotherms at 77k. Prior to measurement, the catalysts were vacuum-degassed at 250 ^oC for 3 h to remove impurities. Brunauer, Emmett, and Teller (BET) method was used to calculate the surface area, and absorption branch of Barrett, Joyner, and Halenda (BJH) method was applied to calculate the pore size and pore volume of the catalysts. The crystallinity of the supports and catalysts was determined by recording their X-ray diffraction pattern between 10 ^{o} to 90 ^{o} 2θ using Rigaku Ultima IV X-ray diffractometer. The operation was performed at 40 kv and 40 mA with a scanning speed of 10 ^{o}/min. Raman spectra of the supports and catalysts were obtained using a HORIBA, iHR320 with CCD detector Raman spectroscope. The spectroscope was operated at laser wavelength of 532 nm under room temperature condition. Fourier transformation infrared (FTIR) spectra of supports and catalysts were recorded on a Thermo Scientific Nicolet 6,700 FTIR spectrometer over a wavelength range of 400 – 4000 cm^{-1}. The sample preparation requires

mixing 1% support/catalyst with KBr, and the crushed powder was pelletized using AtlasTM automatic press 8 ton to form a thin disc, which was inserted into the FTIR cell for the analysis. The catalysts oxides H_2-reducibility were determined by temperature-programmed reduction with hydrogen as a probe molecule (H_2-TPR). The analysis was carried out using an AutoChem II – 2920 Micromeritics Chemisorption analyzer. Roughly 50 mg of the calcined catalyst was heated to 500 ^oC for one hour under the flow of high purity helium in order to remove impurities. After cooling to ambient temperature under the same helium flow, the gas flow was switched to 10 % H_2 in helium (at steady flow of 20 ml/min) and the temperature was raised to 1000 ^oC at 10 ^oC/min ramping. Under these conditions, the amount of H_2 consumed at the reducible temperatures was recorded. The surface acidity of the catalysts was determined using an in-situ pyridine FTIR (with self-supported wafer). The sample, placed in a Specac cell, was pretreated under vacuum of 1.33×10^{-3} Pa at 500 ^oC for 1 h, and later the temperature was decreased to 150 ^oC before flowing pyridine vapor for 30 min. Excess pyridine vapor was expelled from the treated sample by degassing at 150 ^oC, and the total acidity due to Lewis and Bronsted acid sites were recorded. The morphology of sulfided catalysts were recorded on a Field Emission Scanning Electron Microscope FESEM (TESCAN, LYRA 3) using a secondary electron (SE) and the back scattered electron (BSE) mode at an accelerating voltage of 20 kV. Transmission electron microscope (TEM) images of MoS_2 crystallites were recorded on a JEOL-JEM-2100 operated at 200 kV. Bonding states and binding energy of the sulfided catalysts were determined by X-ray photoelectron spectroscopy (XPS) using PHI 5000 Versa Probe II, ULVAC-PHI Inc. spectroscope. Disc pelletized sample of the catalysts was first subjected to high vacuum before the XPS analysis. Elemental composition of the

sulfided catalysts were measured by X-ray fluorescence spectroscopy (XRF) using a Bruker M4 TORNADO Micro-XRF equipped with 30 mm2 Xflash® SD detector.

3.2.3 Catalysts Presulfidation and Performance Evaluation

The pelletized metal oxide catalysts were reduced at 400 ^{o}C for 3 h under a flow of 10% H_2/He in a quartz tubular furnace. After the 3 h, the furnace temperature was brought down to 350 ^{o}C and 2 wt.% CS_2 in cyclohexane was flowed through the tubular furnace at the rate of 0.5 mL/min for 5 h to presulfide the reduced metals.

The HDS performance evaluation of the presulfided catalysts was carried out in a high-pressure Parr 4590 Micro Bench Top Reactor operated at a pressure of 5MPa and 100 rpm stirring rate. Approximately 25 mg of the presulfided catalyst was added to 15 ml of model fuel containing 1000 ppm DBT in dodecane. The reaction was performed for 4 h after the reaction conditions have been stabilized, and product sampling were done at an hour interval.

3.3 Results and Discussion

3.3.1 Characterization Results

An in-depth understanding of the textural properties of a catalyst material often gives a comprehensive guide on how the material is likely to perform in the chosen application [92]. Generally, the surface area and porosity of the developed material are of paramount importance in elucidating the textural properties of the material. The textural properties of the SBA-15 and CeO_x-Si supports, and the supported CoMo catalysts are presented in Table 3.2. It was observed that the BET surface area of the supports decreases continuously with increase in Ce wt.% loading except for 2.5CeO_x-Si, where the BET surface area

increases by up to 8 m^2/g. This phenomenon was explained by Timofeeva et al. [93], where they proposed that the ease of incorporation of Ce into the SBA-15 framework is achieved with the use of low amount of Ce ions in the sol-solution of the SBA-15. At high Ce ion concentration in SBA-15 sol-solution, extra framework cerium oxide formation is most probable, and this will significantly affect the surface area and pore volume of the as-synthesized CeO_x-Si, in addition to its catalytic properties as observed in 5CeO_x-Si and 10CeO_x-Si supports. This is evident from the N_2 adsorption-desorption isotherms and the pore volume-size distribution of the supports presented in **Fig. 3.1a and b** respectively. The slight decrease in the BET surface area of 1CeO_x-Si may imply that at 1Ce wt.% loading, Ce ions are not enough to fill into the framework of the SBA-15 via ion-exchange of the Ce^{3+}/Ce^{4+} with Si^{4+} of the SBA-15 during hydrolysis and condensation process. The addition of Co and Mo to the supports by impregnation approach and further sulfidation of the reduced active metals however, showed decreased surface area and pore volume in all the catalysts due to the obstruction of some surface and void spaces. The 2.5CeO_x-Si-CoMo catalyst showed higher surface area (136.8 m^2/g) and total pore volume (0.34 cm^3/g) than all the other CeO_x-Si-CoMo catalysts (**Fig. 3.2 a and b**), thus putting the catalyst in a better position for catalytic performance.

Table 3. 2: Textural properties of supports and catalysts

Supports and catalysts	**BET Surface area (m^2/g)**	**Microporous surface area (m^2/g)**	**External surface area (m^2/g)**	**Microporous pore volume (cm^3/g)**	**Total pore volume (cm^3/g)**	**Average pore size (nm)**
SBA-15	639.1	48.3	590.7	0.023	1.07	6.71
1CeO$_x$-Si	607.6	38.1	569.4	0.018	1.01	6.73
2.5CeO$_x$-Si	647.1	49.7	597.4	0.024	1.06	6.65
5CeO$_x$-Si	575.4	47.5	527.9	0.023	0.95	6.68
10CeO$_x$-Si	532.2	27.0	505.2	0.013	0.89	6.77
Si-CoMo	157.7	10.4	147.3	0.0051	0.30	7.61
1CeO$_x$-Si-CoMo	117.7	8.9	108.8	0.0045	0.32	10.93
2.5CeO$_x$-Si-CoMo	136.8	12.1	124.0	0.0066	0.34	9.85
5CeO$_x$-Si-CoMo	124.9	17.2	107.7	0.0089	0.29	9.34
10CeO$_x$-Si-CoMo	131.8	17.4	114.4	0.0090	0.32	9.61

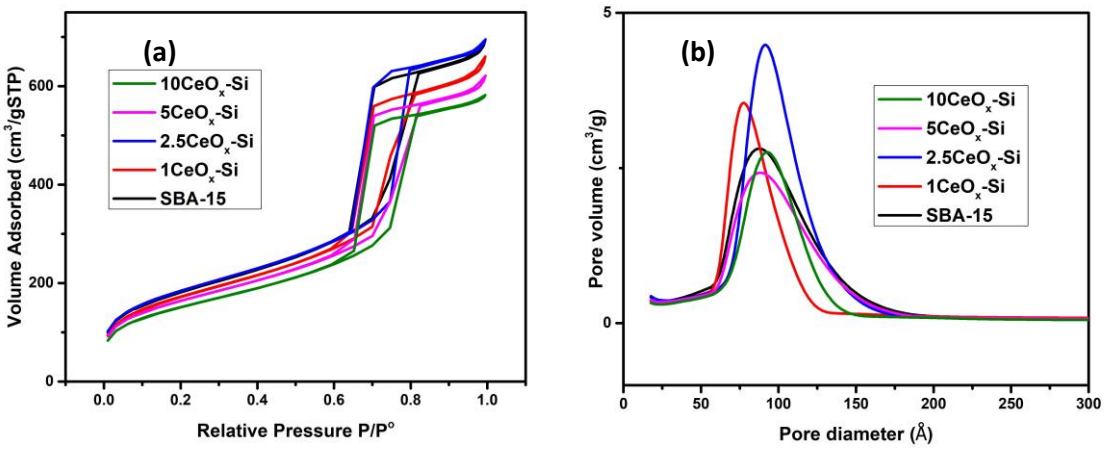

Figure 3. 1: (a) N_2 adsorption desorption isotherm and (b) pore volume-size distribution of SBA-15 and yCeOx-Si supports

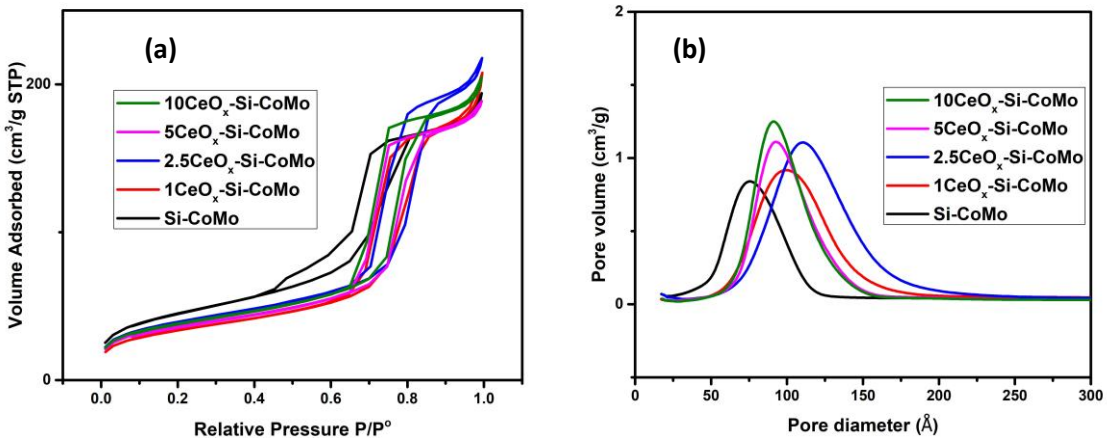

Figure 3. 2: (a) N_2 adsorption desorption isotherm and (b) pore volume-size distribution of supported CoMo catalysts

The X-ray diffraction patterns of the supports and catalysts were performed to determine the crystallinity and dispersion of the sulfided active metals catalysts on the SBA-15 support. The XRD pattern of all the supports in **Fig. 3.3(a-e)** show a broad diffraction peak between 20 ^{o} to 30 ^{o} which is a typical characteristic peak of amorphous silica [94]. The absence of ceria diffraction peaks is considered an indication that ceria has been incorporated into the SBA-15 [95]. The XRD spectra of sulfided catalysts presented in **Fig. 3.3(f-j)** show the MoO_3 phase pattern with a quality mark (QM) of Star (well characterized chemically and crystallographically with no unindexed lines at $\Delta 2\theta \leq 0.03^{o}$) for Si-CoMo, $5CeO_x$-Si-CoMo and $10CeO_x$-Si-CoMo. However, $1CeO_x$-Si-CoMo and $2.5CeO_x$-Si-CoMo show an MoS_2 phase pattern with a QM of I (well characterized chemically with no unindexed strong line at $\Delta 2\theta \leq 0.06^{o}$) [96]. It was further observed that the (111) crystal plane of MoO_2 due to the incomplete sulfidation is present at 26 2θ (^{o}) in the $1CeO_x$-Si-CoMo and $2.5CeO_x$-Si-CoMo catalysts. The peaks intensity of the MoO_3 phase follow the trend: Si-CoMo < $5CeO_x$-Si-CoMo < $10CeO_x$-Si-CoMo, while the peak intensity of MoS_2 phase follow the trend: $1CeO_x$-Si-CoMo < $2.5CeO_x$-Si-CoMo. This indicates that the ease of sulfidation follows the trend $2.5CeO_x$-Si-CoMo > $1CeO_x$-Si-CoMo > $5CeO_x$-Si-CoMo > $10CeO_x$-Si-CoMo. The observed sulfidation trend can be ascribed to the role of ceria on the metal-support interaction. At 2.5 Ce wt.% loading, the optimum metal-support interaction could be said to have been achieved, however, at ceria loading of 5 and 10 wt.%, the metal-support interaction may be large enough to deter the reduction of the Mo species.

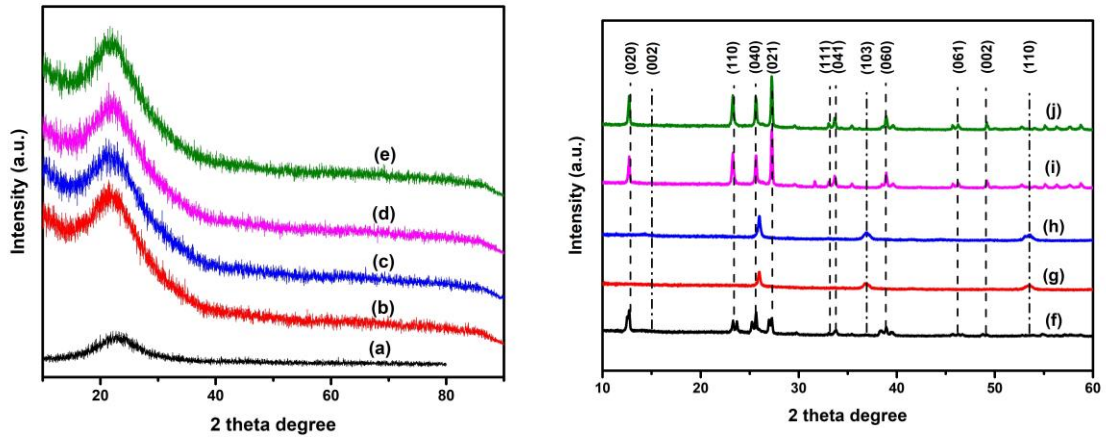

Figure 3. 3: Wide angle XRD pattern of the supports: (a) SBA-15; (b) $1CeO_x$-Si; (c) $2.5CeO_x$-Si; (d) $5CeO_x$-Si; (e) $10CeO_x$-Si and the catalysts: (f) Si-CoMo; (g) $1CeO_x$-Si-CoMo; (h) $2.5CeO_x$-Si-CoMo; (i) $5CeO_x$-Si-CoMo; (j) $10CeO_x$-Si-CoMo. The dash lines and dash-dot line.

Raman spectroscopy has been utilized as a sensitive tool to unravel the molecular structure of metal oxides [97]. The Raman spectra of the supports show very weak peaks at 605 and 850 cm-1 which were assigned to the vibrational stretching mode of the surface hydroxyl group in Si-OH and the symmetrical stretching of the Si-O-Si linkage respectively. Close observation of the Raman spectra of the 5 wt.% and 10 wt.% CeO_x-Si supports revealed a Raman band at 420 cm^{-1}. This band is characteristics Raman band of cerium oxide [98], which means that at high ceria loading some of the cerium ions are not attached to the Si-O-Si framework of SBA-15. This support the findings in the textural properties of the supports that extra framework cerium oxide formation is most probable at high cerium concentration. The Raman spectra of the sulfided catalysts (**Fig. 3.4a-e**) showed peaks at 284, 665, 815 and 993 cm^{-1} for Si-CoMo, 5CeO_x-Si-CoMo and 10CeO_x-Si-CoMo, which are characteristics bands for MoO_3 [99]. The peaks at 284 and 665 cm^{-1} are assigned to the wagging modes of the terminal oxygen atoms and asymmetric stretching of the Mo-O-Mo, while the bands at 815 and 993 cm^{-1} are ascribed to the symmetric stretching and asymmetric stretching of the terminal oxygen in MoO_3. The presence of MoO_3 phase in the sulfided Si-CoMo, 5CeO_x-Si-CoMo and 10CeO_x-Si-CoMo catalysts shows that some of the molybdenum species have not been completely reduced and further sulfided in the catalysts. However, these Raman bands were not observed in the 1CeO_x-Si-CoMo and 2.5CeO_x-Si-CoMo, instead Raman frequencies of vibrational modes of S-Mo-S (385 and 407 cm^{-1}) were detected [99,100]. Therefore, it can be inferred that Ce loading up to 2.5 wt.% increased the metal-support interaction to an optimum level that enhanced the molybdenum dispersion on the support, and thus ease its reduction and sulfidation.

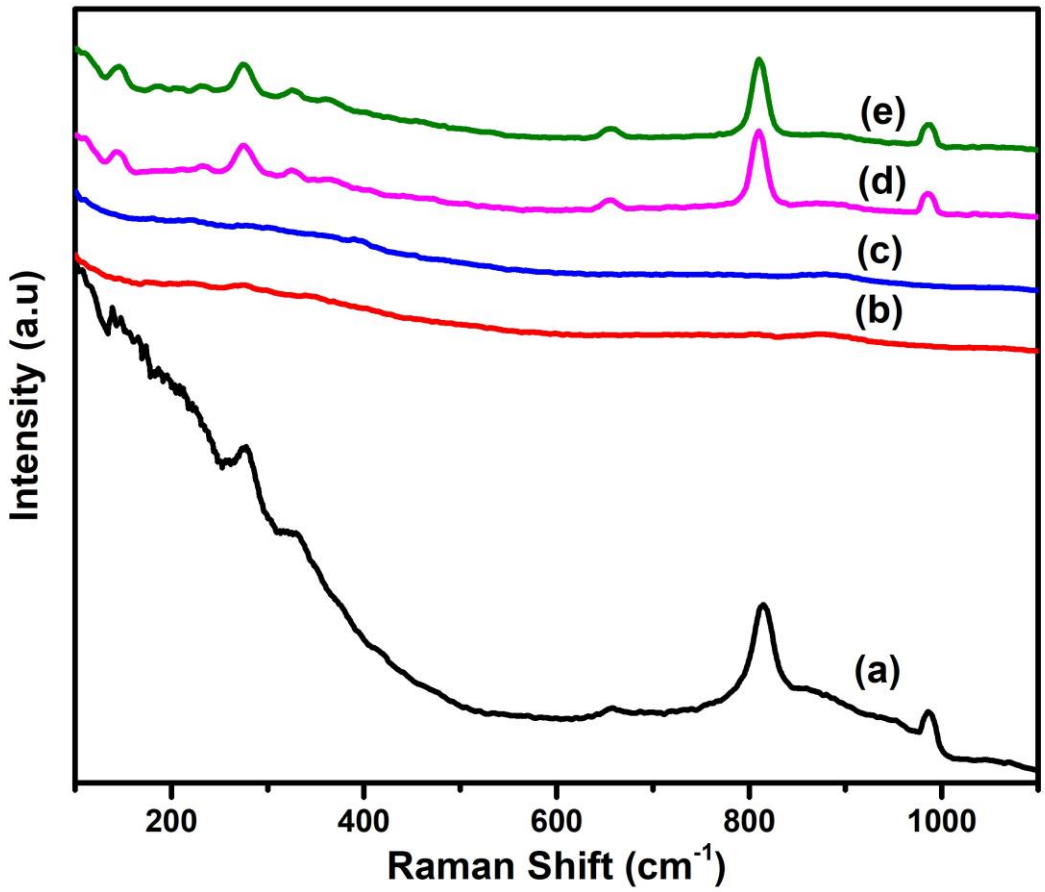

Figure 3. 4: Raman spectra of the catalysts: (a) Si-CoMo; (b) 1CeO_x-Si-CoMo; (c) 2.5CeO_x-Si-CoMo; (d) 5CeO_x-Si-CoMo; (e) 10CeO_x-Si-CoMo.

The FTIR spectra of the supports (a-e) and sulfided catalysts (f-j) are presented in **Fig. 3.5**. The appearance of broad peak at 3300 – 3500 cm^{-1} in all the samples is due to the stretching vibration of Si-OH present in the SBA-15 channels and the O-H stretching of water absorbed on the surfaces of the supports and catalysts. At 1600 cm^{-1}, a sharp peak was observed which is assigned to the O-H bending vibration of the absorbed water molecules. It was noticed that the peak intensities of both peaks decrease proportionately with Ce loading in the support, which implies that some of the SBA-15 pores have been occupied due to ceria loading. The broad band at 1240 cm^{-1} is assigned to the Si-O-Si stretching vibration, and it was observed that the wavenumber increases slightly with ceria loading, and at 10CeO_x-Si, the wavenumber is approximately 1300 cm^{-1} [101,102]. In addition, the intensity of the peak also decreases with ceria loading, again confirming that Si-O-Si bond is being substituted with Si-O-Ce bond as the ceria loading increases [95]. After loading of Co and Mo, the broad peak at 3300 – 3500 cm^{-1} and the sharp peak at 1600 cm^{-1} for the O-H stretching and bending vibration of absorbed water molecules respectively were noticeably decreased, indicating that the free void in the mesoporous supports have been filled with the loaded Co and Mo metals.

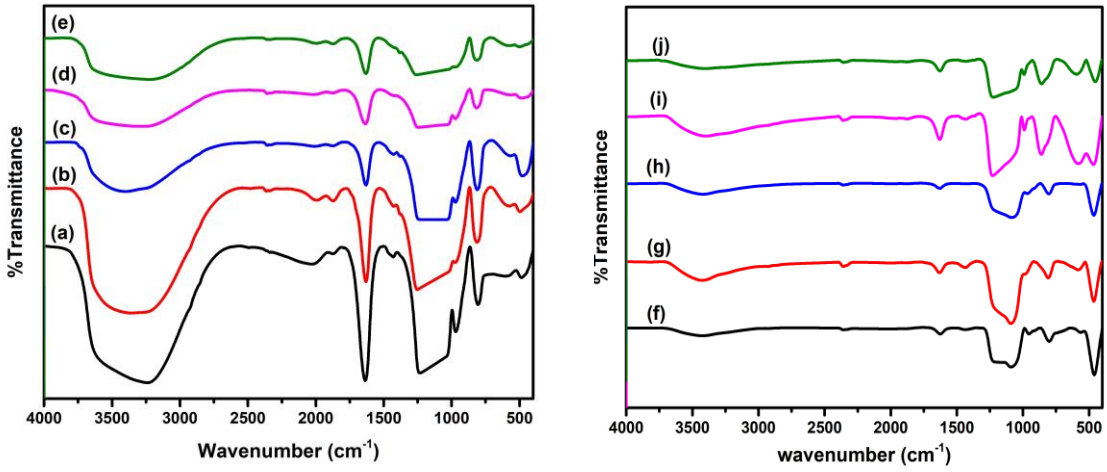

Figure 3. 5: FTIR spectra of the supports: (a) SBA-15; (b) $1CeO_x$-Si; (c) $2.5CeO_x$-Si; (d) $5CeO_x$-Si; (e) $10CeO_x$-Si and the catalysts: (f) Si-CoMo; (g) $1CeO_x$-Si-CoMo; (h) $2.5CeO_x$-Si-CoMo; (i) $5CeO_x$-Si-CoMo; (j) $10CeO_x$-Si-CoMo.

The TPR profiles of the catalysts are shown in **Fig. 3.6a-e**. All the metal oxide catalysts show two major peaks at approximately 575 ^{o}C and 900 ^{o}C, which are assigned to the reduction of molybdenum oxide: MoO_3 to MoO_2 and MoO_2 to Mo^0 respectively [103,104] It was also observed that the reducing temperature of the catalysts slightly decrease as the ceria loading increases up to 2.5 wt.% loading. This suggests that ceria incorporation in to the framework of SBA-15 support increases the mobility and activity of surface oxygen species due to the redox behavior of Ce ($Ce^{4+} \leftrightarrow Ce^{3+}$) and the formation of oxygen vacancy [105,106]. By implication, there will be more Mo species having close contact with the CeO_x-Si than in SBA-15 support, thus resulting in less sintering and more dispersion of Mo in CeO_x-Si supported catalysts. However, above 2.5 wt.% Ce loading, a sharp increase in the reduction temperature was noticed. This implies that with ceria loading up to 5 and 10 wt.%, the metal-support interaction increases abruptly, thus inhibiting the reduction of the MoO_3. This further support the results obtained from the wide angle XRD. Further observation of the Si-CoMo TPR profile reveals a shoulder peak at 324.6 ^{o}C. Similar peak was observed in a study performed by Zepada [107]. The author explained that this shoulder peak is due to the reduction of cobalt oxide to cobalt metal [104], which implies that some cobalt species in the Si-CoMo have set apart from interacting with Mo species. Interestingly, this shoulder peak was not observed in the CeO_x-Si-CoMo catalysts, thus corroborating that ceria incorporation aids the interaction of Co and Mo species.

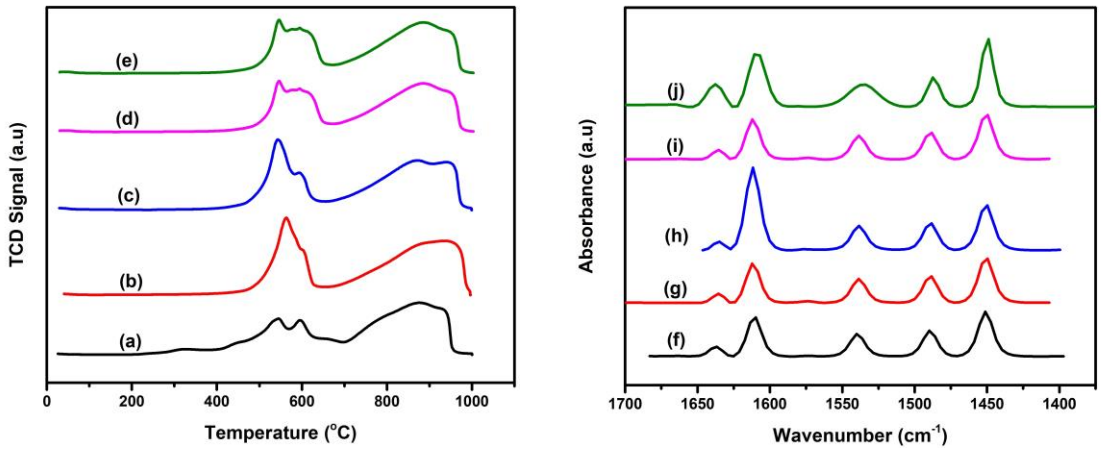

Figure 3. 6: H_2-TPR of the catalysts in their metal oxide form: (a) Si-CoMo; (b) $1CeO_x$-Si-CoMo; (c) $2.5CeO_x$-Si-CoMo; (d) $5CeO_x$-Si-CoMo; (e) $10CeO_x$-Si-CoMo, and FTIR spectra of pyridine adsorbed at 150 ^oC for (f) Si-CoMo; (g) $1CeO_x$-Si-CoMo; (h) $2.5CeO_x$-Si-CoMo; (i) $10CeO_x$-Si-CoMo.

FTIR analysis of adsorbed pyridine (Py-FTIR) at 150 ^{o}C for the catalysts oxides was performed to determine the role of ceria loading on the available acid sites and the acid density of the catalysts. The Py-FTIR spectra and distribution of the acid sites in the catalysts are presented in **Fig. 3.6f-j** and **Table 3.3** respectively. The IR adsorption peaks at 1450 cm^{-1}, 1485 cm^{-1} and 1540 cm^{-1} are assigned to the pyridine molecules adsorbed at the Lewis acid sites, Lewis + Brønsted acid sites and Brønsted acid sites respectively [108]. From the FTIR analysis, it was observed that the acid sites (both Lewis and Brønsted) and acid density of the catalysts increases from Si-CoMo to 10CeO_x-Si-CoMo. This means that the modification of SBA-15 support using ceria heteroatom has significantly increased the catalyst acidity and that the level of acidity increases with ceria loading on the catalyst.

Table 3. 3: The distribution of the acidic sites in the catalysts obtained from Pyr-FTIR.

Catalysts oxides	**Lewis sites(µmol/g)**	***Brønsted sites(*µmol/g)**	**B/L**	**Acid density**
Si-CoMo	**132.78**	**75.01**	**0.56**	**0.62**
1CeO$_x$-Si-CoMo	**137.17**	**81.10**	**0.59**	**0.65**
2.5CeO$_x$-Si-CoMo	**139.62**	**83.68**	**0.60**	**0.67**
5CeO$_x$-Si-CoMo	**151.42**	**89.60**	**0.59**	**0.72**
10CeO$_x$-Si-CoMo	**173.39**	**142.34**	**0.82**	**0.94**

Morphological examination of the Si-CoMo (**Fig. 3.7**) and CeO_x-Si-CoMo catalysts (**Fig. 3.8**) shows that there exist a hexagonally cylindrical short nano-rods that curves somewhat slightly, which is consistent with the structure of mesoporous SBA-15 [109,110]. It was observed that the length of the nano-rods increases with Ce wt.% loading on the support, thus depicting a property of modified mesoporous SBA-15 [51]. Thorough observation of particle density on the surface of the catalysts due to the Co and Mo loading shows that there is a gradual increase in the particle density from Si-CoMo to $2.5CeO_x$-Si-CoMo. However, the particle density decreases at higher Ce loading ($5CeO_x$-Si-CoMo and $10CeO_x$-Si-CoMo). This can be correlated to the increased metal-support interaction and decreased metal dispersion that resulted due to the ceria loading on the SBA-15. With Ce up to 2.5 wt.%, the Co and Mo interaction with the support is at its optimum, hence resulting to optimum metal dispersion on the support. Higher Ce loading results in strong metal-support interaction which causes aggregation of the metal crystallites and low particle density. This further support the XRD and H_2-TPR results. The EDS elemental mapping of the $2.5CeO_x$-Si-CoMo provided in **Fig. 3.9** shows the distribution of the constituent elements in the catalyst.

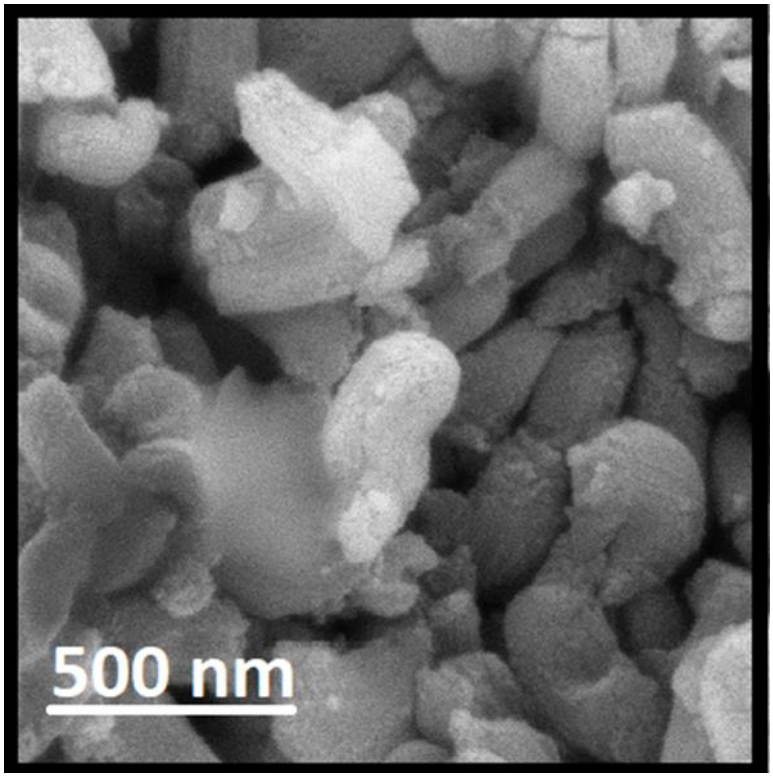

Figure 3. 7: FESEM image for Si-CoMo sulfided catalyst.

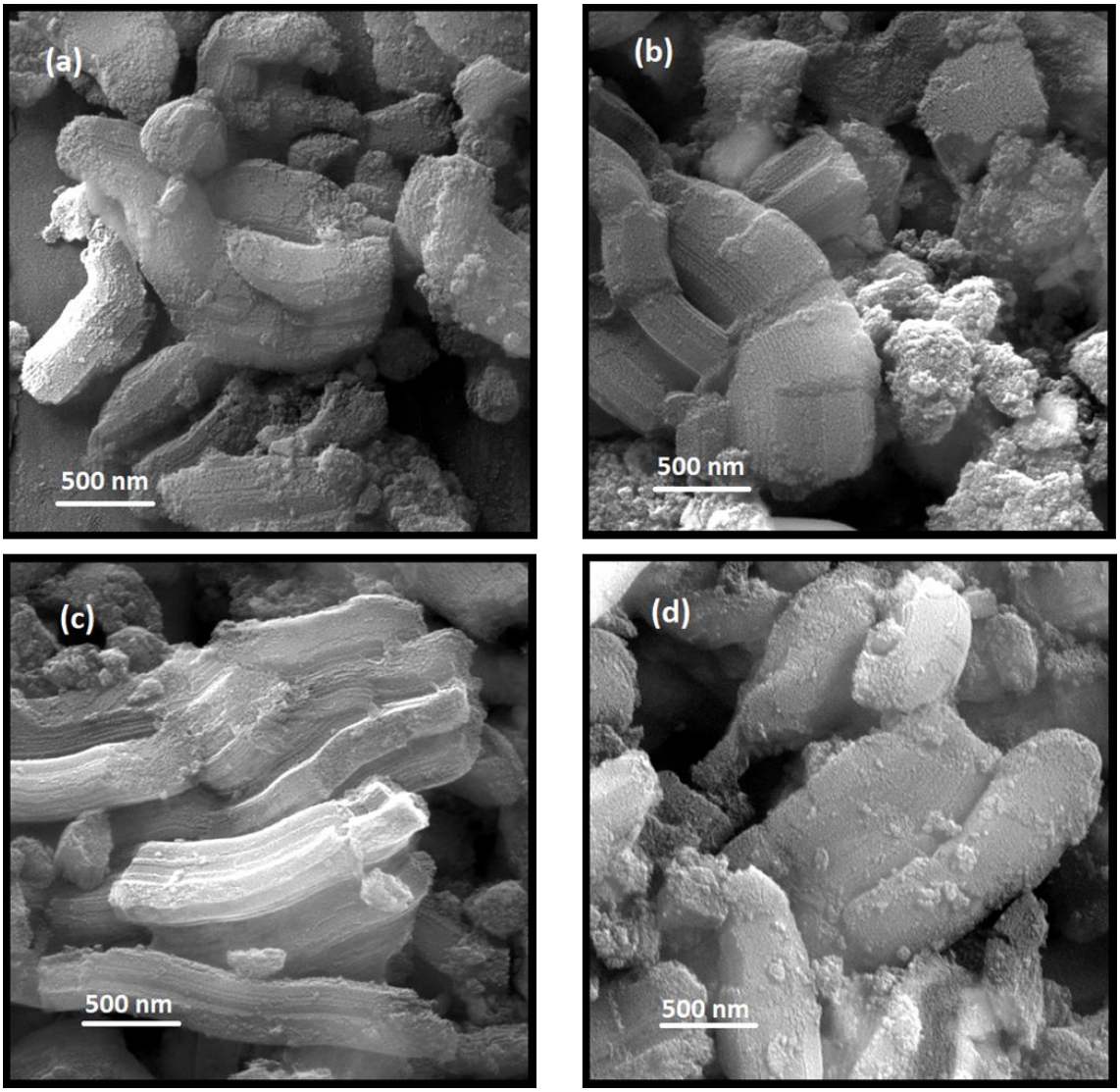

Figure 3. 8: FESEM images of the sulfided catalysts: (a) 1CeO_x-Si-CoMo; (b) 2.5CeO_x-Si-CoMo; (c) 5CeO_x-Si-CoMo; (d) 10CeO_x-Si-CoMo.

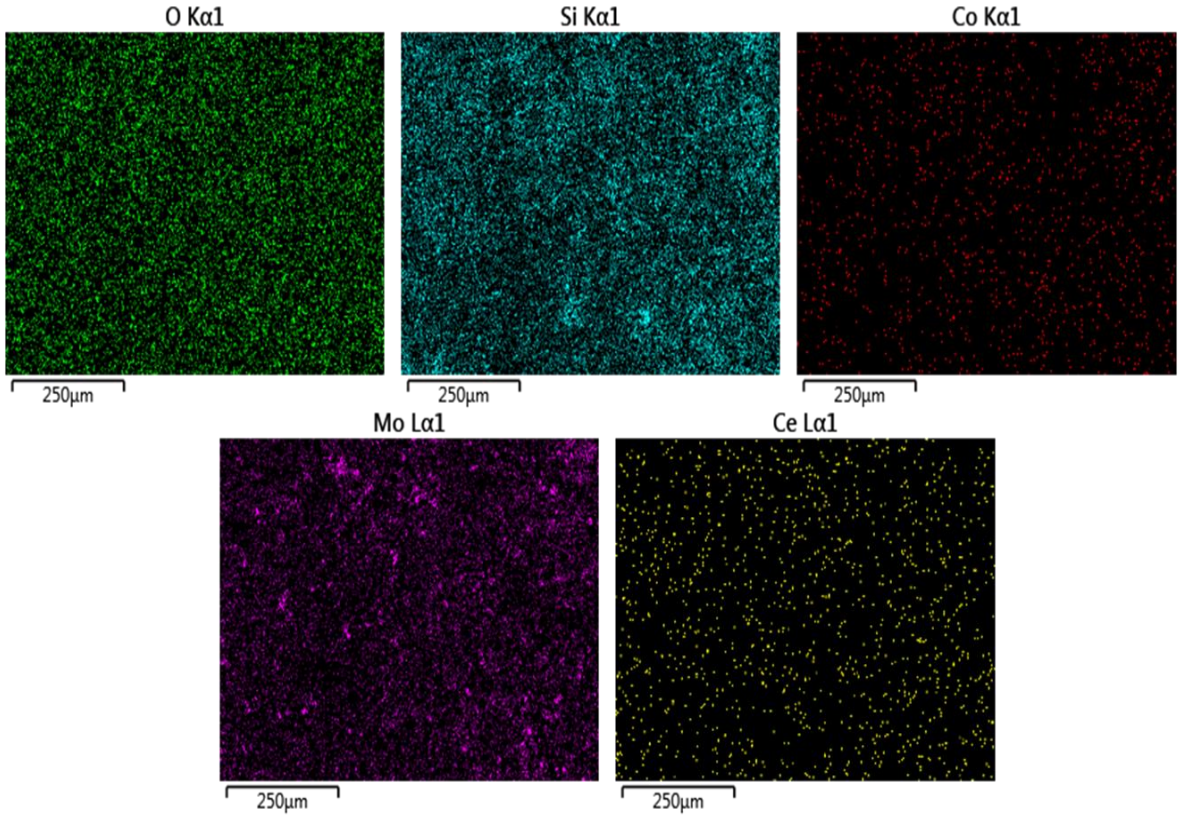

Figure 3. 9: EDS elemental mapping of 2.5CeO_x-Si-CoMo catalyst.

The role of catalyst support modification using ceria on the morphology of MoS_2 active phase and catalyst activity and selectivity can be further understood by using the TEM analysis [108]. The TEM images and MoS_2 crystallites length and stacking degree of the sulfided catalysts are provided in **Fig. 3.10** and **Table 3.4** respectively. The TEM images show different degree of MoS_2 dispersion in the catalysts, and the stacking length and stacking layer variation. The MoS_2 phase in Si-CoMo has an average stacking length of 4 nm and average stacking layer of 3.3. The average stacking length and average stacking layer increases with increase in ceria loading except in 2.5CeO_x-Si-CoMo which has an average stacking length of 3.1 nm and average stacking layer of 3.0. Typically, shorter stacking length of MoS_2 fringes result in more active sites for HDS application [111], while decrease in stacking layers forms the rim sites that favor both the DDS and HYD pathway according to the Rim-Edge model [112]. This mean that the 2.5CeO_x-Si-CoMo has more active sites for HDS reaction and is likely to perform more efficiently in the HDS reaction which will probably occur via both the DDS and HYD pathway.

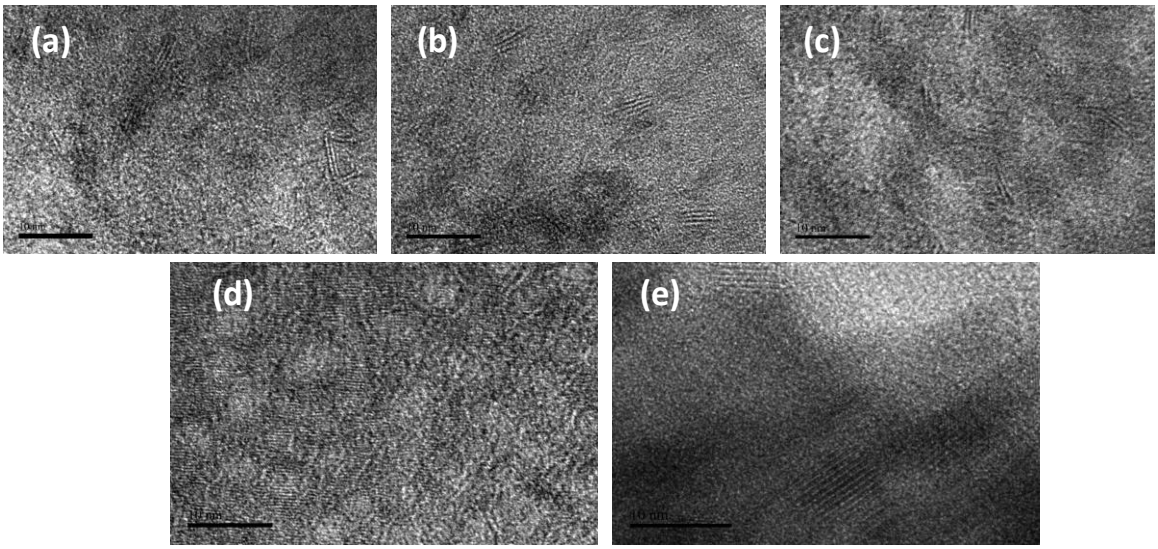

Figure 3. 10: TEM images of sulfided (a) Si-CoMo, (b) 1CeO_x-Si-CoMo, (c) 2.5CeO_x-Si-CoMo, (d) 5CeO_x-Si-CoMo and (e) 10CeO_x-Si-CoMo catalysts.

Table 3. 4: Crystallites length and stacking degree of MoS_2 in the sulfided catalysts.

Catalysts	**Length distribution (nm)**	**Average length (nm)**	**Stacking distribution**	**Average stacking**
Si-CoMo	3.3 – 5.0	4.0	3 – 4	3.3
1CeO$_x$-Si-CoMo	3.3 – 5.8	4.5	3 – 5	4.3
2.5CeO$_x$-Si-CoMo	2.5 – 4.2	3.1	2 – 4	3.0
5CeO$_x$-Si-CoMo	5.0 – 5.8	5.4	4 – 7	5.8
10CeO$_x$-Si-CoMo	5.8 – 6.7	6.0	8 – 10	8.8

The spectra showing various binding states and binding energy of the Mo phases in the sulfided catalysts is presented in **Fig. 3.11**. Though XPS is a surface analysis technique, it is often utilized to gain some insight in to the degree of sulfidation of the Mo species [113]. As shown in **Table 3.5**, three Mo species, distinguished by their unique binding energies, were mapped out from the deconvoluted XPS spectra. Proper identification of the XPS spectra revealed the presence MoS_2 (Mo^{4+} ($3d_{5/2}$)) and MoO_3 (Mo^{6+}($3d_{5/2}$) and Mo^{6+}($3d_{3/2}$)) species in the developed catalysts. However, the atomic percent of the Mo species were found to vary among the Si-CoMo and CeO_x-Si-CoMo catalysts. Noticeably, the XPS peak characteristic of MoS_2 increases from Si-CoMo to 2.5CeO_x-Si-CoMo then became undetectable in higher ceria loaded catalysts. This further explains the ease of Mo sulfidation when ceria (up to 2.5 wt.%) is incorporated into the SBA-15 framework. Interestingly, the only observed XPS peak in 5CeO_x-Si-CoMo and 10CeO_x-Si-CoMo is the MoO_3 peak. The strong metal-support interaction between the support and metal oxides at this high ceria loading has hindered the ease of the metal oxide reduction and sulfidation, which is in perfect agreement with the XRD result obtained for the catalysts.

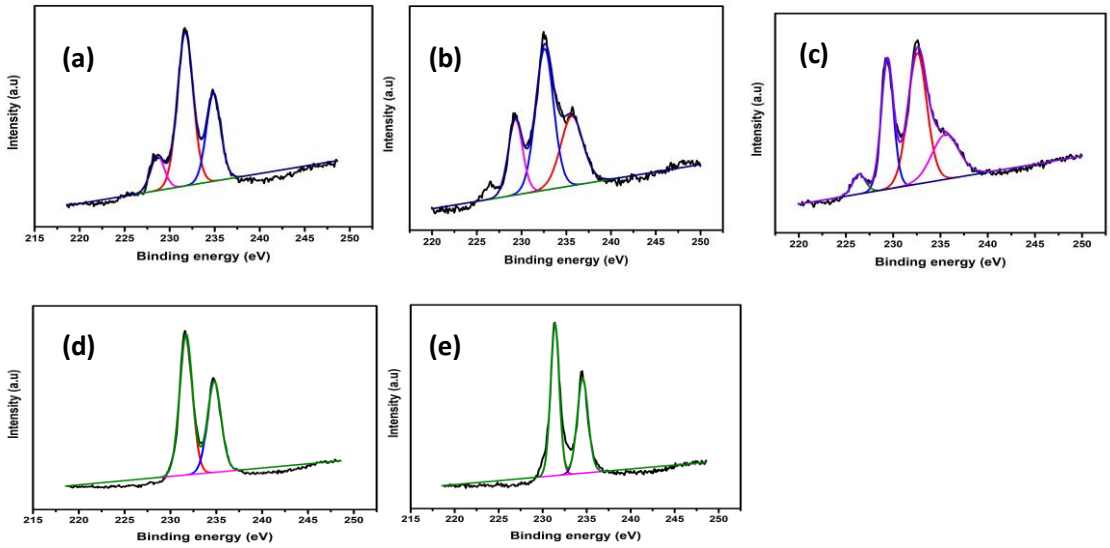

Figure 3. 11: XPS spectra of the sulfide catalysts showing the various Mo phases: (a) Si-CoMo; (b) 1CeO_x-Si-CoMo; (c) 2.5CeO_x-Si-CoMo; (d) 5CeO_x-Si-CoMo; (e) 10CeO_x-Si-CoMo.

Table 3. 5: Different types of Mo phases in the catalysts

Catalysts	**Percent molybdenum in various oxidation states**		
	Mo^{4+} ($3d_{5/2}$)	**Mo^{6+} ($3d_{5/2}$)**	**Mo^{6+} ($3d_{3/2}$)**
Binding energy	**229.5 eV**	**231.8 eV**	**235.6 eV**
Si-CoMo	11.51	58.24	30.25
1CeO_x-Si-CoMo	20.86	30.16	48.98
2.5CeO_x-Si-CoMo	33.44	44.59	21.97
5CeO_x-Si-CoMo	-	40.92	59.08
10CeO_x-Si-CoMo	-	44.16	55.84

The constituent elements that are present in the synthesized catalysts were evaluated using the XRF non-destructive technique (**Table 3.6**). The presence of silicon and oxygen elements in large percent confirms the formation of the silica SBA-15 support in all the catalysts. SBA-15 modification with Ce element was further verified following the Ce element presence and its increasing weight percent in the synthesized catalysts. The disparity in the recorded and theoretical weight percent might have resulted from the addition of the Co and Mo metals after support modification. On the average, it can be ascertained that Co has been well incorporated in all the supports, and in nearly the same amount. However, Mo weight percent across all the catalysts is found to vary significantly. The 2.5CeO_x-Si-CoMo has the highest Mo loading of 8.90%, which is 1.01% more than the Mo loading in Si-CoMo, and this may likely be due to the larger surface area of the former catalyst. The 1CeO_x-Si-CoMo has Mo loading of 6.82%, even lower than 5CeO_x-Si-CoMo and 10CeO_x-Si-CoMo. The probable reason for this ambiguous observation is even though 1CeO_x-Si-CoMo has larger surface area than 5CeO_x-Si-CoMo and 10CeO_x-Si-CoMo, the metal-support interaction in the later catalysts was presumed to be more pronounced as evidenced by XRD, H_2-TPR and Raman characterizations. Thus, attracts more Mo metals than in 1CeO_x-Si-CoMo catalyst.

Table 3. 6: Elemental composition by XRF.

Catalysts	**Elements (%)**				
	Si	**O**	**Ce**	**Co**	**Mo**
Si-CoMo	17.45	74.38	-	0.28	7.89
1CeO$_x$-Si-CoMo	17.47	75.25	0.19	0.27	6.82
2.5CeO$_x$-Si-CoMo	17.51	72.82	0.45	0.32	8.90
5CeO$_x$-Si-CoMo	15.26	76.22	0.79	0.32	7.41
10CeO$_x$-Si-CoMo	16.16	73.96	1.63	0.34	7.91

3.3.2 Catalysts Performance Evaluations

The catalysts performance result presented in the form of percent DBT removal is shown in **Table 3.7**. Under the studied reaction conditions, the HDS of DBT is found to follow an anticipated reaction performance pattern based on the unveiled catalysts characterizations. Within the first one hour of reaction after achieving the stabilized reaction conditions, Si-CoMo had removed up to 32.43% sulfur from 1000 ppm DBT solution (**Fig. 3.12a**). This percent removal was almost doubled (64.89%) when 1CeO_x-Si-CoMo was used as the HDS catalyst. The performance further increased by 8.65% when 2.5CeO_x-Si-CoMo was applied as the HDS catalyst. However, reduction in catalytic activity was noticed when 5CeO_x-Si-CoMo and 10CeO_x-Si-CoMo catalysts were used in the HDS reaction. The observed conversion trend continued for 4 h in all the catalysts, and by the end of the 4^{th} hour, 98.14% sulfur had already been removed from the 1000 ppm DBT in HDS using 2.5CeO_x-Si-CoMo catalyst. The percent sulfur removal in all the catalysts follow the trend: 5CeO_x-Si-CoMo < 10CeO_x-Si-CoMo < Si-CoMo < 1CeO_x-Si-CoMo < 2.5CeO_x-Si-CoMo. Further study was carried out on the effect of the HDS reaction temperature for the most performing catalyst. The result presented in **Table 3.8** and **Fig. 3.12b** show that 64.58% of sulfur was removed at the first 1 h of reaction under process temperature 325 ^oC. This is twice the activity of Si-CoMo under process temperature of 350 ^oC. The advantage of this is the reaction can be studied under lower process temperature by incorporating 2.5Ce wt.% to SBA-15, thus saving a great deal of energy to the refineries. Effect of higher process temperature (of 375 ^oC) was also studied, and it was observed that nearly total sulfur removal (99.27%) is achieved within the first one hour of reaction. The implication of this

result is with 2.5CeO_x-Si-CoMo catalyst in the HDS of DBT, a lot of time and therefore energy in long run can be saved than when Si-CoMo is applied as the HDS catalyst.

Table 3. 7: Catalyst performance results: Percent DBT removal. (Process conditions: 350 ^{o}C; 5 MPa; DBT=1000 ppm; reaction time = 4 h).

Catalysts	**Percent DBT removal (%)**			
	1h	**2h**	**3h**	**4h**
Si-CoMo	32.43	49.65	65.49	82.50
1CeO$_x$-Si-CoMo	64.89	70.71	93.46	97.93
2.5CeO$_x$-Si-CoMo	73.54	90.42	94.6	98.14
5CeO$_x$-Si-CoMo	29.40	47.94	64.94	88.9
10CeO$_x$-Si-CoMo	36.11	50.72	83.86	89.85

Table 3. 8: Effect of process temperature for 2.5CeO$_x$-Si-CoMo (5 MPa; DBT=1000 ppm; reaction time = 4 h).

Temperature (^{o}C)	**Percent sulfur removal (%) at different temperature**			
	1h	**2h**	**3h**	**4h**
325	64.58	75.01	87.23	95.46
350	73.54	90.42	94.6	98.14
375	99.27	100	100	100

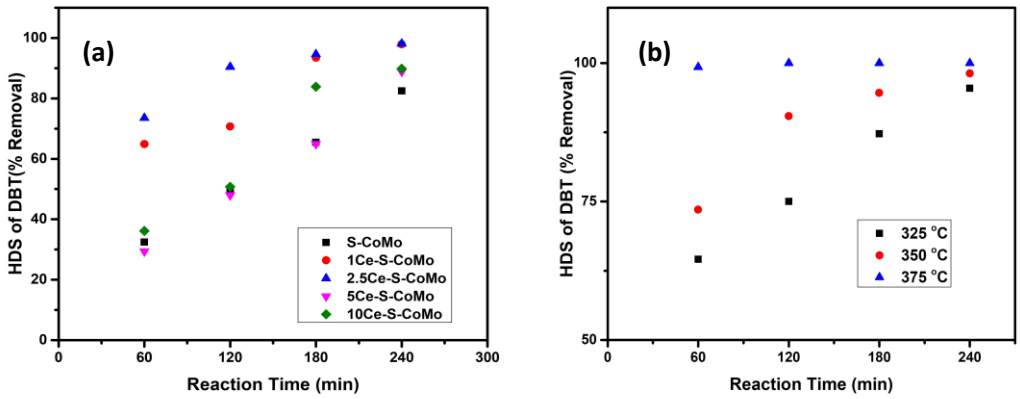

Figure 3. 12: (a) Plot of HDS performance of CeO_x-Si-CoMo catalysts and (b) effect of process temperature on the HDS performance of 2.5CeO_x-Si-CoMo.

3.3.3 Reaction pathways

The mechanism of HDS of DBT has since been documented [114]. The reaction is reported to occur via two pathways: direct desulfurization (DDS) that involves direct C-S bond cleavage (one-step) to form biphenyl (BP); and hydrogenation (HYD) of phenyl ring to cyclohexyl in 2-3 steps, then C-S bond cleavage to form cyclohexyl benzene (CHB) [115]. Detailed study of the products distribution formed after 1 h of HDS reaction is summarized in **Table 3.9**. Close observation of the product distribution revealed a trend in the BP formation across all the studied catalysts. It was noticed that the amount of BP decreases when up to 2.5 wt.% Ce was incorporated to SBA-15. However, when the Ce loading reached 5, the %BP increases and at 10 wt.%, the %BP has reached almost the same amount as that of Si-CoMo. Similarly, the ratio of BP to CHB maintained the same trend as observed in BP. It therefore means that Ce plays a role in the choice of the reaction pathway, and apparently, it tends to lead the reaction to the HYD pathway as evidenced in the %CHB increase due to ceria loading up to 2.5 wt.%. This makes 2.5CeO_x-Si-CoMo a good catalyst for the HDS of highly refractory sulfur compounds such as dialkyldibenzothiophenes which are known to be desulfurized mainly via the HYD pathway [116]. The observed disparity in the product selectivity can be correlated to the catalysts active sites using the Rim-Edge model. According to the model, rim sites favors the HYD pathway and edge sites only favor the DDS. The rim sites are characterized with low intensity of the (002) XRD peak and decreased stacking of MoS_2 slab [112]. The very low (002) XRD peak and the lower average stacking layers of MoS_2 observed in the 2.5CeO_x-Si-CoMo suggests that 2.5 Ce wt.% favors the formation of rim sites of MoS_2 slabs. The effect of temperature variation on the product distribution using 2.5CeO_x-Si-

CoMo catalyst is presented in **Table 3.10**. It was noticed that the %CHB increases with increase in temperature, therefore resulting in decreased BP/CHB. Typically, the DDS pathway can be further modified to include a sequential HYD of BP to CHB, and although the model (DBT→BP→CHB) is less probable, it has been used to explain the increased %CHB at high temperature [17].

Table 3. 9: Catalyst performance results: Product Distribution (%) after 1h. (Process conditions: 350 ^{o}C; 5 MPa; DBT=1000 ppm).

Catalysts	**Product distribution (%)**				
	CPB	**CHB**	**BP**	**THDBT**	**BP/CHB**
Si-CoMo		5.54	94.46	-	17.05
1CeO$_x$-Si-CoMo	-	13.82	86.18	-	6.24
2.5CeO$_x$-Si-CoMo	-	15.53	84.47	-	5.44
5CeO$_x$-Si-CoMo	-	9.68	87.90	2.42	9.08
10CeO$_x$-Si-CoMo	-	6.14	93.84	-	15.28

Table 3. 10: Catalyst performance results: Product distribution (%) after 1h for 2.5CeO$_x$-Si-CoMo at varying temperatures (Process conditions: 5 MPa; DBT=1000 ppm).

Temp (^{o}C)	**Product distribution (%)**				
	CPB	**CHB**	**BP**	**THDBT**	**BP/CHB**
325		14.46	85.54	-	5.92
350	-	15.53	84.47	-	5.44
375	-	16.05	83.95	-	5.23

3.3.4 Kinetics Study

The kinetic study is performed on the assumptions that the HDS reaction occur completely via the parallel pathway, and that the reaction rate is calculated based on the pseudo-first order kinetics. Thus, the rate constants of the HDS reaction, $\mathbf{k}_{HDS}$ (min^{-1}); rate constant of DDS, $\mathbf{k}_{DDS}$ (min^{-1}); and rate constant of HYD, $\mathbf{k}_{HYD}$ (min^{-1}) were established and presented in **Table 3.11**. The $\mathbf{k}_{HDS}$ (min^{-1}) for Si-CoMo catalyst has a value of 6.53 x 10^{-3}, and therefore compares well with the $\mathbf{k}_{HDS}$ (8.4 x 10^{-3} min^{-1}) we recently reported for Ti-modified SBA-NiMo catalyst prepared and sulfided under the same condition [51]. The role of Ce in the catalysts can also be expressed based on the rate constants of the HDS reaction. It was observed that the $\mathbf{k}_{HDS}$ (min^{-1}) increased by a factor of 3.4 from Si-CoMo to 2.5CeO_x-O-Si-CoMo catalysts. The increase in $\mathbf{k}_{HDS}$ (min^{-1}) was in-tandem with an increase in $\mathbf{k}_{HYD}$ (min^{-1}), thus resulted in decreased $\mathbf{k}_{DDS}/\mathbf{k}_{HYD,}$ as observed in the product distribution BP/CHB in **Table 3.9**. However, above 2.5 Ce wt.%, the $\mathbf{k}_{HDS}$ (min^{-1}) and $\mathbf{k}_{HYD}$ (min^{-1}) decreased significantly. The effect of temperature on the $\mathbf{k}_{HDS}$ (min^{-1}) for 2.5CeO_x-Si-CoMo catalyst was studied. As shown in **Table 3.12**, increase in process temperature significantly increases the $\mathbf{k}_{HDS}$ (min^{-1}) (by a factor of 3.7 from 350 to 375 ^oC), however, it also increases the HYD pathway, thus leads to decrease in $\mathbf{k}_{DDS}/\mathbf{k}_{HYD}$.

Table 3. 11: Pseudo first-order rate constants for HDS of DBT after 1 h reaction time at 350 ^{o}C.

Catalysts	**k_{HDS} x 10^3 (min^{-1})**	**k_{DDS} x 10^3 (min^{-1})**	**k_{HYD} x 10^3 (min^{-1})**	**k_{DDS}/k_{HYD}**
Si-CoMo	6.53	6.17	0.36	17.14
1CeO_x-Si-CoMo	17.44	15.03	2.41	6.24
2.5CeO_x-Si-CoMo	22.16	18.72	3.44	5.44
5CeO_x-Si-CoMo	5.80	5.23	0.58	9.02
10CeO_x-Si-CoMo	7.47	7.01	0.46	15.24

Table 3. 12: Effect of temperature on first-order rate constants for HDS of DBT (catalyst = 2.5CeO_x-Si-CoMo).

Temperature (^{o}C)	**k_{HDS} x 10^3 (min^{-1})**	**k_{DDS} x 10^3 (min^{-1})**	**k_{HYD} x 10^3 (min^{-1})**	**k_{DDS}/k_{HYD}**
325	17.30	14.80	2.50	5.92
350	22.16	18.72	3.44	5.44
375	82.00	68.64	13.16	5.22

Overall, it can be stated that the HDS activity of 2.5CeO_x-Si-CoMo catalyst is better than Si-CoMo evidenced from the $\mathbf{k}_{HDS}$ (min^{-1}) values, and in fact the 2.5CeO_x-Si-CoMo is the best performing catalyst among the series of CeO_x-Si-CoMo catalysts. The performance of 2.5CeO_x-Si-CoMo catalyst is connected to its textural properties and the moderate metal-support interaction observed from the XRD, Raman spectroscopy and H_2-TPR results that resulted to better metal dispersion on the support.

3.3.5 Kinetic Modeling

The role of ceria loading on catalysts activity and product selectivity can be further understood by using the kinetic modeling [13]. Based on the experimental data for the catalyst's performance at 350 °C, the triangular reaction network presented in **Fig. 3.13** was proposed.

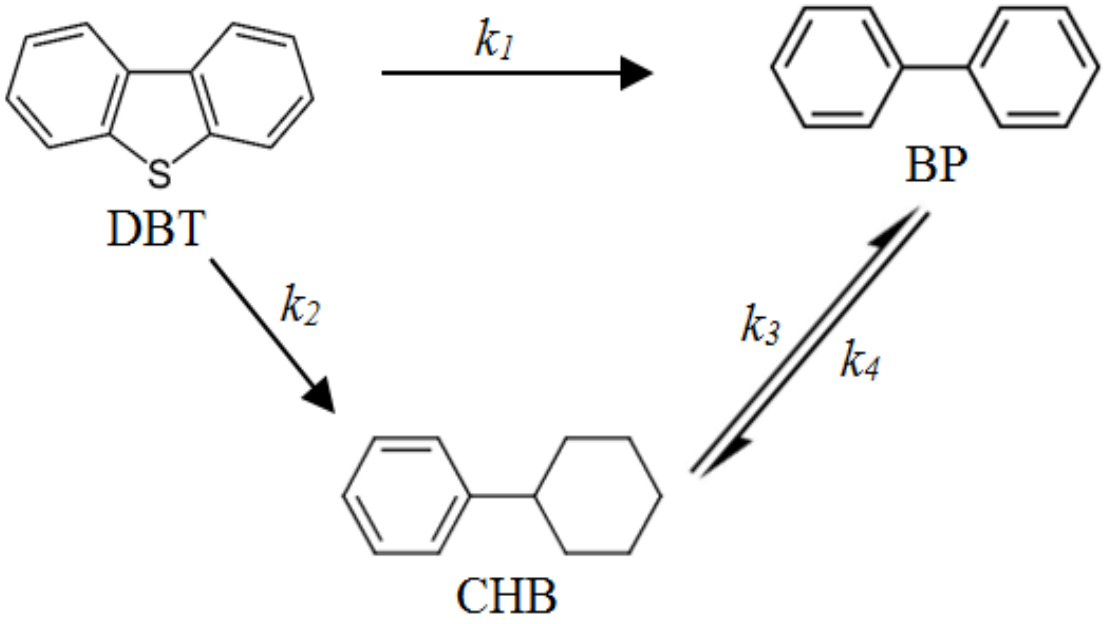

Figure 3. 13: Proposed reaction mechanism for the HDS of DBT to CHB and BP over a CeO_x-Si-CoMo at 350 ^oC and 5 MPa.

The justification for suggesting this new mechanism will be explained in detail. DBT was converted to BP and CHB through the irreversible steps at specific reaction rates k_1 and k_2 respectively. It should be noted however, that unlike the HYD/DDS scheme, the product distribution obtained in this work showed negligible amounts of 4HDBT, implying its instantaneous transformation to CHB. Moreover, preliminary analysis on a non-reversible conversion of BP to CHB gave a very high specific rates for the formation of BP from DBT, and a very nominal value for the specific rate of conversion of BP to CHB. In order words, the time-varying concentrations of BP indicate that BP was formed from both DBT and CHB. Therefore, we proposed the reaction network shown in **Fig. 3.13**. Now, we can write the rate equations as follows.

$$-\frac{dC_{DBT}}{dt} = (\boldsymbol{k_1 + k_2})\boldsymbol{C_{DBT}} \text{----------} \quad (3.1)$$

$$\frac{dC_{BP}}{dt} = \boldsymbol{k_1 C_{DBT} + k_3 C_{CHB} - k_4 C_{BP}} \text{- - - - - - - - -} \quad (3.2)$$

$$\frac{dC_{CHB}}{dt} = \boldsymbol{k_2 C_{DBT} - k_3 C_{CHB} + k_4 C_{BP}} \text{- - - - - - - - -} \quad (3.3)$$

Equation 3.1 is a simple pseudo-first order disappearance of the DBT. Similar rate expression was reported in the literature [51]. This equation could be solved numerically to give a time-dependent function for the DBT concentration as $C_{DBT} = C_{DBT0}e^{-k_0 t}$. Where, $k_0 = k_1 + k_2$, and C_{DBT0} is the initial concentration of DBT. The implication is that, k_0 could be determined separately and independent of equations 3.2 and 3.3. Hence, in seeking the solution to equations (3.2) and (3.3), we have a mathematical constraint that $k_0 = k_1 + k_2$. This constraint is very important, and it means that both k_1 and k_2 must be

less than k_0. This constraint enabled us to figure out that indeed BP was partly formed from CHB. Eventually, equations 3.1 – 3.3 were solved simultaneously in Mathematica™ to determine a global solution for the rate constants. The criteria for accepting the model were high values of coefficient of determination (R^2), and low sum square error (*SSE*) between experimental and model predictions.

The comparison between the experimental and calculated concentrations of DBT, BP and CHB over the CeO_x-Si-CoMo catalysts were presented in **Fig. 3.14**, and the parity plots experimental and modeled DBT concentrations for the CeO_x-Si-CoMo catalysts were shown in **Fig. 3.15**. The data show very good agreement between the experimental data and the proposed kinetic model. In each case, the coefficient of determination, R^2 is greater than 0.98. The results from calculated rate constants (**Table 3.13**) show that 2.5CeO_x-Si-CoMo performs best in the HDS of DBT under the same operating conditions. In addition, the 2.5CeO_x-Si-CoMo catalyst shows the largest amount of k_2, which implies that the catalyst directs the reaction towards the hydrogenation pathway as was observed in the experimental results.

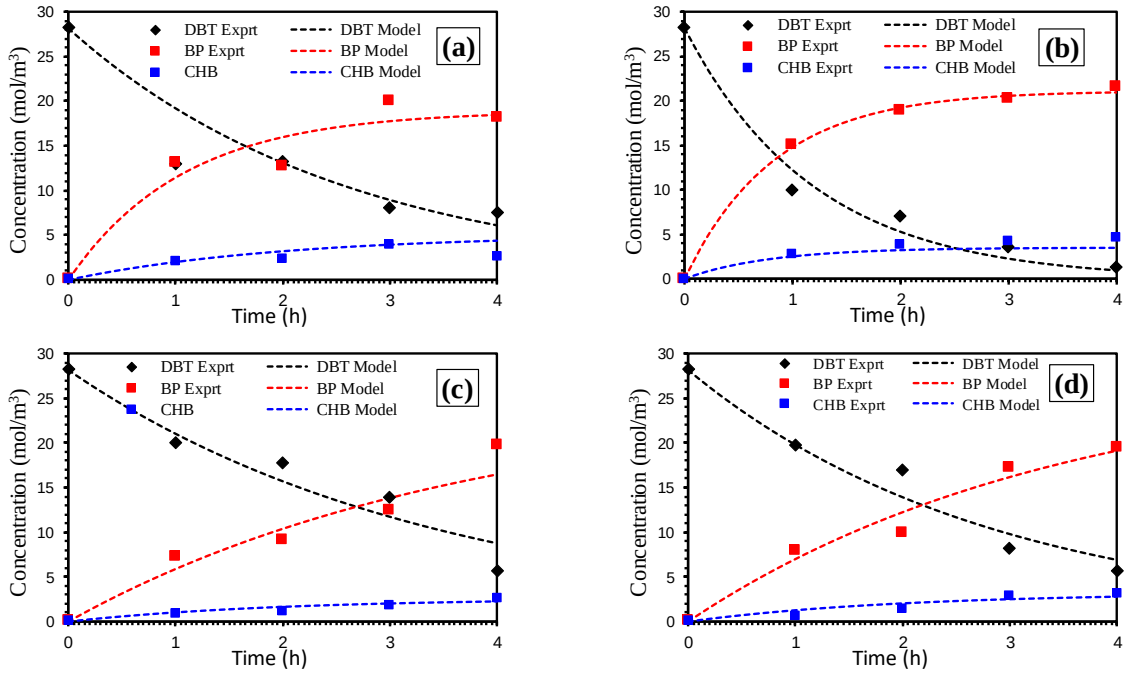

Figure 3. 14: Concentrations as a function of time of species during HDS of DBT over (a) $1CeO_x$-Si-CoMo; (b) $2.5CeO_x$-Si-CoMo; (c) $5CeO_x$-Si-CoMo; (d) $10CeO_x$-Si-CoMo at 350 ^oC and 5 MPa.

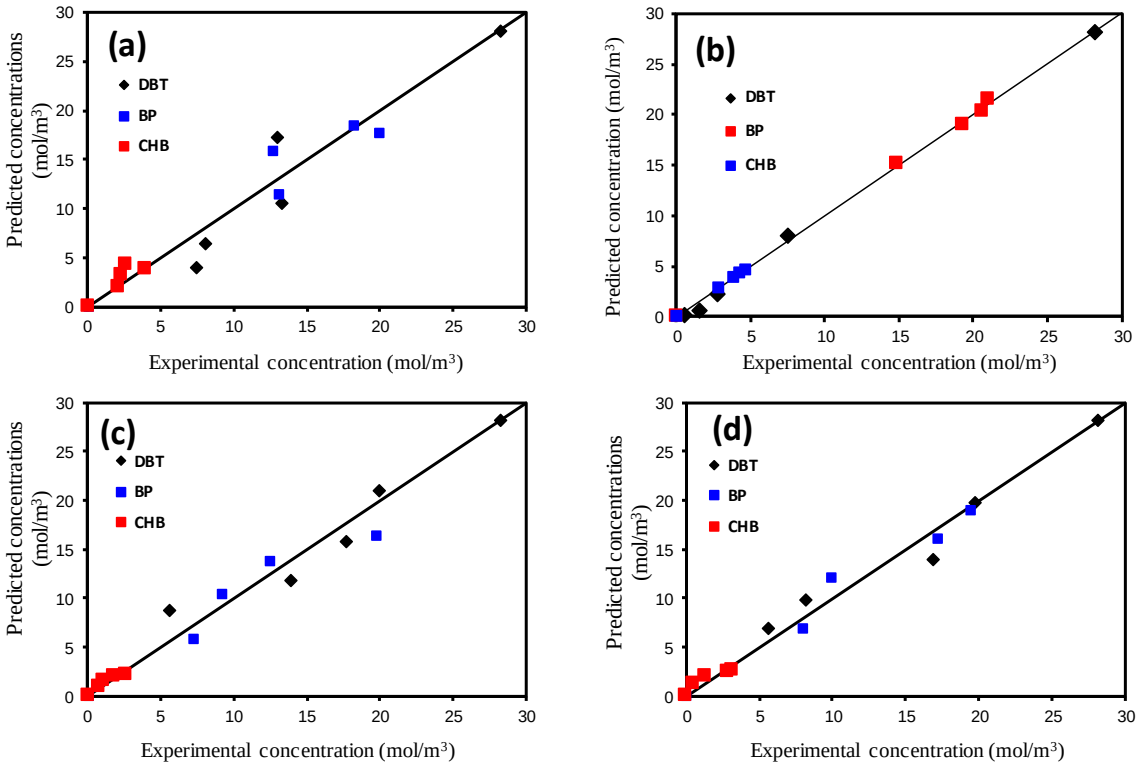

Figure 3. 15: Parity diagrams for the comparison of experimental to calculated concentrations of species during HDS of DBT over (a) $1CeO_x$-Si-CoMo; (b) $2.5CeO_x$-Si-CoMo; (c) $5CeO_x$-Si-CoMo; (d) $10CeO_x$-Si-CoMo at 350 ^oC and 5 MPa.

Table 3. 13: Modeled first-order rate constants for HDS of DBT after 1 h reaction time at 350 ^{o}C.

Parameter	**1CeO$_x$-Si-CoMo**	**2.5CeO$_x$-Si-CoMo**	**5CeO$_x$-Si-CoMo**	**10CeO$_x$-Si-CoMo**
***k*$_0$ x 10^{-3} (s^{-1} g^{-1} catalyst)**	5.51	14.07	3.21	3.92
***k*$_1$ x 10^{-3} (s^{-1} g^{-1} catalyst)**	5.40	10.06	2.57	3.32
***k*$_2$ x 10^{-3} (s^{-1} g^{-1} catalyst)**	0.11	4.01	0.65	0.61
***k*$_3$ x 10^{-3} (s^{-1} g^{-1} catalyst)**	11.20	1.07	4.38	1.94
***k*$_4$ x 10^{-3} (s^{-1} g^{-1} catalyst)**	2.67	0.11	0.11	0.11

3.4 Conclusion

Series of CeO_x-Si supports, and CeO_x-Si-CoMo catalysts have been prepared with different Ce weight percent loading by hydrothermal synthesis method. The characterized results confirmed that up to 2.5 wt.% Ce can be incorporated into the framework of SBA-15, and larger wt.% were rather incorporated into the extra framework of the SBA-15. In addition, it was established by XRD, Raman spectroscopy, H_2-TPR and XPS that the 2.5CeO_x-Si-CoMo catalyst has better active sites (MoS_2 phases) for HDS. Ce loading up to 2.5 wt.% facilitate the reduction of MoO_3 and prevent the formation of the inactive $CoMoO_4$ phase, which results in better Mo reduction and dispersion. Consequently, the 2.5CeO_x-Si-CoMo showed exceedingly better HDS performance than Si-CoMo and the other CeO_x-Si-CoMo catalysts in the series. Furthermore, even at a lower process temperature (325 ^oC) for HDS, the 2.5CeO_x-Si-CoMo catalyst performed almost twice better than Si-CoMo (at 350 ^oC), and at higher process temperature of 375 ^oC, 99.27% DBT has already been removed at the first one hour of reaction with 2.5CeO_x-Si-CoMo catalyst. Therefore, 2.5CeO_x-Si-CoMo as HDS catalyst has demonstrated better efficiency and shows a potential to be used as industrial catalyst more than the Si-CoMo catalyst.

CHAPTER 4

SYNERGY OF ZrO_x-CeO_y ON ACTIVE SITES FORMATION OF NiMoS CATALYST SUPPORTED ON SBA-15 FOR HYDRODESULFURIZATION OF DIBENZOTHIOPHENE IN DIESEL

ABSTRACT

Development of highly robust catalysts for the hydrodesulfurization (HDS) of diesel fuel has recently become an area of special interest. In this study, SBA-15 modification based on ZrO_x incorporation and Mo loading was performed in a one-step approach. The dried catalyst is subsequently impregnated with CeO_y and/or Ni promoter in a second step. The catalysts' activity was tested in the HDS of dibenzothiophene (DBT) in a commercial diesel. Catalytic parameters such as surface area and acidity, number of active sites and dispersion are greatly influenced by the ZrO_x-CeO_y modification of SBA-15 supported (Ni)Mo catalysts. The BET surface area of ZrO_x-CeO_y modified catalyst was enhanced due to the support modification. The py-FTIR and NH_3-TPD showed that the surface acidity and number of active sites of the catalysts increased when ZrO_x and CeO_y were incorporated to the SBA-15 support, and the XPS analysis proved the presence of MoS_2 in large amount in ZrO_x-CeO_y modified catalyst than in the other supported catalysts. The catalytic performance test shows that ZrO_x-CeO_y modified catalyst has the highest HDS activity, and this is correlated to its structural properties such as large surface area, better acidic strength and increased number of active sites.

4.1 Introduction

The recent strict environmental regulations limiting the level of sulfur in the transportation fuel has prompted the need to develop highly active and stable hydrodesulfurization (HDS) catalysts [117]. Previous studies have shown tremendous improvement in the catalyst activity through changing the active metals [118] or addition of promoters to the active metal [22], synthesis route [119] and changing or modification of active metals support [120]. Textural and mechanical properties, high active metal dispersion and low cost have made γ-Al_2O_3 the most widely acceptable catalyst support for many industrial catalysts including the HDS catalyst. However, a big drawback of γ-Al_2O_3 is that it shows strong metal-support interaction with the active metals [40]. This considerably affects catalytic performance of HDS catalyst. Mesoporous silica-based support materials such as SBA-15 and MCM-41 have shown great improvement when used in HDS process [23]. This is due to their weak metal support interaction, but also their ordered structure, high surface area and porosity. Although SBA-15 have shown great potential in HDS, researchers have recently observed that the overall catalyst activity can further be improved by its modification. Different modification strategies such as addition of heteroatoms, additives and choice of solvent have been reported [121]. Heteroatoms that are Lewis acid such as zirconia, titania and alumina increase the metal support interaction from weak (which is known for silica) to moderate by increasing the acidity of the SBA-15 [79]. Different synthesis approach has been explored to incorporate heteroatoms to SBA-15 and their effect on catalyst HDS performance reported [48,49,83,84]. Chelating agents such as ethylenediaminetetraacetic acid and citric acid have impact greatly on the HDS performance of the catalysts [122]. Badoga et al. studied the combined effect of EDTA and heteroatoms (Ti, Al and Zr) on the catalytic performance of an SBA-15 supported NiMo

catalyst for hydrotreating applications [41]. Single heteroatom incorporation in the framework of SBA-15 have shown great potential to increase the catalytic activity of hydrotreating catalysts [51]. Perhaps by modifying SBA-15 with two heteroatoms, the active metal dispersion and catalytic activity can be greatly enhanced. However, there is rare reference in the literature on the effect of incorporating two heteroatoms in the framework of SBA-15. The study by Chandra et al. reported low hydrotreating performance of Ti-Zr-SBA-15 NiMo catalyst due to the presence of tetrahedral MoO_4 phase which inhibit the formation of the Ni-Mo-S type II active phase [56]. According to the authors, the $[MoO_4]^{2-}$ was stabilized by the relative positive charge of ZrO_x site arising from the electronegativity difference between Ti and Zr. Motivated by this, we adopted the idea of using a less electronegative heteroatom, Ce to replace more electronegative Ti to form the ZrO_x-CeO_y modified SBA-15 supported NiMo catalyst. CeO_y has also been explored to modify the support properties of SBA-15 and the modified supported CoMo catalyst has demonstrated excellent HDS performance [123]. With focus to understanding the role of each heteroatom and the combined effect of bi-heteroatoms, series of ZrO_x-SBA-15 and ZrO_x-CeO_y-SBA-15 (Ni)Mo catalysts have been prepared and characterized. In our previous studies, we highlighted that Ni leaching was observed in single-pot synthesis approach and therefore we proposed post-synthesis introduction of Ni to a single-pot synthesized SBA-15 supported Mo catalyst oxide in this study [51]. Therefore, single-pot approach was adopted to prepare SBA-15-Mo and ZrO_x-SBA-15-Mo, and the Ni and CeO_x were introduced into the pre-calcined catalysts by post synthesis approach. The effect of calcination of the developed catalysts prior to sulfidation/activation on the metal dispersion and activity is also studied.

4.2 Experimental Section

4.2.1 Materials

Tetraethoxysilane (TEOS), zirconium (iv) butoxide (80%), pluronic P123, nickel (ii) nitrate hexahydrate, DBT (98%) and dodecane were purchased from Sigma-Aldrich. Ammonium molybdate (vi) tetrahydrate (99%) was bought from ACROS organics, USA. Ammonium cerium (iv) nitrate, was ordered from Riedel-de Haen AG, USA. Deionized water was generated in-house using Thermo Scientific Barnstead NANOPURE after distillation with a Labstrong FiSTREEM^{TM} II Glass Still distillater.

4.2.2 Single-pot Synthesis of SBA-15-Mo and ZrO_x-SBA-15-Mo catalysts

The SBA-15 step-by-step preparation method has previously been reported [52]. Modification of SBA-15 with ZrO_x (20:1 SBA-15:ZrO_x) and the incorporation of active Mo metal species was carried out following our previously reported single pot synthesis approach [51]. ZrO_x-SBA-15 was prepared by dropwise addition of 0.234 g of Zirconium (iv) butoxide to a mixture of 4.16 g TEOS, 2g pluronic P123, 10.3 mL hydrochloric acid and 65 mL deionized water after stirring for 2 h. The mixture, which was kept at 40 ^{o}C, was stirred continuously for 24 h before addition of an aqueous solution of 13 wt.% Mo. After stirring for 30 min, the mixture was transferred to a Teflon autoclave for hydrothermal synthesis in an oven preconditioned at 90 ^{o}C. The autoclave was kept in the oven for additional 24 h before centrifuging and drying at 100 ^{o}C for 10 h.

4.2.3 Materials

The dried pre-calcined SBA-15-Mo and ZrO_x-SBA-15 catalysts were first re-dispersed in deionized water. Then solution of 0.191 g of ammonium cerium nitrate (20:1 SBA-15:CeO_y) and/or 0.595 g (3 wt.%) nickel (ii) nitrate hexahydrate were added to the suspension and stirred at 40 ^oC until the water is nearly evaporated. The mixture was dried in air and later in an oven at 100 ^oC for 24 h. Detailed description of the prepared catalysts is presented in **Table 4.1**. The powdered metal oxide catalysts were pelletized to within 300 -500 microns.

Table 4. 1: Catalysts description.

Code	Description
SM	SBA-15 supported Mo
ZrSM	ZrO_x modified SBA-15 supported Mo
ZrSMN	ZrSM impregnated with Ni
ZrCeSM	ZrSM impregnated with CeO_y
ZrCeSMN	ZrSM impregnated with CeO_y and Ni
ZrCeSMN-C	Calcined ZrCeSMN

4.2.4 Characterization of Supported Catalysts

The catalysts surface area, pore size and pore volume were measured on a Micromeritics ASAP 2020 using N_2 adsorption-desorption isotherms at 77k. Before the measurement, the catalysts were degassed with a vacuum at 250 ^oC for 3 h to remove impurities. Brunauer, Emmett, and Teller (BET) method was used to calculate the surface area, and adsorption branch of Barrett, Joyner, and Halenda (BJH) method was applied to calculate the pore size and pore volume of the catalysts. The catalysts' crystallinity and the nature of their active metal phases on the supports were determined by recording their X-ray diffraction pattern between 20 – 80 ^{o} at 2θ using Rigaku Ultima IV X-ray diffractometer. The operation was performed at 40 kv and 40 mA with a scanning speed of 10 ^{o}/min and 0.03 width. The catalysts FTIR spectra were recorded on a Nicolet 6700 FTIR spectrometer within a wavelength range of 400 – 4000 cm^{-1}. Prior to the FTIR analysis, the catalysts were mixed in 1:100 ratio with KBr and pelletized using the hydraulic press pelletizer. The formed tiny pellets were inserted into the FTIR cell for analysis. The nature and amount of catalysts surface acidity were determined using an in-situ pyridine FTIR (with self-supported wafer). The samples, placed in a *Specac* cell, were pretreated under vacuum of 1.33×10^{-3} Pa at 300 ^oC for 1 h, and pyridine vapor adsorption at 150 ^oC for 30 min. Excess pyridine vapor was expelled from the treated samples by degassing at 200 ^oC, and the total acidity due to Lewis and Bronsted acid sites were recorded. Ammonia TPD (NH_3-TPD) was utilized to measure the acidic property of the catalysts. The measurements were conducted on a micromeritics Chemisorp 2750 using 10 wt.% NH_3. Approximately 100 mg of the catalysts in their oxide form was loaded into a quartz tube high purity helium was purged through the tube at 600 ^oC for 30 min, then cooled to 100 ^oC. Thereafter, NH_3 was passed through

the samples for 30 min at 100 ^{o}C, followed by helium for 60 min to remove excess NH_3 that is physically adsorbed. The temperature was raised to 900 ^{o}C at 10 ^{o}C/min in order to desorb the ammonia, and the thermal conductivity detector (TCD) signal was recorded against the desorption temperature. The reducibility of the metal oxides in the catalysts by H_2 was determined by temperature-programmed reduction with hydrogen as a probe molecule. The analysis was carried out using an AutoChem II – 2920 Micromeritics Chemisorption analyzer. Before the analysis, about 100 mg of the catalyst was heated to 500 ^{o}C for one hour under a steady flow of high purity helium to remove impurities, and later cooled to room temperature under the same condition of helium flow. Then the system gas flow was switched to 10 % H_2 in helium and the temperature was raised to 1000 ^{o}C at 10 ^{o}C/min ramping. Under these conditions, the amount of H_2 consumed at the reducible temperatures was recorded. The catalysts surface morphologies were recorded on a Field Emission Scanning Electron Microscope FESEM (TESCAN, LYRA 3) using a secondary electron (SE) and the back scattered electron (BSE) mode at an accelerating voltage of 20 kV. The different Mo bonding states and their binding energies in the sulfided catalysts were determined by X-ray photoelectron spectroscopy (XPS) using PHI 5000 Versa Probe II, ULVAC-PHI Inc. spectroscope. Disc pelletized catalysts samples prepared using hydraulic press pelletizer were first subjected to high vacuum before the XPS analysis.

4.2.5 Catalysts Presulfidation and Performance Evaluation

All the pelletized catalysts were presulfided without prior calcination except for ZrCeSMN, which some portion of it was calcined to allow comparison of sequential calcination and reduction approach to the simultaneous calcination and reduction approach. The presulfidation was carried out in quartz tubular furnace after the simultaneous calcination

and reduction of the Mo and NiMo metal oxides in the catalysts under the flow of 10% H_2 in helium at 400 ^oC. After reduction, the furnace temperature was brought down to 350 ^oC and a 2 wt.% CS_2 solution in cyclohexane was flowed through the furnace at 0.5 mL/min for 5h.

HDS performance study of the presulfided catalysts was carried out in a Parr 4576B batch reactor operated at 350 ^oC, 5 MPa H_2 pressure and 300 rpm stirring rate. Roughly 100 mg of the presulfided catalyst was added to 100 mL of locally obtained commercial diesel spiked with 1000 ppm DBT. The reaction was performed for 5 h after the reaction conditions have been stabilized, and product sampling were done at an hour interval.

4.3 Results and Discussion

4.3.1 Characterization Results

The BET surface area, pore size and pore volume of catalysts are important parameters usually employed to have some understanding of the catalytic performance behavior demonstrated by the catalysts [92]. In this study, the developed catalysts' textural properties were measured and summarized in **Table 4.2**. The BET surface area of SM is 245.9 m^2/g and it was observed that by incorporation of ZrO_x the surface area increased to 260.64 m^2/g. The observed trend shows that incorporation of ZrO_x leads to increased surface area possibly due to its large atomic size as compared to Si. Similar phenomenon was observed when TiO_x was incorporated to the SBA-15 support [124]. However, subsequent addition of Ni to form ZrSMN catalyst resulted in slight decrease in the surface area and this was attributed to the blockage of the void spaces within the support framework. The combined effect of biheteroatoms on the surface area was investigated by

addition of CeO_y to the ZrSM to form ZrCeSM. It was observed that CeO_y incorporation further increased the surface area of ZrSM and did not significantly affect it porosity. Similar result was observed in our previous work when the SBA-15 framework was modified with CeO_y [125]. Interestingly however, simultaneous introduction of CeO_y and Ni to the ZrSM results in only slight drop in the surface area (from 327.6 m^2/g for ZrCeSM to 316.76 m^2/g for ZrCeSMN) which is again due to void blockage as a result of Ni incorporation. It is noteworthy that incorporation of ZrO_x and CeO_y to the SBA-15 support, and the active (Ni)Mo species did not disrupt the mesoporosity nature of the support significantly as all catalysts' isotherms follow the H1 hysteresis loop **(Fig. 4.1(a))**. Subsequent calcination of the ZrCeSMN for 5 h to form ZrCeSMN-C significantly decreased the surface area to 226.86 m^2/g, even though it resulted to an increase in average pore size as shown in **Fig. 4.1(b)**. The decrease in surface area due to calcination is associated with metal sintering and formation of crystallites that blocked the support surface [126]. Based on the surface area results of the catalyst series, it can be envisaged that there is electronic and structural interaction between ZrO_x and CeO_y in ZrCeSMN catalyst which results in large surface area and pore volume of the catalyst.

Table 4. 2: Textural properties of catalysts.

Catalyst	BET Surface Area (m^2/g)	Microporous Surface Area (m^2/g)	External Surface Area (m^2/g)	Microporous Pore Volume (cm^3/g)	Total Pore Volume (cm^3/g)	Average Pore Size (nm)
SM	245.9	31.9	214	0.0158	0.408	6.11
ZrSM	287.63	33.1	254.4	0.0165	0.499	6.05
ZrSMN	260.64	26.6	244.08	0.0131	0.451	5.54
ZrCeSM	327.57	33.2	287.56	0.0167	0.489	5.63
ZrCeSMN	316.76	33.8	282.97	0.0169	0.511	5.85
ZrCeSMN-C	226.86	27.5	199.38	0.0136	0.436	6.66

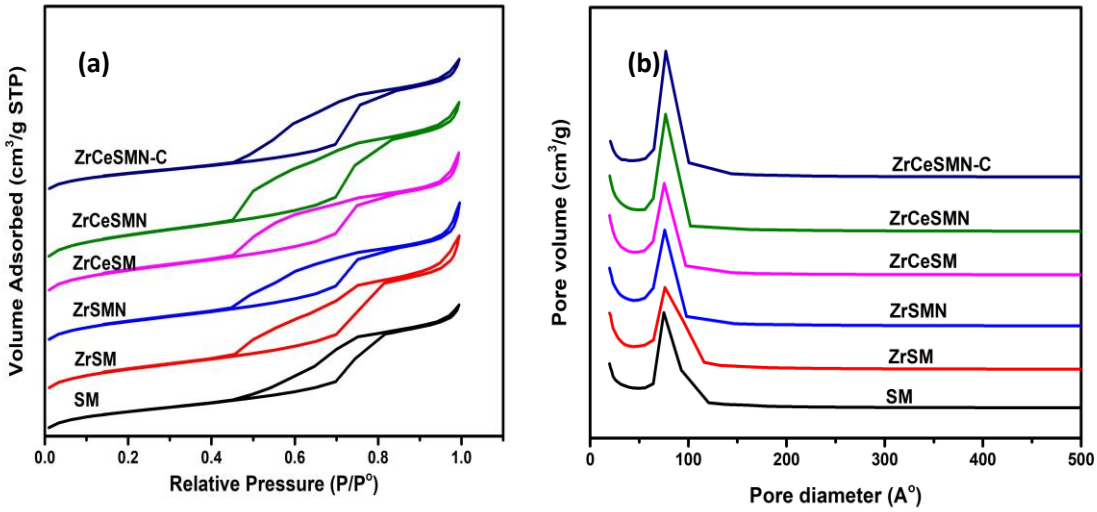

Figure 4. 1: (a) N_2 adsorption-desorption isotherm and (b) pore volume-size distribution for the Zr and ZrCe-modified SBA-15 supported NiMo catalysts.

The XRD pattern of the sulfided catalysts is presented in **Fig. 4.2**. Generally, the pattern of the XRD gives insight on the phases of the active species and their dispersion on the support [127]. From **Fig. 4.2,** it was observed that all the catalysts showed a broad diffraction pattern at approximately 25 ^{o} 2θ, a distinctive property of amorphous silica due to the SBA-15 support [94]. The absence of diffraction patterns characteristics of ZrO_x and CeO_y indicates that the oxides are incorporated into the SBA-15 framework or at best are in small quantity and therefore undetectable. Careful observation also shows that all the catalysts except ZrCeSMN-C have good dispersion of the Mo or NiMo active species due to the absence of their metal crystallite peaks. However, the presence of small and unresolved peak in ZrCeSMN-C at approximately 35 ^{o} 2θ hinted the presence of Mo crystallites due to agglomeration (because of calcination effect) in the catalyst which is responsible for the lower surface area observed in the textural properties study.

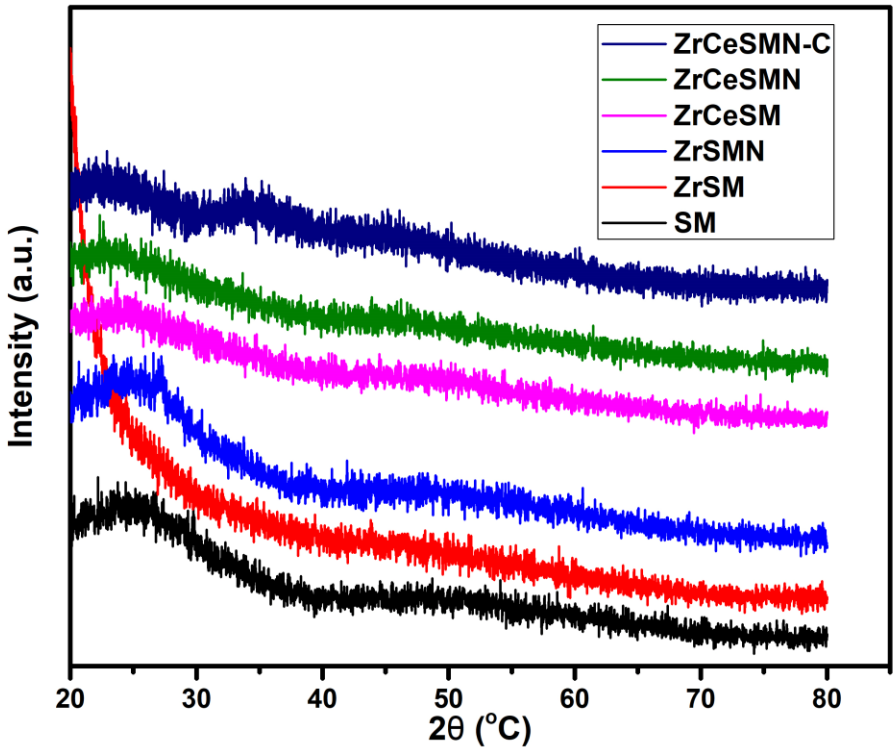

Figure 4. 2: Wide angle XRD pattern of the Zr and ZrCe-modified SBA-15 supported NiMo catalysts.

FTIR spectroscopy was performed to have some idea about the functional groups present in the sulfided catalysts. The FTIR spectra of the catalysts (in their sulfided form) is shown in **Fig. 4.3(a)**. All the catalysts show broad adsorption band at 3500 cm^{-1} which was assigned to the stretching vibration of Si-OH of the SBA-15 and O-H of the adsorbed water molecules. The water molecule O-H bending vibration peak was also observed at 1600 cm^{-1}. It was noted that these adsorption bands increase slightly from SM to ZrCeSMN. This trend is partially correlated to the catalysts total pore volume; thus, the larger pore volume catalyst is likely to attract more atmospheric moisture. This supports the textural properties results discussed above, which demonstrated that ZrO_x and CeO_y incorporation to SBA-15 support increased both the support surface area and total pore volume. The ZrCeSMN-C catalyst, however, shows a significant decrease in the water molecule adsorption bands which is due to the catalyst calcination. The Si-O-Si stretching vibration band was observed within the range of 1150-1250 cm^{-1} in all the catalysts though at different intensities. The slight difference in Si-O-Si band wavelength and intensity in the catalysts is considered due to the incorporation of the ZrO_x and CeO_y which substitute the SiO_2 in Si-O-Si to form Si-O-Zr and Si-O-Ce respectively [101,128].

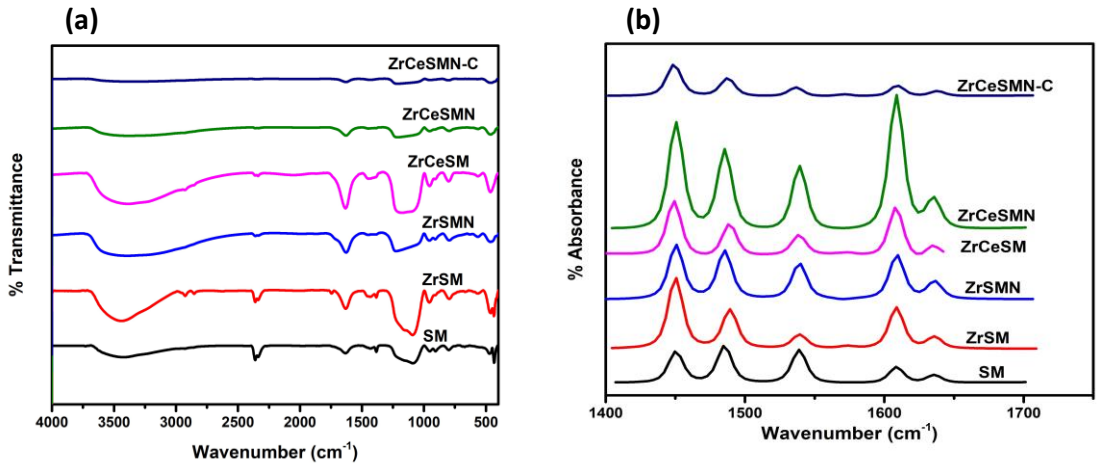

Figure 4. 3: (a) FTIR spectra: and (b) Py-FTIR of the Zr and ZrCe-modified SBA-15 supported NiMo catalysts.

The type, strength and amount of acidity in the sulfided catalysts was measured using the Py-FTIR. Typically, the free pyridine adsorption band is observed at frequency of 1582 cm^{-1}, and a shift to a range of 1590 – 1630 cm^{-1} indicates a Lewis acid sites [85,129]. The further away the shift is from the pyridine peak the more is the strength of the Lewis acidity. Bronsted acidity due to pyridine adsorption is observed at a frequency of 1540 cm^{-1}. The py-FTIR results presented in **Fig. 4.3(b)** shows the Lewis acid adsorption bands at 1450, 1610 and 1630 cm^{-1}, and the Bronsted acid adsorption band at 1540 cm^{-1}. The band at 1490 cm^{-1} indicates the interaction of pyridine with both Lewis and Bronsted acid sites. It was observed that the intensity of the acid sites (both Lewis and Bronsted) as well as the acid strength increases with the incorporation of the ZrO_x and CeO_y (see **Table 4.3**) except in ZrCeSMN-C where the high temperature calcination resulted in metals agglomeration. Thus, incorporation of biheteroatom increase the acidity of the catalysts that has not been subjected to high temperature calcination.

Table 4. 3: The distribution of the acidic sites in the catalysts obtained from py-FTIR.

Catalysts	**Lewis sites(µmol/g)**	**Brønsted sites (µmol/g)**	**B/L**
SM	105.8	256.8	1.43
ZrSM	197.0	373.5	0.89
ZrSMN	207.5	393.4	0.89
ZrCeSM	394.4	546.6	0.39
ZrCeSMN	480.6	835.7	0.74
ZrCeSMN-C	156.5	203.6	0.30

The NH_3-TPD is a complimentary technique to the pyr-FTIR and is often utilized to characterize the strength and available acid sites in catalysts [130]. The NH_3-TPD experiments were carried out to determine the acidic strength of the $ZrO_x(CeO_y)$-modified SBA-15 supported (Ni)Mo catalysts, and the obtained TPD profiles are shown in **Fig. 4.4(a)**. From the profiles, two main peaks were noticed at around 180 and 680 ^oC in all the catalysts. The peak at approximately 180 ^oC is considered the weakly acidic sites peak, while the peak at 680 ^oC is considered the strongly acidic sites peak [41]. Very small and unquantifiable peak was also noticed in all the catalysts at approximately 500 ^oC, which is characteristic medium acidic sites peak. The weak acidic sites were attributed to the surface hydroxyl group that are likely to be present in the catalysts' supports and can be considered the Bronsted acidity. The peak intensities were found to decrease with the incorporation of the ZrO_x and further addition of CeO_y as shown in **Table 4.4**. Conversely, the intensity of the strongly acidic sites peak was observed to increase due to the incorporation of the ZrO_x and CeO_y except for ZrCeSMN-C where the decrease in the strong acidic sites is attributed to the high temperature calcination. Overall, it can be concluded that the incorporation of ZrO_x and CeO_y heteroatoms to the SBA-15 support enhanced the acidic strength of the catalysts.

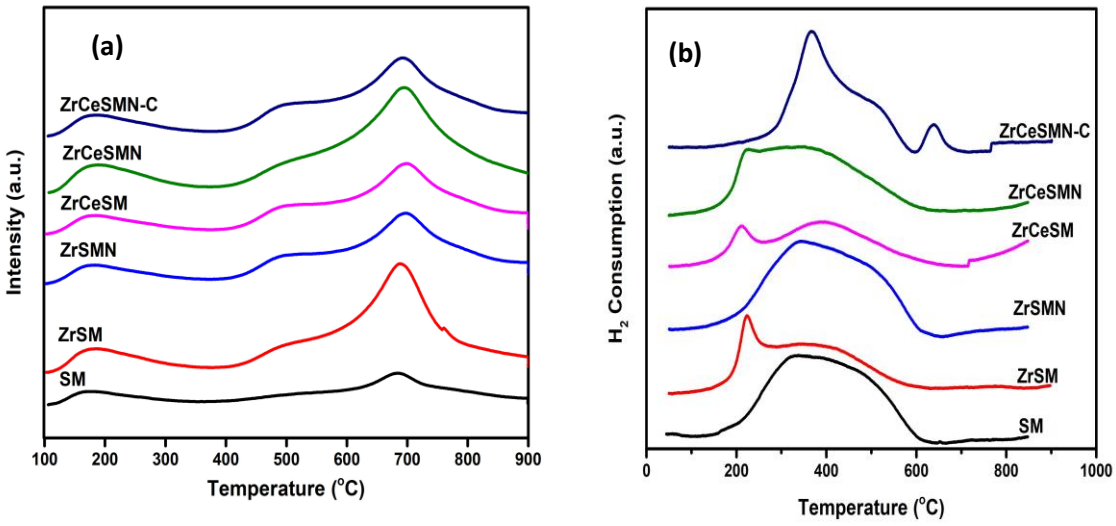

Figure 4. 4: (a) NH_3-TPD and (b) H_2-TPR of the Zr and ZrCe-modified SBA-15 supported NiMo catalysts.

Table 4. 4: Summary of NH_3-TPD and H_2-TPR of the catalysts.

NH_3-TPD			**H_2-TPR**	
Catalysts	**Peak Temp.(s)**	**Quantity (cm^3/g STP)**	**Peak Temp.(s)**	**Quantity (cm^3/g STP)**
SM	153, 688	42.2, 53.4	370	204.4
ZrSM	176, 688	18.2, 56.7	222, 391	27.8, 83
ZrSMN	185, 602	17.8, 56.9	384,	179
ZrCeSM	188, 696	9.3, 63.6	208, 393	18.8, 90.9
ZrCeSMN	186, 691	16.7, 82.8	227, 311, 337	30.1, 48.4, 103.5
ZrCeSMN-C	190, 688	9.1, 60.2	377, 639	149.3, 4.4

TPR is a powerful tool used to observe the reduction pattern of metal oxide catalysts. Here, the TPR was performed to understand the combined role of ZrO_x and CeO_y on the reducing behavior of the SBA-15 supported NiMo catalysts. As shown in **Fig. 4.4(b)** and **Table 4.4**, the TPR profile of SM shows a broad reduction peak at 370 ^oC and a shoulder peak at around 500 ^oC. These peaks are assigned to the reduction of Mo^{6+} species to Mo^{4+} and Mo^{4+} to Mo^0 respectively in the octahedrally coordinated species that are weakly bound to SBA-15 support [131]. After incorporation of ZrO_x and ZrO_x-CeO_y to the support, this reduction peak shifted to 391 ^oC and 393 ^oC respectively confirming an increase in the strength of the metal-support interaction. However, the addition of Ni promoter to the ZrSM and ZrCeSM lowers the reduction temperature of the Mo^{6+} species which further explains the role of Ni promoter in enhancing easier reduction and sulfidation of catalysts oxides. The high temperature reduction peak characteristic of Mo^{4+} to Mo^0 reduction gave an inconclusive pattern in all the catalysts as was similarly observed by Tatiana et al [131].

The FESEM images of the catalysts are displayed in **Fig. 4.5**. All the catalysts show the presence of micro-sized cylindrical rods characteristics of mesoporous SBA-15 [110]. Careful observation of the images shows that the size of the micro-sized rod decreases when ZrO_x and CeO_y are incorporated to the SBA-15 framework which is in line with the previously reported observations of modified mesoporous SBA-15 [51,52]. It was further observed that the micro-sized cylindrical rods in ZrCeSMN-C are stacked in multi-layers and this somewhat affect the dispersion of the active species on the modified support as is observed in the particle density due to NiMo loading on the catalyst.

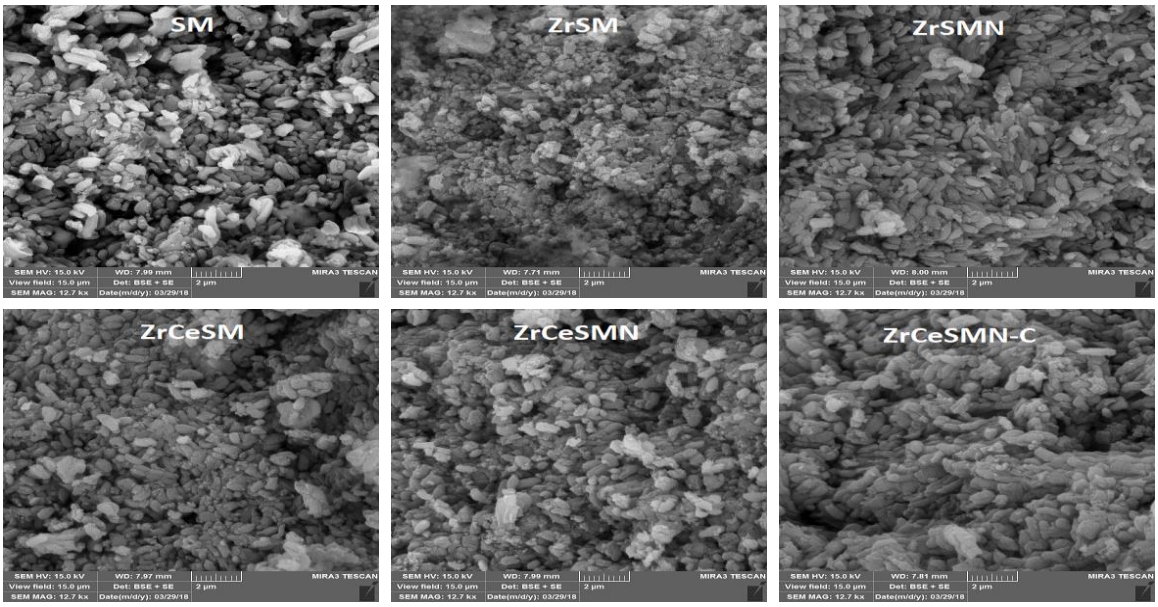

Figure 4. 5: FESEM images of the Zr and ZrCe-modified SBA-15 supported NiMo catalysts.

The binding states and energies of Mo phases in the sulfided catalysts was determined using XPS. The information was utilized to have a fair understanding of the degree of sulfidation of the Mo in the catalysts [113]. The results of the Mo XPS analysis obtained after peaks deconvolution is shown in **Fig. 4.6** and **Table 4.5**. Three Mo phases were noticed at approximately 229.5, 231.8 and 235.6 eV binding energies, and these peaks were assigned to the Mo^{4+} ($3d_{5/2}$), Mo^{6+}($3d_{5/2}$) and Mo^{6+}($3d_{3/2}$) phases respectively. The Mo^{4+} ($3d_{5/2}$) phase is characteristic of MoS_2 whereas Mo^{6+}($3d_{5/2}$) and Mo^{6+}($3d_{3/2}$) defines the MoO_3 species. A low intensity peak at approximately 226 eV, similar to the 2S line due to sulfur, was also observed and this was deducted from the Mo percent composition [132]. From the **Fig. 4.6**, it was observed that SM catalyst has small atomic percent of the MoS_2 phase and ZrCeSMN-C catalyst does not even show the MoS_2 peak. This shows that the sulfidation level in both catalysts is considerably low. However, the remaining catalysts show reasonable degree of sulfidation which increases according to the trend ZrSM < ZrCeSM < ZrSMN < ZrCeSMN. Therefore, it can be deduced that the incorporation of biheteroatom increases the ease of MoO_3 sulfidation, although calcination at 550 ^oC further retards the sulfidation process.

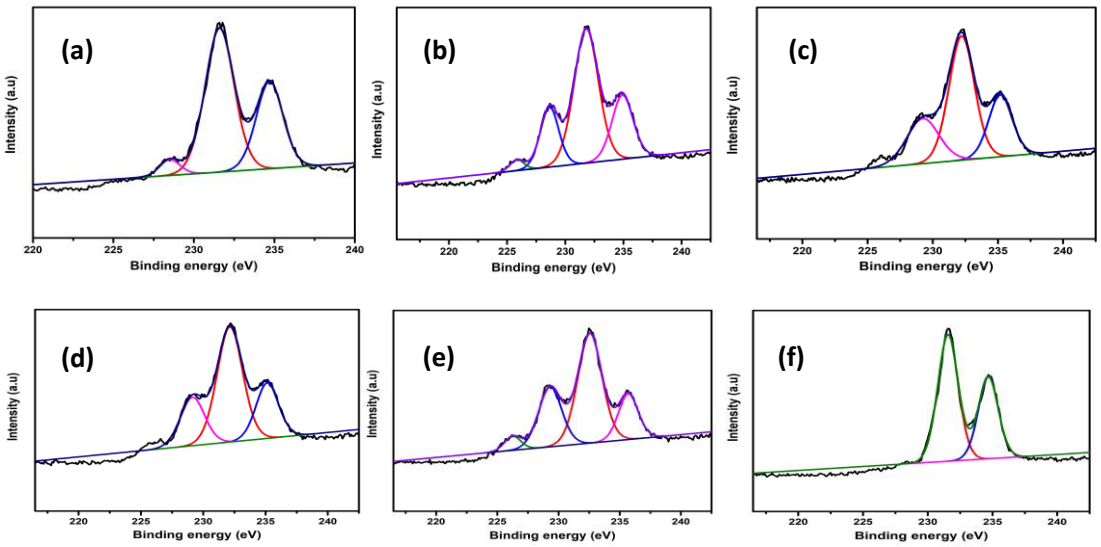

Figure 4. 6: XPS spectra of the Zr and ZrCe-modified SBA-15 supported NiMo catalysts showing the various Mo phases: (a)SM; (b) ZrSM; (c)ZrSMN; (d) ZrCeSM; (e) ZrCeSMN; (f) ZrCeSMN-C.

Table 4. 5: Different Mo phases obtained from the XPS spectra.

Catalysts	**Percent molybdenum in various oxidation states**		
	Mo^{4+} ($3d_{5/2}$)	**Mo^{6+} ($3d_{5/2}$)**	**Mo^{6+} ($3d_{3/2}$)**
Binding energy	**229.5 eV**	**231.8 eV**	**235.6 eV**
SM	0.03	64.07	35.92
ZrSM	19.33	56.95	23.72
ZrSMN	23.96	51.97	24.07
ZrCeSM	21.94	54.83	23.23
ZrCeSMN	28.04	53.81	18.14
ZrCeSMN-C	-	61.25	38.75

4.3.2 Catalysts Activity Test

The developed catalysts were evaluated for HDS using diesel fuel spiked with 1000 ppm DBT and the performance result is presented in **Table 4.6**. After 1 h of reaction, it was estimated that 30.26% of DBT has been removed from the diesel using the SM catalyst, and this percent got increased by approximately 15% and 29% when ZrCeSM and ZrCeSMN were used for the HDS reaction respectively. The percent sulfur removal in the subsequent hours follows similar trend, and by the 5^{th} hour, almost 96% of sulfur has been removed by ZrCeSMN. However, when the ZrCeSMN-C was used for the HDS, a significant drop in conversion was noted (**Fig. 4.7**). The observed trend in HDS performance is correlated to the physicochemical properties of the catalysts such as surface acidity, metal support interaction and active phase dispersion. The ZrCeSMN catalyst that shows the highest HDS performance happens to have the largest surface area as discussed in the textural properties study of the catalysts, and this textural property usually results in more active phase loading and dispersion which are likely to result in better HDS experience. In addition, the py-FTIR and NH_3-TPD results discussed above enumerated that the incorporation of ZrO_x and CeO_y increase the strong acidic sites of the catalyst support and by implication increased the metal-support interaction and active phase dispersion on the SBA-15 support as was further corroborated by the H_2-TPR results. On the other hand, the low HDS performance of ZrCeSMN-C is related to the relatively low surface area of the catalysts and active phase dispersion.

Table 4. 6: Catalyst performance results: Percent DBT removal from diesel. (Process conditions: 350 ^{o}C; 5 MPa; DBT=1000 ppm; reaction time = 5 h).

Catalysts	**Percent DBT removal (%)**				
	1h	**2h**	**3h**	**4h**	**5h**
SM	30.26	56.1	57.6	61.67	66.8
ZrSM	28.28	49.45	56.78	65.07	67.14
ZrSMN	51.06	71.92	72.24	79.08	84.55
ZrCeSM	45.07	61.6	78.48	76.87	80
ZrCeSMN	59.3	68.58	92.47	92.67	95.65
ZrCeSMN-C	10.87	37.49	40.45	57.15	72.92

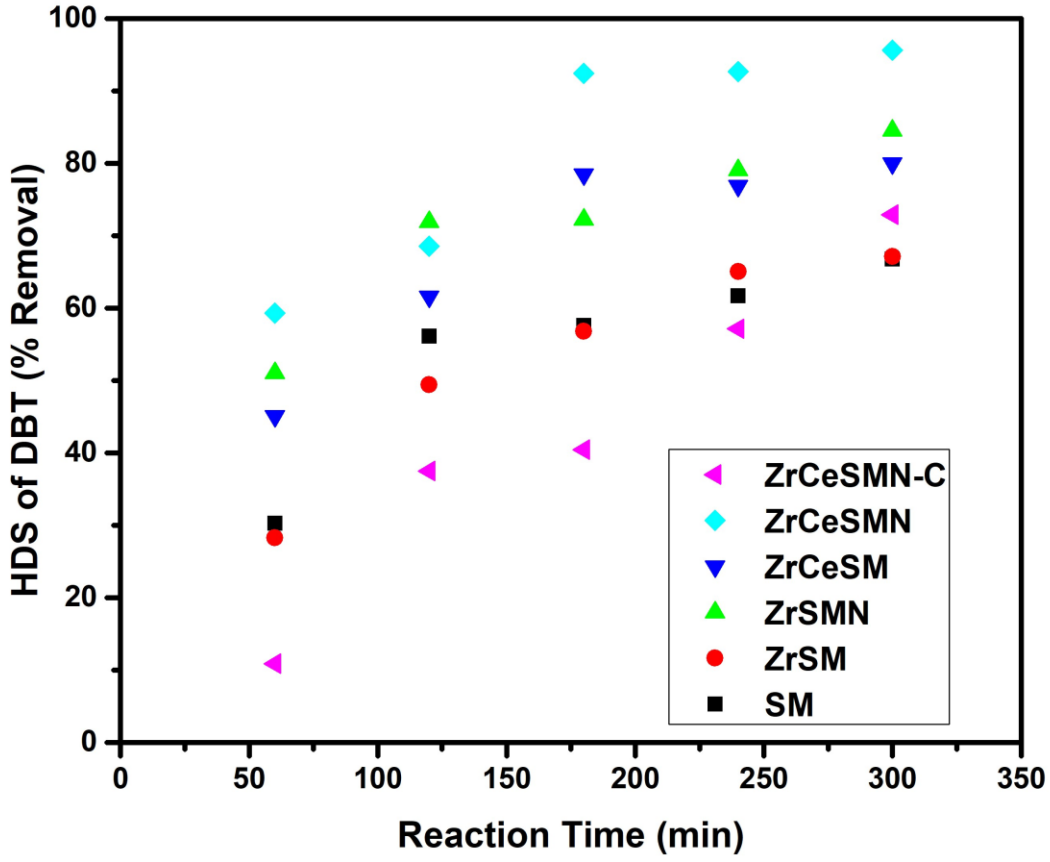

Figure 4. 7: (a) Plot of HDS performance of Zr and ZrCe-modified SBA-15 supported NiMo catalysts.

4.4 Conclusion

The synergetic effect of ZrO_x and CeO_y on the active site formation and dispersion for SBA-15 supported NiMo catalysts has presented interesting performance in the HDS of DBT in diesel fuel. The electronic and structural interactions between the ZrO_x and CeO_y in the catalyst significantly improved the catalyst textural properties such as surface area and pore volume. The py-FTIR and NH_3-TPD results demonstrated that the catalysts acidic strength was also increased because of combined effect between ZrO_x and CeO_y. The H_2-TPR results shows an increased metal-support interaction that is sufficient enough to enhance the active phase dispersion on the support. The XPS analysis further confirmed the formation of increased amount of MoS_2 active phases in the ZrO_x-CeO_y modified SBA-15 supported NiMo catalysts which further enumerate the synergetic effect of the ZrO_x-CeO_y combination in the ZrCeSMN catalyst. As a result, the ZrCeSMN catalyst demonstrated higher HDS activity of DBT in diesel than the rest of the catalysts in the series.

CHAPTER 5

A GREENER AND EFFICIENT APPROACH TO THE SULFIDATION OF SUPPORTED METAL OXIDE CATALYSTS FOR HYDRODESULFURIZATION APPLICATIONS

ABSTRACT

The conventional approach for the sulfidation of supported metal oxide catalysts involves the use of hydrogen sulfide or carbon disulfide at high temperatures. Both chemicals are highly toxic and depending on the degree of exposure, can lead to death. The increasing demand for a cleaner and sustainable environment has made it imperative to develop a greener approach for synthesis of hydrodesulfurization catalysts. In this work, (3-Mercaptopropyl)trimethoxysilane (MPMS) silica precursor that doubles as a sulfur precursor was employed to eliminate the hazardous sulfidation step for metal oxide catalysts. The novel approach, carried out by hydrothermal synthesis at 90 ^{o}C for 24 h, involves stirring together a mixture of MPMS, Pluronic P123 surfactant, Co and Mo precursors in an acidic solution for 24 h. The dried powder was heated at 400 ^{o}C for 3 h in a flow of air, argon and hydrogen to form three different silica supported CoMoS catalysts (air-treated, Ar-treated and H_2-treated). Fourier Transform infrared spectroscopy and X-ray photoelectron were used to investigate the formation of MoS_2 phase in the catalysts. The MoS_2 phase formation is in the order H_2-treated > Ar-treated > air-treated catalysts. X-ray diffraction studies showed that all the catalysts are well dispersed on the silica support. The hydrodesulfurization performance test demonstrated that H_2-treated catalyst offers the best activity, and this was correlated to its available MoS_2 phase and the BET surface area. The use of this approach has successfully eliminated the conventional highly toxic sulfidation step in the synthesis of supported metal catalysts for hydrodesulfurization.

5.1 Introduction

Hydrodesulfurization (HDS) of high sulfur fuel requires a robust catalyst. Generally, efficient HDS catalyst is conceived from the catalyst's design strategy. Choice of active phases such as CoMo(W) and NiMo(W), and active phase support (in the case of supported catalysts) such as alumina, silica and zeolites constitute the integral part of the catalysts design. But more importantly, the choice of synthetic method adopted for production of the catalyst will have a major impact in dictating the type of catalyst produced, both in terms of catalyst efficiency and safety of the synthesis approach [133,134].

Over the years, the synthetic strategies used had main objectives of increasing metal dispersion on supported catalysts [135–137]. Different approaches to enhance formation of the MoS_2 phase and inhibiting the sulfidation of the metal promoters such as Co and Ni, have been demonstrated in the literature by usage of chelating agents [138–141]. Recently, a single-pot strategy, that involves mixing together both the support precursors and active metals precursors in a single hydrothermal synthesis strategy, was reported to enhance both metal dispersion and formation of MoS_2 active phase by our group [51].

Typically, all these synthetic approaches gave rise to catalysts in their oxides form, and therefore, an activation step that involves the oxides reduction and further sulfidation is required. The sulfidation step involves passing hydrogen sulfide gas and in some cases carbon disulfide solution at high temperature through a muffle furnace containing the reduced metal catalysts. These chemicals have been classified as highly toxic and even low level exposure (2 -5 ppm) can cause nausea, respiratory difficulty and loss of appetite [142,143]. The risk of working in an environment of low sulfide exposure even below the OSHA and NIOSH standards has been linked with chronic long-term health effects such

as brain damage, and regrettably, as of now there is no suitable specific therapy for sulfide poisoning. Therefore, the need for adopting a novel and safe approach for metal oxide catalyst sulfidation that would eliminate the direct use of highly toxic hydrogen sulfide or carbon disulfide is imperative [144].

The use of thiosalt both as active metals and sulfur precursors have been demonstrated as easy and reproducible approach to address the challenge of the reduction and sulfidation of the metal oxides catalysts [145,146]. The approach involves thermal decomposition of the thiosalt to give the desired unsupported active catalysts and has been explored in the synthesis of stoichiometric amount of both bi- and tri-metallic sulfides [147,148]. Series of tungsten disulfide (WS_2) as HDS catalysts have been prepared by thermal decomposition of ammonium tetrathiotungstates and tetraalkylammonium thiotungstate under the flow of N_2 and H_2S/H_2 [149]. Romero et al. synthesis MoS_2 using different alkyldiammonium thiomolybdate (alkyl = ethyl, 1,4-butyl, 1,6-hexyl and 1,8-octyl), and observed that the formed MoS_2 catalysts contains carbon intercalated within their pores which is due to the decomposition of the alkyl group in the precursors [150]. Ammonium and alkyltrimethylammonium-thiomolybdate-thiotungstate-cobaltate (II) were used as precursors to form various CoMoW-S catalysts via thermal decomposition which were tested in the HDS of dibenzothiophene (DBT) [151].

This nice approach is particularly successful in the synthesis of low surface area unsupported bulk HDS catalysts. Furthermore, the metals thiosalt precursors are mostly synthesized prior to the *in situ*/*ex situ* decomposition which makes the procedure somewhat challenging.

The present study therefore explores the use of (3-Mercaptopropyl)trimethoxysilane (MPMS) both as a silica support and as a sulfur precursor for the synthesis of supported metals catalysts with high surface area. Indeed, the use of support in catalysts synthesis and development improved catalysts activity due to active phase dispersion and minimize the use of bulk metals. The mixture of MPMS, Pluronic P123 surfactant, Co and Mo precursors were subjected to hydrothermal synthesis in an acidic solution for 24 h. This novel one-step approach has addressed the challenge of catalyst sulfidation using toxic chemicals which is an important step in the preparation of supported catalysts and has also enhanced metal dispersion on the silica support via metal-sulfur interactions. The synthesized sulfur-rich silica supported CoMo catalyst was exposed to three different calcination treatments at 400 ^{o}C for 3 h under the flow of air; Ar and H_2. Subsequently, the treated catalysts were characterized by BET, FTIR, XRD, SEM and XPS to understand their physico-chemical behavior.

5.2 Experimental Section

5.2.1 Synthesis of Sulfur-Rich Silica Supported CoMo

The sulfur-rich silica supported CoMo was prepared by dissolving 1.25 g of pluronic P123 in 30 ml of 2M HCl solution followed by addition of 10 ml deionized water and the mixture was stirred for 30 min at 40 ^{o}C. Then 2.45 g of MPMS was added dropwise to the continuous stirred mixture and after 1 h of stirring, a solution of Mo and Co (10 wt.% and 3 wt.% respectively) was added to the mixture and the stirring continued for 20 h before transferring the mixture into a Teflon-lined autoclave for hydrothermal synthesis at 90 ^{o}C for 24 h. The greenish solid was centrifuged and dried at 100 ^{o}C overnight before subjecting it to the calcination treatment. The elemental composition of the dried greenish sulfur-rich

silica supported CoMo powder abbreviated as HS_SiO_2_CM was determined by X-ray fluorescence (XRF) spectrometer and is presented as **Table 5.1**.

Table 5. 1: Representative elements present in sulfur-rich silica supported CoMo catalyst before activation.

Spectrum	**Si**	**S**	**Co**	**Mo**
HS_SiO_2_CM 1	35.57	56.10	1.25	7.08
HS_SiO_2_CM 2	32.24	57.94	1.09	8.74
HS_SiO_2_CM 3	33.19	57.42	0.99	8.40
HS_SiO_2_CM 4	31.79	60.70	1.27	6.24
HS_SiO_2_CM 5	35.45	56.07	1.05	7.43
Mean value	33.65	57.65	1.13	7.58
Std. Abw.:	1.59	1.69	0.11	0.90
Std. Abw. rel. [%]:	4.71	2.94	9.88	11.92

5.2.2 Activation of the Sulfur-Rich Silica Supported CoMo

Three different activation approaches, air, argon and hydrogen were employed to obtain the CoMoS active species. Simply, the samples were heated in a tubular furnace at 400 ^{o}C for 3 h under the flow of air, argon and hydrogen respectively. Under these conditions, the sulfur is expected to react with the metals to form CoMoS active phase on the silica support. The formed catalysts are named air-treated, Ar-treated and H_2-treated respectively, and the schematic representation of the synthesis procedure is presented as **Fig. 5.1**.

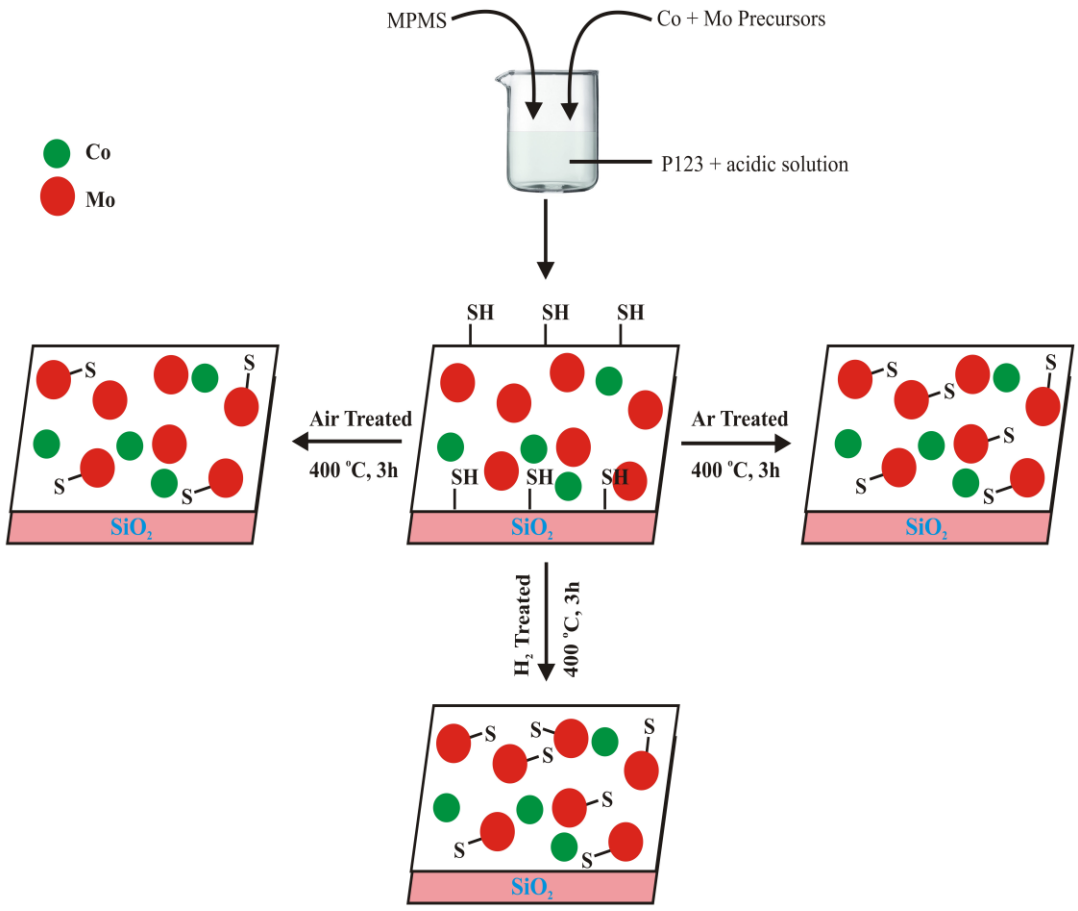

Figure 5. 1: Synthesis approach of silica supported CoMoS catalysts. MPMS is (3-Mercaptopropyl)trimethoxysilane

5.2.3 Characterization of the Activated CoMoS Catalysts

The catalysts textural properties were evaluated on a Micromeretics Tristar II by N_2 adsorption-desorption isotherm at 77k. At first, the catalysts (approximately 0.1 g each) were degassed under flowing argon at 523k for 2.5 h, and the BET method was used to calculate the surface area, whereas absorption branch of BJH method was applied to calculate the pore size and pore volume of the catalysts.

The catalysts FTIR spectra were recorded on a Nicolet 6700 FTIR spectrometer within a wavelength range of 400 – 4000 cm^{-1}, by preparing a 1:100 mixed pellet of catalysts and KBr respectively and inserting the pellet into the FTIR cell.

Catalyst crystallinity and the distribution of CoMo on the silica support were determined by scanning the catalysts' X-ray diffraction pattern between 20 ^{o} to 80 ^{o} 2θ at 40 kv and 40 mA using Rigaku Ultima IV X-ray diffractometer.

Surface morphologies of the catalysts were imaged using JEOL JSM-6610LV scanning electron microscope, and element mapping with corresponding EDX spectrum were recorded using the energy dispersive X-ray spectrometer.

The degree of Mo sulfidation of the catalysts due to the different activation conditions were determined by X-ray photoelectron spectroscopy (XPS) using PHI 5000 Versa Probe II, ULVAC-PHI Inc. spectroscope.

5.2.4 Catalysts Activity Test

All the three activated catalysts were pelletized, crushed and sieved within 300 – 500 microns prior to the activity test. The activity test was carried out in a Parr 4590 Micro

Bench Top Reactor operated at a pressure of 5MPa of H_2 and 100 rpm stirring rate. Approximately 15 mg of the activated catalyst was added to 15 ml of model fuel containing 1000 ppm DBT in dodecane. The reaction was performed for 4 h after the reaction conditions have been stabilized, and product sampling were done at hour interval. GC-SCD was used to monitor decrease in the DBT in model fuel and catalysts activity was calculated in terms percent conversion versus reaction time. The identity of products and the product distribution studies were performed using the GC-MS.

5.3 Results and Discussion

5.3.1 Characterization Results

The surface area, pore volume and pore sizes of the activated catalysts are presented in **Table 5.1**. Typically, large BET surface area and pore volume are indication of better catalysts performance since the reactant molecules are likely to interact more effectively with the active phase of the catalysts when the surface area is large. From the textural properties results in **Table 5.2**, it was observed that air-treated catalyst has the lowest surface area (30 m^2/g) whereas the Ar-treated catalyst has the highest surface area of 298 m^2/g. H_2-treated catalyst has relatively lower BET surface area than Ar-treated although it presents a slightly higher microporous surface area.

Table 5. 2: Textural properties of the activated catalysts

Catalysts	**BET surface area (m^2/g)**	**Microporous surface area (m^2/g)**	**External surface area (m^2/g)**	**Microporous pore volume (cm^3/g)**	**Total pore volume (cm^3/g)**	**Average pore size (nm)**
Air-treated	30	28	31	0.002	0.083	9.6
Ar-treated	298	83	193	0.058	0.187	5.8
H_2-treated	154	92	63	0.054	0.102	7.5

This implies that the activation condition significantly affects the surface area of the sulfur-rich silica supported CoMo catalysts. Similar pattern was observed for both microporous pore volume and total pore volume of the catalysts. However, it was observed that the average pore size of the catalysts follows an inverse relation with the catalysts BET surface area with air-treated and Ar-treated catalysts presenting pore size of 9.6 nm and 5.8 nm respectively. The observed behavior can be connected to the possible combustion of the Pluronic P123 organic template during the activation process. Generally, it is expected that Air-treated catalyst would have the least carbon deposition due to the oxidation of carbon by air, which open the mesoporous cavities that were hitherto filled up with surfactant, therefore it can be inferred that the amount of carbon deposit on the catalysts influence their pore volume and surface area [152]. The N_2 adsorption-desorption isotherm and pore volume versus pore width plots presented in **Fig. 5.2** depict the level of porosity of the catalysts, and type IV hysteresis loop is observed which confirms the presence of both micropores and mesopores due to the complexity of the activated catalysts.

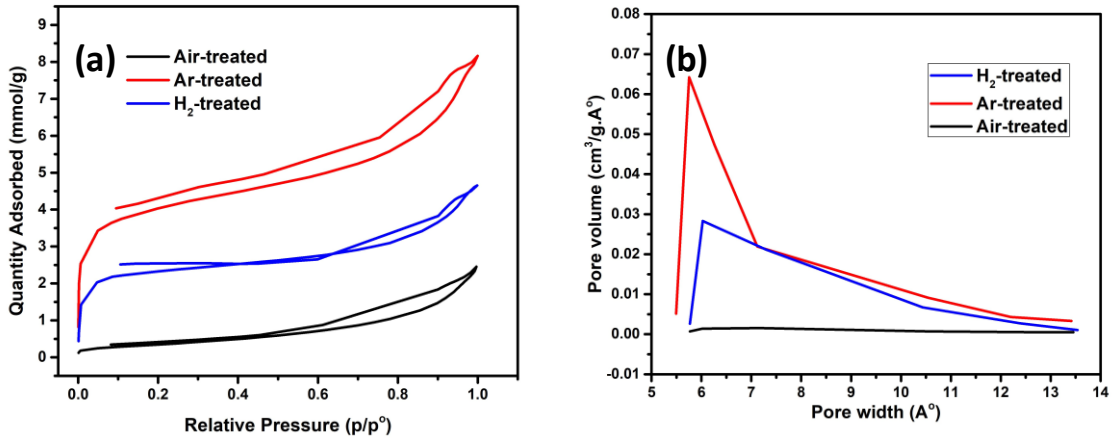

Figure 5. 2: (a) N_2 adsorption-desorption isotherm and (b) pore volume-size distribution for the activated catalysts.

The FTIR spectra of the catalysts (air-, Ar- and H_2-treated) are presented in **Fig. 5.3a**. All the catalysts show peaks characteristics of silica support. The O-H stretching adsorption band (due to silanol or water adsorption) was observed at 3500 cm^{-1} while Si-O-Si stretching vibration and Si-OH were noted at 1050 cm^{-1} and 750 cm^{-1} respectively. Interestingly, peak of the thiol group attached to the silica was not observed in all the activated catalysts, therefore, it can be inferred that the thiol has been decomposed due to the activation treatment and was converted to possibly the metal sulfides, hydrogen sulfide and sulfur dioxide depending on the activation condition. The Mo-S vibration peak was observed in all the catalysts at 490-500 cm^{-1} [153,154], thus confirming the formation of the MoS_2 active phase in all the catalysts. Careful observation of the peak intensity revealed that H_2-treated catalyst has relatively larger amount of MoS_2, thus is expected to have more active phases than the Ar- and Air-treated catalysts. The peaks observed at 2900 cm^{-1} and 2300 cm^{-1} were assigned to the $-CH_2$ and $-C\equiv C-$ stretching vibration due to the decomposition of Pluronic P123 during the catalyst's activation. Their peak intensities further support the claim that the Air-treated catalyst has the least carbon deposit.

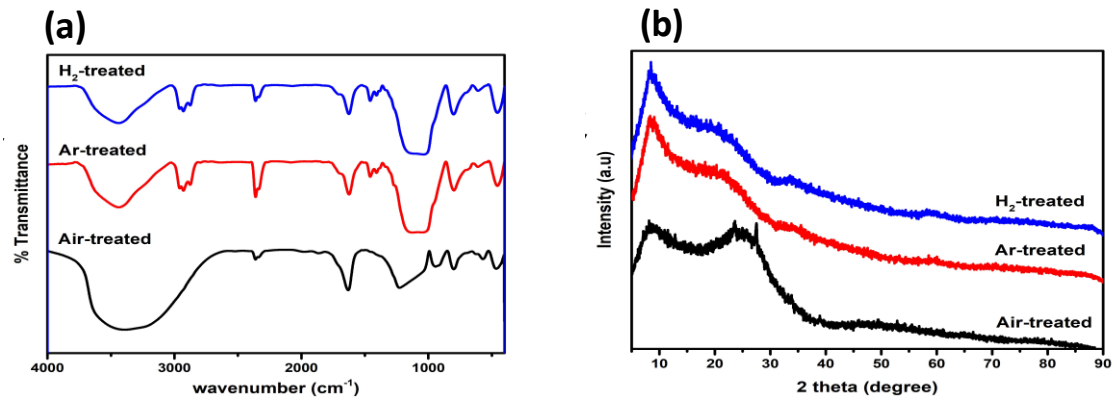

Figure 5. 3: (a) FTIR spectra and (b) XRD pattern of the activated catalysts.

The catalysts crystallinity and fair understanding of the CoMo dispersion on silica support was elucidated from the X-ray diffraction patterns shown in **Fig. 5.3b**. All the observed patterns show broad band characteristic of the amorphous nature of silica. This imply that the metals have relatively good dispersion on the silica support. The interaction between the metal species and the sulfur of the thiol group in the silica support is likely responsible for the good dispersion of the metal catalysts. Diligent observation of the spectra can also reveal weak peaks of the metal phases present in the activated catalysts. Firstly, the Air-treated catalyst shows peculiar diffraction peaks at 24 and 27.5 ^{o} 2θ, which are well resolved peaks of MoO_3 (JC-PDF2-No. 05–0508) [155]. These diffractions peaks were not noticed in the Ar- and H_2-treated catalysts, instead peaks characteristic of MoS_2 were observed at 35 and 60 ^{o} 2θ (JC-PDS No. 37-1492) [153]. Based on the observed results, it can be concluded that all the catalysts have relatively good dispersion of the metals due to their poor crystallinity [115], and the degree of Mo sulfidation is relatively low in the Air-treated catalysts due to the observed MoO_3 phases.

The SEM images of all the activated catalysts is presented in **Fig. 5.4**. The images showed that the catalysts composed of particles of irregular sizes and the particle density is largest in Ar- and H_2-treated catalysts and lowest in air-treated catalyst. The EDX elemental analysis of the catalysts presented in **Table 5.3** highlighted the reason for the large particle density of Ar- and H_2-treated catalysts to be due to the carbon deposit.

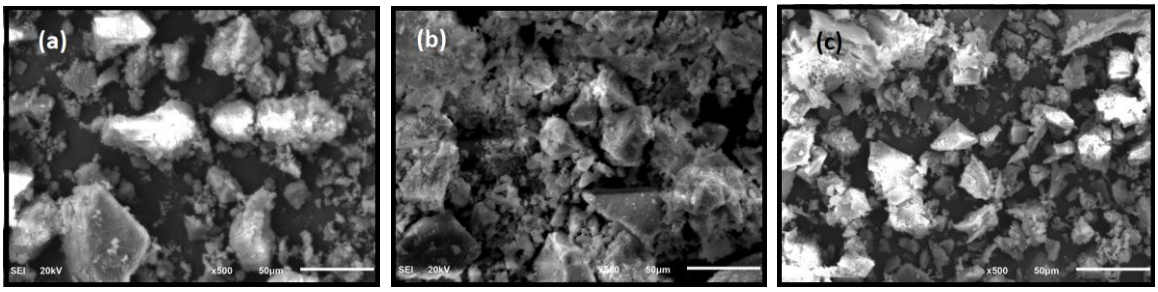

Figure 5. 4: SEM images of the activated catalysts: (a) Air-treated; (b) Ar-treated and (c) H_2-treated.

The percent carbon of 41.39, 55.90 and 57.41 were recorded for the air-, Ar- and H_2-treated catalysts respectively. Furthermore, the percent sulfur of 0.9, 1.33 and 1.89 for Air-, Ar- and H_2-treated catalysts were obtained from the EDX analysis, which means the MoO_3 were more sulfided in the H_2-treated catalyst than in Ar-treated catalyst, and Air-treated catalyst presents the least Mo sulfidation. This supports the XRD and FTIR results. The mapping of the element was performed on the catalysts to check the distribution of all the elemental components. **Fig. 5.5** show that all the elemental components are evenly distributed in the activated catalysts. Therefore, this approach of synthesizing supported CoMoS catalysts from sulfur-rich support provides excellent distribution of the active species on the support.

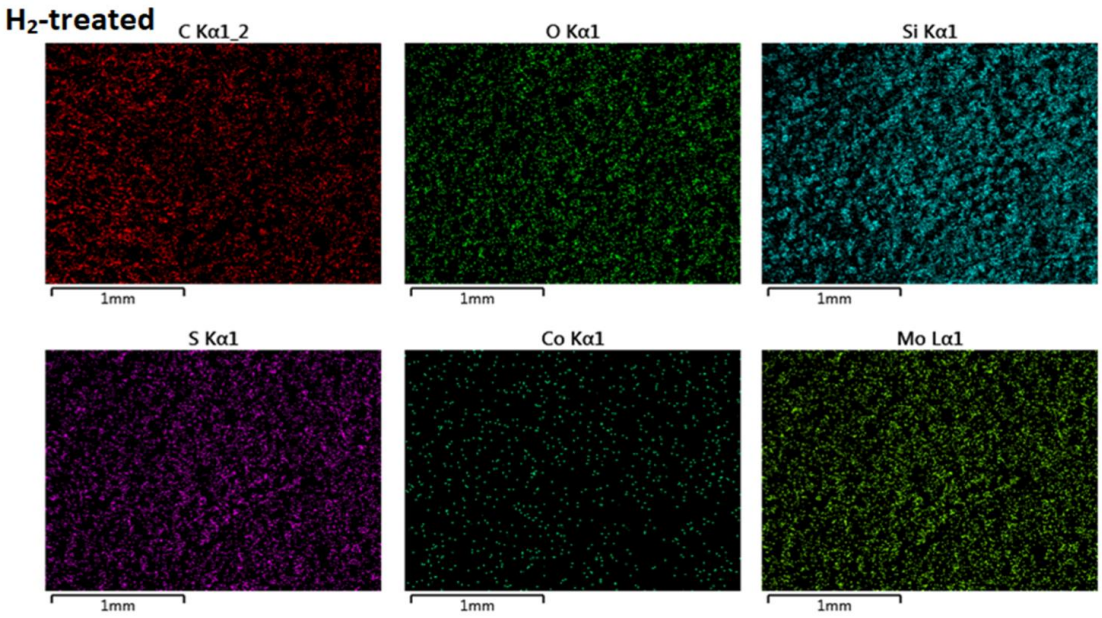

Figure 5. 5: Mapping of the elemental analysis of H_2-treated catalyst showing the distribution of all the elemental component.

Table 5. 3: Percent elemental composition of the activated catalysts obtained from EDX analysis

Catalysts	**C**	**O**	**Si**	**S**	**Co**	**Mo**
Air-treated	41.4	37.9	14.8	0.90	0.07	4.92
Ar-treated	55.9	25.7	13.5	1.33	0.05	3.51
H_2-treated	57.4	23.2	14.1	1.89	0.03	3.39

Table 5. 4: Percent elemental composition of the activated catalysts obtained from XPS analysis

Catalysts	**C1s (284 eV)**	**Mo^{4+} ($3d_{5/2}$) (228eV)**	**Mo^{6+}($3d_{5/2}$) (232eV)**	**Mo^{6+}($3d_{3/2}$) (235eV)**
Air-treated	18.8	0.14	0.20	0.14
Ar-treated	35.5	0.20	0.20	0.13
H_2-treated	44.1	0.39	0.10	-

The XPS analysis of the activated catalysts were performed to understand the Mo phases in the catalysts and the level of sulfidation achieved through the different activation approach. **Fig. 5.6a** and **Fig. 5.6b** present the deconvoluted XPS of Mo and sulfur respectively in the activated catalysts. The XPS peaks of Mo were identified at 228 eV, 233 eV and 236 eV which correspond to the Mo^{4+} ($3d_{5/2}$), Mo^{6+}($3d_{5/2}$) and Mo^{6+}($3d_{3/2}$) states respectively. The XPS peak of sulfur was observed at 163 eV and correspond to the S^{2-} ($2P_{3/2}$) state of sulfur. The presence of both Mo^{4+} and S^{2-} XPS peaks confirmed the formation of the MoS_2 active phase in the catalysts, and higher percent of these Mo^{4+} and S^{2-} states in the catalysts will imply more active phases. **Table 5.4** contains the elemental composition of the activated catalysts in their various oxidation states obtained from the XPS result. Air-treated catalyst has the least percent of Mo^{4+} ($3d_{5/2}$) and S^{2-} ($2P_{3/2}$) whereas H_2-treated has the largest percent of Mo^{4+} ($3d_{5/2}$) and S^{2-} ($2P_{3/2}$). This further confirms the SEM, XRD and FTIR results that high percent of the active phase are obtained in the H_2-treated catalyst. Based on the characterization results discussed above, the mechanism of activation is proposed below.

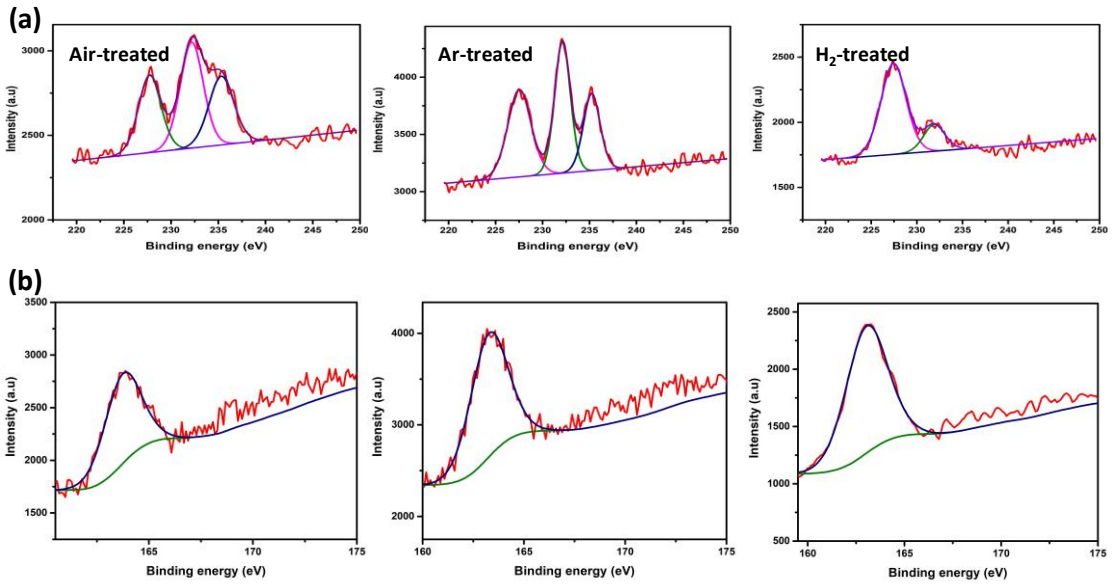

Figure 5. 6: XPS spectra of the activated catalysts showing the (a) Mo phases and (b) sulfide state in the activated catalysts.

5.3.2 Proposed Mechanism of the HS_SiO$_2$_CM Activation

The HS_SiO$_2$_CM catalyst was activated at 400 ^{o}C for 3 h under the flow of air, Ar and H_2. At this activation temperature, the thiol bond in the catalyst is likely to be dissociated and the formation of H_2S is probable. In the flow of air, formation of SO_2 is most probable due to oxidation of the thiol as shown in equation (6.1), and this, in addition to the oxide nature of the catalyst, hinders the sulfidation process. In the flow of Argon, the decomposition of the thiol is expected to yield H_2S and S_2 (equation (6.2)) which is likely to improve the sulfidation of the catalyst oxide though not as efficiently as in the case of H_2, where the metal oxides first get reduced and subsequently sulfided as depicted in equation (6.3). The decomposition of P123 surfactant during the activation process is expected to form carbon deposit and oxides of carbon. Typically, Ar- and H_2-treated catalysts are likely to form only the carbon deposit while the air-treated will form the CO and CO_2 in addition to the carbon deposit.

$$\mathbf{HS\_SiO_2\_CM} \overset{\boldsymbol{air}}{\longrightarrow} \boldsymbol{SiO_2\_CoMo\ (oxides) + H_2S + SO_2\ \rightarrow\ SiO_2\_CoMo\ (oxides) +} \boldsymbol{SiO_2\_CoMoS} \ldots\ldots\ldots\ldots\ldots\ldots\ldots\ldots\ldots (6.1)$$

$$\mathbf{HS\_SiO_2\_CM} \overset{\boldsymbol{Ar}}{\rightarrow} \boldsymbol{SiO_2\_CoMo\ (oxides) + H_2S + S_2 \rightarrow\ SiO_2\_CoMo\ (oxides) +} \boldsymbol{SiO_2\_CoMoS} \ldots\ldots\ldots\ldots\ldots\ldots\ldots\ldots (6.2)$$

$$\mathbf{HS\_SiO_2\_CM} \overset{\boldsymbol{H_2}}{\rightarrow} \boldsymbol{SiO_2\_CoMo\ (reduced) + H_2S \rightarrow\ SiO_2\_CoMoS} \ldots\ldots\ldots\ldots (6.3)$$

5.3.3 Catalysts Activity Test

The activity results of the silica supported CoMoS catalysts developed through activation of $HS\_SiO_2\_CM$ via three different treatments is presented in **Table 5.5**. As expected, the H_2-treated catalyst which has more of the active phases required for the HDS reaction showed the highest percent conversion of DBT while air-treated catalyst present the lowest percent conversion. The percent conversion of DBT for Ar-treated catalyst is slightly lower than the observed conversion for H_2-treated catalyst (**Fig. 5.7**). The disparity in DBT removal by the catalysts is attributed to the activation condition, where activation under the flow of H_2 resulted in largest amount of Mo sulfidation. Furthermore, the catalysts BET surface area and pore volume significantly affect the catalysts activity. Ar-treated catalyst with the largest surface area performed very well close to the H_2-treated catalyst even though the former has relatively lower Mo sulfidation, which implies that its large surface area and total pore volume have enhanced the HDS activity. The carbon deposit formed due to decomposition of organic surfactant may also affect the HDS activity [149]. According to previous findings, large carbon deposit is likely to impact negatively on the HDS activity of the catalysts due to the blocking of active sites [152,156]. Indeed, the air-treated catalyst has lower percent of carbon deposit than the Ar- and H_2-treated catalysts, however, both its microporous and total pore volume are lesser than those of Ar- and H_2-treated catalysts. This may imply that the role of the carbon deposit on the catalysts' textural properties and HDS activity is mostly dependent on the synthesis approach through which the carbon is introduced into the structure of the active metals phases. Successful incorporation of carbon at the edges of MoS_2 slabs will surely enhance its HDS activity as reported by Kelty et al. [157].

Table 5. 5: Activity and product distribution in the HDS of DBT for the activated catalysts after 4 h of reaction.

Catalysts	**DBT removal (%)**	**Product distribution (%)**		k_{HDS} x 10^3 **(min^{-1})**	k_{DDS} x 10^3 **(min^{-1})**	k_{HYD} x 10^3 **(min^{-1})**	k_{DDS}/k_{HYD}
		CHB	**BP**				
Air-treated	58.3	-	100	3.65	3.65	0.00	-
Ar-treated	72.2	10.2	89.8	5.33	4.79	0.54	8.87
H_2-treated	75.5	10.1	89.9	5.85	5.26	0.59	8.92

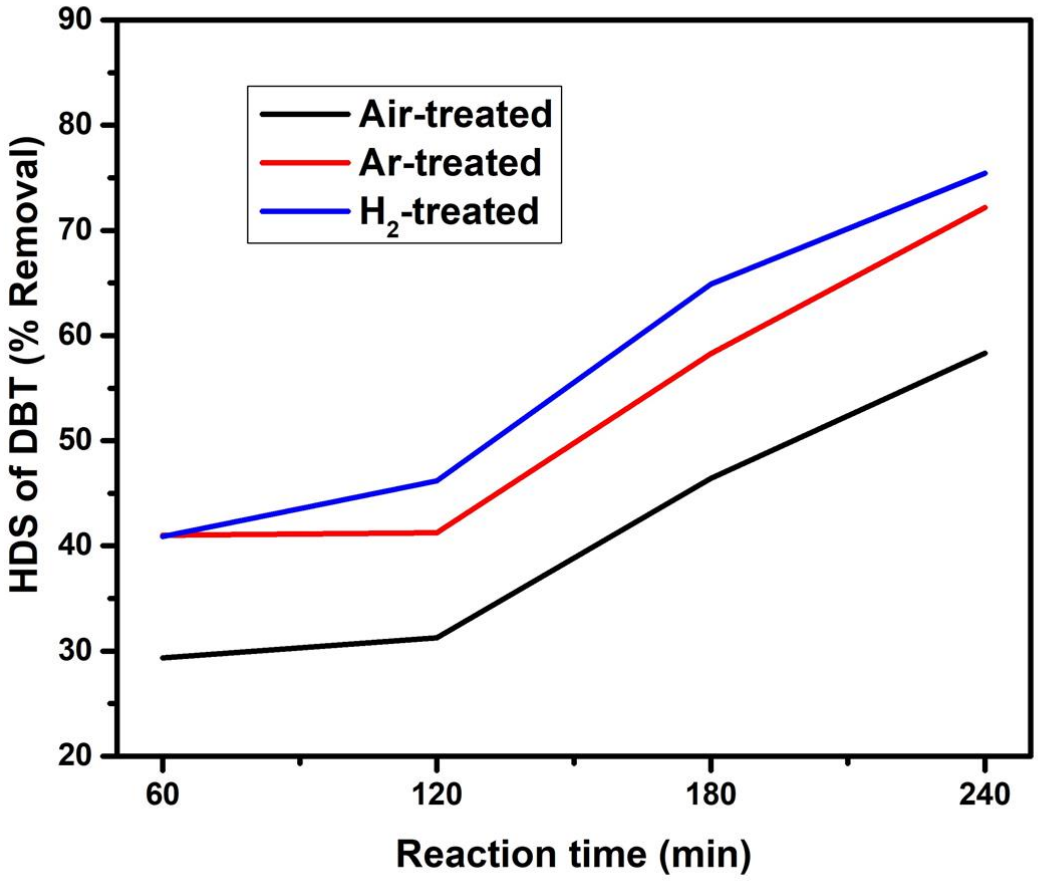

Figure 5. 7: Catalysts activity plot for HDS of DBT at 350 ^{o}C and 5MPa.

Product distribution studies also shows an outstanding difference between the catalysts' activation methods. Previous studies have shown that the HDS of DBT typically occurs through two major pathways: direct desulfurization to form biphenyl (BP) and hydrogenation to form cyclohexyl benzothiophene which dissociates fast via C-S cleavage to form cyclohexyl benzene (CHB) [13]. Product distribution results presented in **Table 5.5** shows that BP is the only product of the HDS reaction for air-treated catalyst, thus the reaction occur only via the DDS pathway. The HDS reaction using Ar- and H_2-treated catalysts however, occurs via both the DDS and HYD pathways forming BP (*ca.* 90%) and CHB (*ca.* 10%) respectively. The hydrogenation behavior of Ar- and H_2-treated catalysts suggest their potential applicability in the HDS of more refractory sulfur compounds like dimethyldibenzothiophene that are known to be desulfurized especially through the HYD pathway [116]. The disparity in the product selectivity observed among the catalysts further demonstrates the effect of activation approach to the $HS\_SiO_2\_CM$ catalyst.

The kinetic parameters were established following the assumption that the HDS reaction occurs via the parallel pathway, and Pseudo-first kinetics was used to calculate the rate constants after 4 h reaction time. The rate constants (min^{-1}) of the HDS ($\mathbf{k}_{HDS}$); DDS ($\mathbf{k}_{DDS}$); and HYD ($\mathbf{k}_{HYD}$) were presented in **Table 5.5**. The k_{HDS} of the activated catalysts was noted to increase in the order air-treated > Ar-treated > H_2-treated, however, the ratio of the k_{DDS}/k_{HYD} was observed to be nearly the same for Ar- and H_2-treated catalysts. The k_{DDS}/k_{HYD} for air-treated is undefined further demonstrating that the reaction occurred only via the DDS pathway. **Table 5.6** presents a fair comparison between various reported k_{HDS} and the observed k_{HDS} of H_2-treated catalyst. Interestingly, the observed k_{HDS} compares very well with reported values, thus buttressing the success of this novel approach.

Therefore, by adopting this novel approach of catalysts synthesis, similar (and in some cases better) performance can be achieved and most importantly, the use of toxic chemicals has been completely avoided.

Table 5. 6: Comparison of HDS activity of various catalysts based on their rate constants.

Catalysts	**k_{HDS} x 10^3 (min^{-1})**	**Reference**
TSMN-SP-550[a]	6.50	[51]
WS-1[b]	0.85	[149]
CoMoWS-C14[c]	10.6	[151]
H_2-treated	5.85	This work

a) Single pot synthesis of Ti-SBA-15 NiMo oxides
b) WS_2 formed from ex situ decomposition of ammonium thiotungstate in N_2
c) CoMoWS obtained by in situ decomposition of tetradecyltrimethylammonium-thiomolybdate-thiotungstate-cobaltate (II)

5.4 Conclusion

Facile and greener synthesis approach for sulfidation of supported metal oxide catalysts based on a (3-Mercaptopropyl)trimethoxysilane silica precursor that doubles as a sulfur precursor in a hydrothermal synthesis approach was developed. The performance was evaluated based on the activation approach used. Ar- and H_2-treated catalysts presented high BET surface area and total pore volume characteristics of supported catalysts, and further demonstrated better Mo sulfidation. The H_2-treated catalyst demonstrated higher HDS activity in accordance with its better active phase properties which makes the H_2 activation approach the best among the rest. The Ar- and H_2-treated catalysts direct the HDS reaction via both DDS and HYD pathway while air-treated catalyst directs the reaction via only the DDS pathway. The HDS reaction rate constant of H_2-treated catalyst compares well with severally reported rate constants thus demonstrated the success of the novel approach which in addition to reducing the synthesis steps also eliminate the use of toxic sulfidation chemicals such as hydrogen sulfide and carbon disulfide.

CHAPTER 6

CONCLUSION

The demand for highly active hydrodesulfurization (HDS) catalysts will continue to increase due to the increasing stringent environmental regulations. With the current European regulation of near zero ppm sulfur in vehicle fuel, the refineries are under great pressure to meet the requirement through research.

It has been discovered that the use of heteroatom such as Al, Ti and Zr into the framework of mesoporous SBA-15 silica support enhanced both the support acidity and metal support interaction, which lead to better active phase dispersion on the support and ultimately higher HDS activity.

We built on the existing knowledge by incorporating Ce into the silica support framework. In addition to its redox properties, the acid-base property is yet another exploitable property of ceria that has been utilized in developing a lot of catalysts for different applications such as hydrogenation and hydrogenolysis. Therefore, we modified the silica framework of SBA-15 support by incorporation of ceria (using as-prepared ceria isopropoxide precursor) and studied the resultant effect on the sulfided-CoMo catalyst for HDS of DBT. The role of ceria on the product selectivity and kinetic parameters of the HDS process were evaluated and a plausible mechanism was proposed. We discovered that Ce loading up to 2.5 wt.% facilitate the reduction of MoO_3 and prevent the formation of the inactive $CoMoO_4$ phase, which results in better Mo reduction and dispersion. Consequently, the 2.5CeOx-Si-CoMo showed exceedingly better HDS performance than Si-CoMo and the

other CeOx-Si-CoMo catalysts in the series. Subsequent modification of SBA-15 with ceria and zirconia biheteroatoms and loading of Ni and Mo also presented higher dibenzothiophene conversion in commercial diesel which was correlated to the electronic effect due to the biheteroatoms modification. Disturbed by the unsafe handling of toxic CS_2 or H_2S during the catalyst sulfidation process, we developed the use of (3-Mercaptopropyl)trimethoxysilane as sulfidation source in addition to the silica support source and completely eliminate the direct usage of CS_2 or H_2S.The new approach is considered greener method of HDS catalyst activation.

References

[1] A.M. Omer, Energy, environment and sustainable development, Renew. Sustain. Energy Rev. 12 (2008) 2265–2300.

[2] M. Asif, T. Muneer, Energy supply, its demand and security issues for developed and emerging economies, Renew. Sustain. Energy Rev. 11 (2007) 1388–1413.

[3] N.K. Arora, Environmental Sustainability—necessary for survival, Environ. Sustain. 1 (2018) 1–2.

[4] G.P. Peters, R.M. Andrew, T. Boden, J.G. Canadell, P. Ciais, C. Le Quéré, G. Marland, M.R. Raupach, C. Wilson, The challenge to keep global warming below 2 °C, Nat. Clim. Chang. 3 (2013) 4–6.

[5] Z. Han, F. Qi, H. Wang, B. Liu, X. Shen, C. Song, Z. Bao, X. Zhao, Y. Xu, D. Sun, Emission characteristics of volatile sulfur compounds (VSCs) from a municipal sewage sludge aerobic composting plant, Waste Manag. 77 (2018) 593–602.

[6] E. Sadeghi Meresht, T. Shahrabi Farahani, J. Neshati, Failure analysis of stress corrosion cracking occurred in a gas transmission steel pipeline, Eng. Fail. Anal. 18 (2011) 963–970.

[7] V.C. Srivastava, RSC Advances An evaluation of desulfurization technologies for sulfur removal from liquid fuels, RSC Adv. 2 (2012) 759–783.

[8] Honeywell, ULTIMet^{TM} | Honeywell UOP, (2017). https://www.uop.com/products/catalysts/hydroprocessing/ultimet/

[9] M. Bhaskar, G. Valavarasu, B. Sairam, K.S. Balaraman, K. Balu, Three-Phase Reactor Model to Simulate the Performance of Pilot-Plant and Industrial Trickle-

Bed Reactors Sustaining Hydrotreating Reactions, Ind. Eng. Chem. Res. 43 (2004) 6654–6669.

[10] I. Babich, J. Moulijn, Science and technology of novel processes for deep desulfurization of oil refinery streams: a review, Fuel. 82 (2003) 607–631.

[11] Stratas Advisors, A Global Overview and Outlook of On-Road Diesel Quality, Vehicle Emissions and Fuel Efficiency | Stratas Advisors, (n.d.). https://stratasadvisors.com/Insights/110118-On-Road-Diesel-Quality.

[12] T. Huang, J. Xu, Y. Fan, Effects of concentration and microstructure of active phases on the selective hydrodesulfurization performance of sulfided CoMo/Al_2O_3 catalysts, Appl. Catal. B Environ. 220 (2018) 42–56.

[13] A.S. Jalilov, A. Tanimu, S.A. Ganiyu, K. Alhooshani, Kinetic and Mechanistic Analysis of Dibenzothiophene Hydrodesulfurization on Ti-SBA-15–NiMo Catalysts, Energy & Fuels. 32 (2018) 11383–11389.

[14] M.Á. Calderón-Magdaleno, J.A. Mendoza-Nieto, T.E. Klimova, Effect of the amount of citric acid used in the preparation of NiMo/SBA-15 catalysts on their performance in HDS of dibenzothiophene-type compounds, in: Catal. Today, 2014: pp. 78–88.

[15] F.J. Méndez, O.E. Franco-López, X. Bokhimi, D.A. Solís-Casados, L. Escobar-Alarcón, T.E. Klimova, Dibenzothiophene hydrodesulfurization with NiMo and CoMo catalysts supported on niobium-modified MCM-41, Appl. Catal. B Environ. 219 (2017) 479–491.

[16] Y. Huang, Z. Zhou, Y. Qi, X. Li, Z. Cheng, W. Yuan, Hierarchically macro-/mesoporous structured Co–Mo–Ni/γ-Al_2O_3 catalyst for the hydrodesulfurization of

thiophene, Chem. Eng. J. 172 (2011) 444–451.

[17] G.H. Singhal, R.L. Espino, J.E. Sobel, G.A. Huff, Hydrodesulfurization of sulfur heterocyclic compounds: Kinetics of dibenzothiophene, J. Catal. 67 (1981) 457–468.

[18] M. Egorova, R. Prins, Hydrodesulfurization of dibenzothiophene and 4,6-dimethyldibenzothiophene over sulfided NiMo/γ-Al_2O_3, CoMo/γ-Al_2O_3, and Mo/γ-Al_2O_3 catalysts, J. Catal. 225 (2004) 417–427.

[19] F. Bataille, J.L. Lemberton, G. Pérot, P. Leyrit, T. Cseri, N. Marchal, S. Kasztelan, Sulfided Mo and CoMo supported on zeolite as hydrodesulfurization catalysts: transformation of dibenzothiophene and 4,6-dimethyldibenzothiophene, Appl. Catal. A Gen. 220 (2001) 191–205.

[20] A. Stanislaus, A. Marafi, M.S. Rana, Recent advances in the science and technology of ultra low sulfur diesel (ULSD) production, Catal. Today. 153 (2010) 1–68.

[21] R. Huirache-Acuña, R. Nava, C. Peza-Ledesma, J. Lara-Romero, G. Alonso-Núez, B. Pawelec, E. Rivera-Muñoz, SBA-15 Mesoporous Silica as Catalytic Support for Hydrodesulfurization Catalysts—Review, Materials (Basel). 6 (2013) 4139–4167.

[22] M. Egorova, R. Prins, The role of Ni and Co promoters in the simultaneous HDS of dibenzothiophene and HDN of amines over Mo/γ-Al_2O_3 catalysts, J. Catal. 241 (2006) 162–172.

[23] V. Sundaramurthy, I. Eswaramoorthi, A.K. Dalai, J. Adjaye, Hydrotreating of gas oil on SBA-15 supported NiMo catalysts, Microporous Mesoporous Mater. 111 (2008) 560–568.

[24] S. Badoga, K.C. Mouli, K.K. Soni, A.K. Dalai, J. Adjaye, Beneficial influence of

EDTA on the structure and catalytic properties of sulfided NiMo/SBA-15 catalysts for hydrotreating of light gas oil, Appl. Catal. B Environ. 125 (2012) 67–84.

[25] O.Y. Gutiérrez, S. Singh, E. Schachtl, J. Kim, E. Kondratieva, J. Hein, J.A. Lercher, Effects of the Support on the Performance and Promotion of (Ni)MoS_2 Catalysts for Simultaneous Hydrodenitrogenation and HydrodesulfurizationEffects of the Support on the Performance and Promotion of (Ni)MoS_2 Catalysts for Simultaneous Hydrodenitrogenation, ACS Catal. 4 (2014) 1487–1499.

[26] Y. Fan, H. Xiao, G. Shi, H. Liu, X. Bao, A novel approach for modulating the morphology of supported metal nanoparticles in hydrodesulfurization catalysts, Energy Environ. Sci. 4 (2011) 572–582.

[27] X. Wang, Z. Zhao, P. Zheng, Z. Chen, A. Duan, C. Xu, J. Jiao, H. Zhang, Z. Cao, B. Ge, Synthesis of NiMo catalysts supported on mesoporous Al_2O_3 with different crystal forms and superior catalytic performance for the hydrodesulfurization of dibenzothiophene and 4,6-dimethyldibenzothiophene, J. Catal. 344 (2016) 680–691.

[28] F.J. Méndez, A. Llanos, M. Echeverría, R. Jáuregui, Y. Villasana, Y. Díaz, G. Liendo-Polanco, M.A. Ramos-García, T. Zoltan, J.L. Brito, Mesoporous catalysts based on Keggin-type heteropolyacids supported on MCM-41 and their application in thiophene hydrodesulfurization, Fuel. 110 (2013) 249–258.

[29] F. Liu, S. Xu, Y. Chi, D. Xue, A novel alumina-activated carbon composite supported NiMo catalyst for hydrodesulfurization of dibenzothiophene, Catal. Commun. 12 (2011) 521–524.

[30] L. Zhang, Q. Dai, W. Fu, T. Tang, P. Dong, M. He, Q. Chen, CoMo catalyst on zeolite TS-1 nanorod assemblies with high activity in the hydrodesulfurization of

4,6-dimethyldibenzothiophene, J. Catal. 359 (2018) 130–142.

[31] K. Soni, B.S. Rana, A.K. Sinha, A. Bhaumik, M. Nandi, M. Kumar, G.M. Dhar, 3-D ordered mesoporous KIT-6 support for effective hydrodesulfurization catalysts, Appl. Catal. B Environ. 90 (2009) 55–63.

[32] I. Vázquez-Garrido, A. López-Benítez, G. Berhault, A. Guevara-Lara, Effect of support on the acidity of NiMo/Al_2O_3-MgO and NiMo/TiO_2-Al_2O_3 catalysts and on the resulting competitive hydrodesulfurization/hydrodenitrogenation reactions, Fuel. 236 (2019) 55–64.

[33] W. Han, H. Nie, X. Long, M. Li, Q. Yang, D. Li, Effects of the support Brønsted acidity on the hydrodesulfurization and hydrodenitrogention activity of sulfided NiMo/Al_2O_3 catalysts, Catal. Today. 292 (2017) 58–66.

[34] S.A. Yashnik, G.A. Urzhuntsev, A.I. Stadnichenko, D.A. Svintsitskiy, A. V. Ishchenko, A.I. Boronin, Z.R. Ismagilov, Effect of Pd- precursor and support acid properties on the Pd electronic state and the hydrodesulfurization activity of Pd-zeolite catalysts, Catal. Today. 323 (2019) 257–270.

[35] M. Zhang, J. Fan, K. Chi, A. Duan, Z. Zhao, X. Meng, H. Zhang, Synthesis, characterization, and catalytic performance of NiMo catalysts supported on different crystal alumina materials in the hydrodesulfurization of diesel, Fuel Process. Technol. 156 (2017) 446–453.

[36] Y. Dong, Y. Xu, Y. Zhang, X. Lian, X. Yi, Y. Zhou, W. Fang, Synthesis of hierarchically structured alumina support with adjustable nanocrystalline aggregation towards efficient hydrodesulfurization, Appl. Catal. A Gen. 559 (2018) 30–39.

[37] S. Shan, P. Yuan, W. Han, G. Shi, X. Bao, Supported NiW catalysts with tunable size and morphology of active phases for highly selective hydrodesulfurization of fluid catalytic cracking naphtha, J. Catal. 330 (2015) 288–301.

[38] J. Liu, Y. Li, Y. Li, S. Sang, S. Li, Effects of pore structure on thermal conductivity and strength of alumina porous ceramics using carbon black as pore-forming agent, Ceram. Int. 42 (2016) 8221–8228.

[39] F. Cao, L. Ren, X. Li, Synthesis of high strength monolithic alumina aerogels at ambient pressure, RSC Adv. 5 (2015) 18025–18028.

[40] L. Qu, W. Zhang, P.J. Kooyman, R. Prins, MAS NMR, TPR, and TEM studies of the interaction of NiMo with alumina and silica-alumina supports, J. Catal. 215 (2003) 7–13.

[41] S. Badoga, A.K. Dalai, J. Adjaye, Y. Hu, Combined effects of EDTA and heteroatoms (Ti, Zr, and Al) on catalytic activity of SBA-15 supported NiMo catalyst for hydrotreating of heavy gas oil, Ind. Eng. Chem. Res. 53 (2014) 2137–2156.

[42] F. Jiao, H. Frei, Nanostructured Cobalt Oxide Clusters in Mesoporous Silica as Efficient Oxygen-Evolving Catalysts, Angew. Chemie Int. Ed. 48 (2009) 1841–1844.

[43] Y. Li, W.-N. Wang, Z. Zhan, M.-H. Woo, C.-Y. Wu, P. Biswas, Photocatalytic reduction of CO_2 with H_2O on mesoporous silica supported Cu/TiO_2 catalysts, Appl. Catal. B Environ. 100 (2010) 386–392.

[44] S.H. Joo, J.Y. Park, C.-K. Tsung, Y. Yamada, P. Yang, G.A. Somorjai, Thermally stable Pt/mesoporous silica core–shell nanocatalysts for high-temperature reactions,

Nat. Mater. 8 (2009) 126–131.

[45] X. Zhou, A. Duan, Z. Zhao, Y. Gong, H. Wu, J. Li, Y. Wei, G. Jiang, J. Liu, Y. Zhang, Synthesis of hierarchically porous silicas with mesophase transformations in a four-component microemulsion-type system and the catalytic performance for dibenzothiophene hydrodesulfurization, J. Mater. Chem. A. 2 (2014) 6823–6833.

[46] M.T. Nguyen Dinh, P. Rajbhandari, C. Lancelot, P. Blanchard, C. Lamonier, M. Bonne, S. Royer, F. Dumeignil, E. Payen, Tuning Hydrodesulfurization Active-Phase Dispersion using Optimized Mesoporous Titania-Doped Silica Supports, ChemCatChem. 6 (2014) 328–338.

[47] S.J. Danforth, D.R. Liyanage, A. Hitihami-Mudiyanselage, B. Ilic, S.L. Brock, M.E. Bussell, Probing hydrodesulfurization over bimetallic phosphides using monodisperse $Ni_{2-x}M_xP$ nanoparticles encapsulated in mesoporous silica, Surf. Sci. 648 (2016) 126–135.

[48] P. Rayo, J. Ramírez, M.S. Rana, J. Ancheyta, A. Aguilar-Elguézabal, Effect of the incorporation of Al, Ti, and Zr on the cracking and hydrodesulfurization activity of NiMo/SBA-15 catalysts, Ind. Eng. Chem. Res. 48 (2009) 1242–1248.

[49] L.Y. Lizama, T.E. Klimova, SBA-15 modified with Al, Ti, or Zr as supports for highly active NiW catalysts for HDS, in: J. Mater. Sci., 2009: pp. 6617–6628.

[50] P. Biswas, P. Narayanasarma, C.M. Kotikalapudi, A.K. Dalai, J. Adjaye, Characterization and activity of ZrO_2 doped SBA-15 supported NiMo catalysts for HDS and HDN of bitumen derived heavy gas oil, Ind. Eng. Chem. Res. 50 (2011) 7882–7895.

[51] S.A. Ganiyu, K. Alhooshani, S.A. Ali, Single-pot synthesis of Ti-SBA-15-NiMo

hydrodesulfurization catalysts: Role of calcination temperature on dispersion and activity, Appl. Catal. B Environ. 203 (2017) 428–441.

[52] S.A. Ganiyu, S.A. Ali, K. Alhooshani, Synthesis of a Ti-SBA-15-NiMo Hydrodesulfurization Catalyst: The Effect of the Hydrothermal Synthesis Temperature of NiMo and Molybdenum Loading on the Catalytic Activity, Ind. Eng. Chem. Res. 56 (2017) 5201–5209.

[53] S. Jiang, Y. Zhou, S. Ding, Q. Wei, W. Zhou, Y. Shan, Effect of direct synthesis Al–SBA-15 supports on the morphology and catalytic activity of the NiMoS phase in HDS of DBT, RSC Adv. 6 (2016) 106680–106689.

[54] C. Suresh, L.P. Cabrera, J.A. Aliaga, J.N.D. de León, T.A. Zepeda, S. Fuentes, G. Berhault, G. Alonso-Núñez, Formation of Co-Promoted MoS_2 Fullerene-Like Nanostructures on SBA-15 as Effective Hydrodesulfurization Catalyst, Catal. Letters. 147 (2017) 46–57.

[55] D. Valencia, T. Klimova, Effect of the support composition on the characteristics of NiMo and CoMo/(Zr)SBA-15 catalysts and their performance in deep hydrodesulfurization, Catal. Today. 166 (2011) 91–101.

[56] K. Chandra Mouli, S. Mohanty, Y. Hu, A. Dalai, J. Adjaye, Effect of hetero atom on dispersion of NiMo phase on M-SBA-15 (M = Zr, Ti, Ti-Zr), in: Catal. Today, Elsevier, 2013: pp. 133–144.

[57] J.C. Morales-Ortuño, T.E. Klimova, Development of new hydrodesulfurization NiMo catalysts supported on Al_2O_3-TiSBA-15 hybrid materials, Fuel. 198 (2017) 99–109.

[58] J.A. Mendoza-Nieto, O. Vera-Vallejo, L. Escobar-Alarcón, D. Solís-Casados, T.

Klimova, Development of new trimetallic NiMoW catalysts supported on SBA-15 for deep hydrodesulfurization, Fuel. 110 (2013) 268–277.

[59] M.A. López-Mendoza, R. Nava, C. Peza-Ledesma, B. Millán-Malo, R. Huirache-Acuña, P. Skewes, E.M. Rivera-Muñoz, Characterization and catalytic performance of Co-Mo-W sulfide catalysts supported on SBA-15 and SBA-16 mechanically mixed, Catal. Today. 271 (2016) 114–126.

[60] C. Suresh, L. Pérez-Cabrera, J.N. Díaz de León, T.A. Zepeda, G. Alonso-Núñez, S.F. Moyado, Highly active CoMo/Al (10) KIT-6 catalysts for HDS of DBT: Role of structure and aluminum heteroatom in the support matrix, Catal. Today. 296 (2017) 214–218.

[61] A. Duan, T. Li, Z. Zhao, B. Liu, X. Zhou, G. Jiang, J. Liu, Y. Wei, H. Pan, Synthesis of hierarchically porous L-KIT-6 silica–alumina material and the super catalytic performances for hydrodesulfurization of benzothiophene, Appl. Catal. B Environ. 165 (2015) 763–773.

[62] H. Wu, A. Duan, Z. Zhao, T. Li, R. Prins, X. Zhou, Synthesis of NiMo hydrodesulfurization catalyst supported on a composite of nano-sized ZSM-5 zeolite enwrapped with mesoporous KIT-6 material and its high isomerization selectivity, J. Catal. 317 (2014) 303–317.

[63] Q. Gao, Y. Zhang, K. Zhou, H. Wu, J. Guo, L. Zhang, A. Duan, Z. Zhao, F. Zhang, Y. Zhou, Synthesis of ZSM-5/KIT-6 with a tunable pore structure and its catalytic application in the hydrodesulfurization of dibenzothiophene and diesel oil, RSC Adv. 8 (2018) 28879–28890.

[64] J. Fan, A. Duan, C. Xu, Z. Zhao, P. Zheng, X. Wang, H. Li, C. Xiao, J. Mei, G.

Jiang, Hydrodesulfurization Properties of Dibenzothiophene over NiMo Catalysts Supported on Cubic *Fm*3*m* Mesoporous Structure and High-Framework Aluminum-Modified AlKIT-5, Energy & Fuels. 32 (2018) 9793–9803.

[65] J. Shi, Y. Wang, W. Yang, Y. Tang, Z. Xie, Recent advances of pore system construction in zeolite-catalyzed chemical industry processes, Chem. Soc. Rev. 44 (2015) 8877–8903.

[66] M. Taniguchi, D. Imamura, H. Ishige, Y. Ishii, T. Murata, M. Hidai, T. Tatsumi, Hydrodesulfurization of benzothiophene over zeolite-supported catalysts prepared from Mo and Mo-Ni sulfide clusters, J. Catal. 187 (1999) 139–150.

[67] W. Fu, L. Zhang, T. Tang, Q. Ke, S. Wang, J. Hu, G. Fang, J. Li, F.-S. Xiao, Extraordinarily High Activity in the Hydrodesulfurization of 4,6-Dimethyldibenzothiophene over Pd Supported on Mesoporous Zeolite Y, J. Am. Chem. Soc. 133 (2011) 15346–15349.

[68] S. Al-Khattaf, Catalytic transformation of toluene over a high-Acidity Y-zeolite based catalyst, Energy and Fuels. 20 (2006) 946–954.

[69] T. Tang, L. Zhang, W. Fu, Y. Ma, J. Xu, J. Jiang, G. Fang, F.-S. Xiao, Design and Synthesis of Metal Sulfide Catalysts Supported on Zeolite Nanofiber Bundles with Unprecedented Hydrodesulfurization Activities, J. Am. Chem. Soc. 135 (2013) 11437–11440.

[70] B. Liu, Z. Zhao, D. Wang, J. Liu, Y. Chen, T. Li, A. Duan, G. Jiang, A theoretical study on the mechanism for thiophene hydrodesulfurization over zeolite L-supported sulfided CoMo catalysts: Insight into the hydrodesulfurization over zeolite-based catalysts, Comput. Theor. Chem. 1052 (2015) 47–57.

[71] Q. Huo, Y. Gong, T. Dou, Z. Zhao, H. Pan, F. Deng, Novel Micro- and Mesoporous Composite Molecular Sieve Assembled by Zeolite L Nanocrystal and Its Performance for the Hydrodesulfurization (HDS) of Fluid Catalytic Cracking (FCC) Gasoline, Energy & Fuels. 24 (2010) 3764–3771.

[72] W. Zhou, M. Liu, Q. Zhang, Q. Wei, S. Ding, Y. Zhou, Synthesis of NiMo Catalysts Supported on Gallium-Containing Mesoporous Y Zeolites with Different Gallium Contents and Their High Activities in the Hydrodesulfurization of 4,6-Dimethyldibenzothiophene, ACS Catal. 7 (2017) 7665–7679.

[73] X. Wang, J. Mei, Z. Zhao, P. Zheng, Z. Chen, D. Gao, J. Fu, J. Fan, A. Duan, C. Xu, Self-Assembly of Hierarchically Porous ZSM-5/SBA-16 with Different Morphologies and Its High Isomerization Performance for Hydrodesulfurization of Dibenzothiophene and 4,6-Dimethyldibenzothiophene, ACS Catal. 8 (2018) 1891–1902.

[74] X. Wang, Y. Li, K. Chi, Z. Zhao, P. Du, J. Mei, P. Zheng, J. Fan, A. Duan, C. Xu, Optimal Synthesis of Hierarchical Porous Composite ZSM-5/SBA-16 for Ultradeep Hydrodesulfurization of Dibenzothiophene and 4,6-Dimethyldibenzothiophene. Part 1: The Influence of Inorganic Salt on the Properties of NiMo Catalysts, Energy & Fuels. 32 (2018) 6204–6212.

[75] Q. Gao, Y. Zhang, K. Zhou, H. Wu, J. Guo, L. Zhang, A. Duan, Z. Zhao, F. Zhang, Y. Zhou, Synthesis of ZSM-5/KIT-6 with a tunable pore structure and its catalytic application in the hydrodesulfurization of dibenzothiophene and diesel oil, RSC Adv. 8 (2018) 28879–28890.

[76] R. Madlener, Y. Sunak, Impacts of urbanization on urban structures and energy

demand: What can we learn for urban energy planning and urbanization management?, Sustain. Cities Soc. 1 (2011) 45–53.

[77] S. Shafiee, E. Topal, When will fossil fuel reserves be diminished?, Energy Policy. 37 (2009) 181–189.

[78] Z. Vít, D. Gulková, L. Kaluža, J. Kupčík, Pd–Pt catalysts on mesoporous SiO_2–Al_2O_3 with superior activity for HDS of 4,6-dimethyldibenzothiophene: Effect of metal loading and support composition, Appl. Catal. B Environ. 179 (2015) 44–53.

[79] K. Szczodrowski, B. Prélot, S. Lantenois, J.M. Douillard, J. Zajac, Effect of heteroatom doping on surface acidity and hydrophilicity of Al, Ti, Zr-doped mesoporous SBA-15, Microporous Mesoporous Mater. 124 (2009) 84–93.

[80] C.G. Piscopo, J. Tochtermann, M. Schwarzer, D. Boskovic, R. Maggi, G. Maestri, S. Loebbecke, Titania supported on silica as an efficient catalyst for deep oxidative desulfurization of a model fuel with exceptionally diluted H_2O_2, React. Chem. Eng. 3 (2018) 13–16.

[81] L. Díaz-García, V. Santes, T. Viveros-García, A. Sánchez-Trujillo, J. Ramírez-Salgado, C. Ornelas, E. Rodríguez-Castellón, Electronic binding of sulfur sites into Al_2O_3-ZrO_2 supports for NiMoS configuration and their application for Hydrodesulfurization, Catal. Today. 282 (2017) 230–239.

[82] F.J. Méndez, G. Bravo-Ascención, M. González-Mota, I. Puente-Lee, X. Bokhimi, T.E. Klimova, NiMo catalysts supported on Al, Nb, Ti or Zr-containing MCM-41 for dibenzothiophene hydrodesulfurization, Catal. Today. (2018).

[83] S. Wu, Y. Han, Y.C. Zou, J.W. Song, L. Zhao, Y. Di, S.Z. Liu, F.S. Xiao, Synthesis of Heteroatom Substituted SBA-15 by the “pH-Adjusting” Method, Chem. Mater.

16 (2004) 486–492.

[84] K.K. Soni, K. Chandra Mouli, A.K. Dalai, J. Adjaye, Effect of Ti loading on the HDS and HDN activity of KLGO on NiMo/TiSBA-15 catalysts, Microporous Mesoporous Mater. 152 (2012) 224–234.

[85] Z. Wu, A.K.P. Mann, M. Li, S.H. Overbury, Spectroscopic Investigation of Surface-Dependent Acid–Base Property of Ceria Nanoshapes, J. Phys. Chem. C. 119 (2015) 7340–7350.

[86] Y. Wang, F. Wang, Q. Song, Q. Xin, S. Xu, J. Xu, Heterogeneous Ceria Catalyst with Water-Tolerant Lewis Acidic Sites for One-Pot Synthesis of 1,3-Diols via Prins Condensation and Hydrolysis Reactions, J. Am. Chem. Soc. 135 (2013) 1506–1515.

[87] S. Zhang, Z.Q. Huang, Y. Ma, W. Gao, J. Li, F. Cao, L. Li, C.R. Chang, Y. Qu, Solid frustrated-Lewis-pair catalysts constructed by regulations on surface defects of porous nanorods of CeO_2, Nat. Commun. 8 (2017) 15266.

[88] L. Vivier, D. Duprez, Ceria-Based Solid Catalysts for Organic Chemistry, ChemSusChem. 3 (2010) 654–678.

[89] S. Akbayrak, Y. Tonbul, S. Özkar, Ceria supported rhodium nanoparticles: Superb catalytic activity in hydrogen generation from the hydrolysis of ammonia borane, Appl. Catal. B Environ. 198 (2016) 162–170.

[90] D. Zhao, Triblock Copolymer Syntheses of Mesoporous Silica with Periodic 50 to 300 Angstrom Pores, Science (80-). 279 (1998) 548–552.

[91] A. Tanimu, S.A. Ganiyu, O. Muraza, K. Alhooshani, Palladium nanoparticles supported on ceria thin film for capillary microreactor application, Chem. Eng. Res. Des. 132 (2018).

[92] R.M. Rioux, H. Song, J.D. Hoefelmeyer, P. Yang, G.A. Somorjai, High-surface-area catalyst design: Synthesis, characterization, and reaction studies of platinum nanoparticles in mesoporous SBA-15 silica, J. Phys. Chem. B. 109 (2005) 2192–2202.

[93] M.N. Timofeeva, S.H. Jhung, Y.K. Hwang, D.K. Kim, V.N. Panchenko, M.S. Melgunov, Y.A. Chesalov, J.S. Chang, Ce-silica mesoporous SBA-15-type materials for oxidative catalysis: Synthesis, characterization, and catalytic application, Appl. Catal. A Gen. 317 (2007) 1–10.

[94] P. Velmurugan, J. Shim, K.J. Lee, M. Cho, S.S. Lim, S.K. Seo, K.M. Cho, K.S. Bang, B.T. Oh, Extraction, characterization, and catalytic potential of amorphous silica from corn cobs by sol-gel method, J. Ind. Eng. Chem. 29 (2015) 298–303.

[95] Q. Dai, X. Wang, G. Chen, Y. Zheng, G. Lu, Direct synthesis of Cerium(III)-incorporated SBA-15 mesoporous molecular sieves by two-step synthesis method, Microporous Mesoporous Mater. 100 (2007).

[96] H.P. Zhang, H.F. Lin, Y. Zheng, Y.F. Hu, A. MacLennan, The catalytic activity and chemical structure of nano MoS_2 synthesized in a controlled environment, React. Chem. Eng. 1 (2016) 165–175.

[97] Y. Li, Z. Feng, Y. Lian, K. Sun, L. Zhang, G. Jia, Q. Yang, C. Li, Direct synthesis of highly ordered Fe-SBA-15 mesoporous materials under weak acidic conditions, Microporous Mesoporous Mater. 84 (2005) 41–49.

[98] T. Taniguchi, T. Watanabe, N. Sugiyama, A.K. Subramani, H. Wagata, N. Matsushita, M. Yoshimura, Identifying Defects in Ceria-Based Nanocrystals by UV Resonance Raman Spectroscopy, J. Phys. Chem. C. 113 (2009) 19789–19793.

[99] B.C. Windom, W.G. Sawyer, D.W. Hahn, A Raman Spectroscopic Study of MoS_2 and MoO_3: Applications to Tribological Systems, Tribol. Lett. 42 (2011) 301–310.

[100] H. Li, Q. Zhang, C.C.R. Yap, B.K. Tay, T.H.T. Edwin, A. Olivier, D. Baillargeat, From Bulk to Monolayer MoS_2: Evolution of Raman Scattering, Adv. Funct. Mater. 22 (2012) 1385–1390.

[101] M.D. Kadgaonkar, S.C. Laha, R.K. Pandey, P. Kumar, S.P. Mirajkar, R. Kumar, Cerium-containing MCM-41 materials as selective acylation and alkylation catalysts, in: Catal. Today, 2004: pp. 225–231.

[102] S.C. Laha, P. Mukherjee, S.R. Sainkar, R. Kumar, Cerium containing mcm-41-type mesoporous materials and their acidic and redox catalytic properties, J. Catal. 207 (2002) 213–223.

[103] M.. Abello, M.. Gomez, O. Ferretti, Mo/γ-Al_2O_3 catalysts for the oxidative dehydrogenation of propane.: Effect of Mo loading, Appl. Catal. A Gen. 207 (2001) 421–431.

[104] J. Li, G. Jacobs, Y. Zhang, T. Das, B.H. Davis, Fischer–Tropsch synthesis: effect of small amounts of boron, ruthenium and rhenium on Co/TiO_2 catalysts, Appl. Catal. A Gen. 223 (2002) 195–203.

[105] C.T. Campbell, C.H.F. Peden, Chemistry. Oxygen vacancies and catalysis on ceria surfaces., Science. 309 (2005) 713–4.

[106] F. Esch, S. Fabris, L. Zhou, T. Montini, C. Africh, P. Fornasiero, G. Comelli, R. Rosei, Electron localization determines defect formation on ceria substrates., Science. 309 (2005) 752–5.

[107] T.A. Zepeda, Comparison and performance of different sulphided Ti-loaded

mesostructured silica-supported CoMo catalysts in deep HDS, Appl. Catal. A Gen. 347 (2008) 148–161.

[108] W. Zhou, Q. Wei, Y. Zhou, M. Liu, S. Ding, Q. Yang, Hydrodesulfurization of 4,6-dimethyldibenzothiophene over NiMo sulfide catalysts supported on meso-microporous Y zeolite with different mesopore sizes, Appl. Catal. B Environ. 238 (2018) 212–224.

[109] S. Che, K. Lund, T. Tatsumi, S. Iijima, S.H. Joo, R. Ryoo, O. Terasaki, Direct Observation of 3D Mesoporous Structure by Scanning Electron Microscopy (SEM): SBA-15 Silica and CMK-5 Carbon, Angew. Chemie Int. Ed. 42 (2003) 2182–2185.

[110] H. Tüysüz, C.W. Lehmann, H. Bongard, B. Tesche, R. Schmidt, F. Schüth, Direct Imaging of Surface Topology and Pore System of Ordered Mesoporous Silica (MCM-41, SBA-15, and KIT-6) and Nanocast Metal Oxides by High Resolution Scanning Electron Microscopy, J. Am. Chem. Soc. 130 (2008) 11510–11517.

[111] J. Liang, M. Wu, J. Wang, P. Wei, B. Sun, Y. Lu, D. Sun, Y. Liu, C. Liu, A new approach to construct a hydrodesulfurization catalyst from a crystalline precursor: ligand-induced self-assembly, sulfidation and hydrodesulfurization, Catal. Sci. Technol. 8 (2018) 6330–6345.

[112] V.M. Kogan, P.A. Nikulshin, On the dynamic model of promoted molybdenum sulfide catalysts, Catal. Today. 149 (2010) 224–231.

[113] H. Liu, C. Liu, C. Yin, Y. Chai, Y. Li, D. Liu, B. Liu, X. Li, Y. Wang, X. Li, Preparation of highly active unsupported nickel-zinc-molybdenum catalysts for the hydrodesulfurization of dibenzothiophene, Appl. Catal. B Environ. 174–175 (2015) 264–276.

[114] H. Li, W. Zhu, S. Zhu, J. Xia, Y. Chang, W. Jiang, M. Zhang, Y. Zhou, H. Li, The selectivity for sulfur removal from oils: An insight from conceptual density functional theory, AIChE J. 62 (2016) 2087–2100.

[115] H. Liu, C. Yin, B. Liu, X. Li, Y. Li, Y. Chai, C. Liu, Effect of Calcination Temperature of Unsupported NiMo Catalysts on the Hydrodesulfurization of Dibenzothiophene, Energy & Fuels. 28 (2014) 2429–2436.

[116] P. Michaud, J.. Lemberton, G. Pérot, Hydrodesulfurization of dibenzothiophene and 4,6-dimethyldibenzothiophene: Effect of an acid component on the activity of a sulfided NiMo on alumina catalyst, Appl. Catal. A Gen. 169 (1998) 343–353.

[117] F. Rashidi, T. Sasaki, A.M. Rashidi, A. Nemati Kharat, K.J. Jozani, Ultradeep hydrodesulfurization of diesel fuels using highly efficient nanoalumina-supported catalysts: Impact of support, phosphorus, and/or boron on the structure and catalytic activity, J. Catal. 299 (2013) 321–335.

[118] E. Payen, R. Hubaut, S. Kasztelan, O. Poulet, J. Grimblot, Morphology Study of MOS_2- and WS_2-Based Hydrotreating Catalysts by High-Resolution Electron Microscopy, J. Catal. 147 (1994) 123–132.

[119] J.A. Bergwerff, M. Jansen, B. (R). G. Leliveld, T. Visser, K.P. de Jong, B.M. Weckhuysen, Influence of the preparation method on the hydrotreating activity of MoS_2/Al_2O_3 extrudates: A Raman microspectroscopy study on the genesis of the active phase, J. Catal. 243 (2006) 292–302.

[120] Y. V. Joshi, P. Ghosh, M. Daage, W.N. Delgass, Support effects in HDS catalysts: DFT analysis of thiolysis and hydrolysis energies of metal-support linkages, J. Catal. 257 (2008) 71–80.

[121] K.C. Mouli, K. Soni, A. Dalai, J. Adjaye, Applied Catalysis A : General Effect of pore diameter of Ni – Mo / Al-SBA-15 catalysts on the hydrotreating of heavy gas oil, "Applied Catal. A, Gen. 404 (2011) 21–29.

[122] L. Peña, D. Valencia, T. Klimova, CoMo/SBA-15 catalysts prepared with EDTA and citric acid and their performance in hydrodesulfurization of dibenzothiophene, Appl. Catal. B Environ. 147 (2014) 879–887.

[123] A. Tanimu, S.A. Ganiyu, S. Adamu, K. Alhooshani, Synthesis, application and kinetic modeling of CeOx–Si–CoMo catalysts for the hydrodesulfurization of dibenzothiophene, React. Chem. Eng. (2019). doi:10.1039/C8RE00330K.

[124] S.K. Das, M.K. Bhunia, A. Bhaumik, Highly ordered Ti-SBA-15: Efficient H_2 adsorbent and photocatalyst for eco-toxic dye degradation, J. Solid State Chem. 183 (2010) 1326–1333.

[125] A. Tanimu, S.A. Ganiyu, S. Adamu, K. Alhooshani, Synthesis, application and kinetic modeling of CeOx–Si–CoMo catalysts for the hydrodesulfurization of dibenzothiophene, React. Chem. Eng. (2019). doi:10.1039/c8re00330k.

[126] J.-G. Yu, H.-G. Yu, B. Cheng, X.-J. Zhao, J.C. Yu, W.-K. Ho, The Effect of Calcination Temperature on the Surface Microstructure and Photocatalytic Activity of TiO_2 Thin Films Prepared by Liquid Phase Deposition, J. Phys. Chem. B. 107 (2003) 13871–13879.

[127] H. Liu, Y.P. Li, C.L. Yin, Y.L. Wu, Y.M. Chai, D.M. Dong, X.H. Li, C.G. Liu, One-pot synthesis of ordered mesoporous NiMo-Al_2O_3 catalysts for dibenzothiophene hydrodesulfurization, Appl. Catal. B-Environmental. 198 (2016) 493–507.

[128] D.M. Do, S. Jaenicke, G.-K. Chuah, Mesoporous Zr-SBA-15 as a green solid acid

catalyst for the Prins reaction, Catal. Sci. Technol. 2 (2012) 1417.

[129] F. Jin, Y. Li, A FTIR and TPD examination of the distributive properties of acid sites on ZSM-5 zeolite with pyridine as a probe molecule, Catal. Today. 145 (2009) 101–107.

[130] M. Tamura, K. Shimizu, A. Satsuma, Comprehensive IR study on acid/base properties of metal oxides, Appl. Catal. A Gen. 433–434 (2012) 135–145.

[131] T. Klimova, L. Peña, L. Lizama, C. Salcedo, O.Y. Gutiérrez, Modification of activity and selectivity of NiMo/SBA-15 HDS catalysts by grafting of different metal oxides on the support surface, Ind. Eng. Chem. Res. 48 (2009) 1126–1133.

[132] W. Lai, Z. Chen, J. Zhu, L. Yang, J. Zheng, X. Yi, W. Fang, A NiMoS flower-like structure with self-assembled nanosheets as high-performance hydrodesulfurization catalysts, Nanoscale. 8 (2016) 3823–3833.

[133] A. Bodin, A.L.N. Christoffersen, C.F. Elkjær, M. Brorson, J. Kibsgaard, S. Helveg, I. Chorkendorff, Engineering Ni-Mo-S Nanoparticles for Hydrodesulfurization, Nano Lett. 18 (2018) 3454–3460.

[134] A. Mansouri, N. Semagina, Colloidal Synthesis Protocol of Shape- and Dimensionally- Controlled Transition-Metal Chalcogenides and Their Hydrodesulfurization Activities, ACS Appl. Nano Mater. 1 (2018) 4408–4412.

[135] J. Liang, M. Wu, P. Wei, J. Zhao, H. Huang, C. Li, Y. Lu, Y. Liu, C. Liu, Efficient hydrodesulfurization catalysts derived from Strandberg P–Mo–Ni polyoxometalates, J. Catal. 358 (2018) 155–167.

[136] A.N. Varakin, A. V. Mozhaev, A.A. Pimerzin, P.A. Nikulshin, Comparable investigation of unsupported MoS2hydrodesulfurization catalysts prepared by

different techniques: Advantages of support leaching method, Appl. Catal. B Environ. 238 (2018) 498–508.

[137] W. Song, W. Lai, Z. Chen, J. Cao, H. Wang, Y. Lian, W. Yang, X. Jiang, Fabrication of 3D Porous Hierarchical NiMoS Flowerlike Architectures for Hydrodesulfurization Applications, ACS Appl. Nano Mater. 1 (2018) 442–454.

[138] L. van Haandel, G.M. Bremmer, E.J.M. Hensen, T. Weber, The effect of organic additives and phosphoric acid on sulfidation and activity of (Co)Mo/Al_2O_3 hydrodesulfurization catalysts, J. Catal. 351 (2017) 95–106.

[139] J.A. Toledo-Antonio, M.A. Cortes-Jacome, J. Escobar-Aguilar, C. Angeles-Chavez, J. Navarrete-Bolaños, E. López-Salinas, Upgrading HDS activity of MoS_2 catalysts by chelating thioglycolic acid to MoOx supported on alumina, Appl. Catal. B Environ. 213 (2017) 106–117.

[140] J. Escobar, M.C. Barrera, A.W. Gutiérrez, J.E. Terrazas, Benzothiophene hydrodesulfurization over NiMo/alumina catalysts modified by citric acid. Effect of addition stage of organic modifier, Fuel Process. Technol. 156 (2017) 33–42.

[141] C.E. Santolalla-Vargas, V. Santes, C. Ortega-Niño, A. Hernández-Gordillo, F. Sanchez-Minero, L. Lartundo-Rojas, R. Borja-Urby, J.C. López-Curiel, O. Goiz, I.I. Padilla-Martinez, Effect of trimesic acid as chelating agent in sulfided CoMoP/γ-Al_2O_3 catalyst for hydrodesulfurization of straight-run gas oil, Catal. Today. (2018).

[142] J. Jiang, A. Chan, S. Ali, A. Saha, K.J. Haushalter, W.-L.M. Lam, M. Glasheen, J. Parker, M. Brenner, S.B. Mahon, H.H. Patel, R. Ambasudhan, S.A. Lipton, R.B. Pilz, G.R. Boss, Hydrogen Sulfide—Mechanisms of Toxicity and Development of an Antidote, Sci. Rep. 6 (2016) 20831.

[143] J. Jiao, J. Fu, Y. Wei, Z. Zhao, A. Duan, C. Xu, J. Li, H. Song, P. Zheng, X. Wang, Y. Yang, Y. Liu, Al-modified dendritic mesoporous silica nanospheres-supported NiMo catalysts for the hydrodesulfurization of dibenzothiophene: Efficient accessibility of active sites and suitable metal–support interaction, J. Catal. 356 (2017) 269–282.

[144] D. Kodjak, Policies to reduce fuel consumption, air pollution, and carbon emissions from vehicles in G20 nations, 2015. www.theicct.org (accessed October 16, 2018).

[145] G. Alonso-Núñez, J. Bocarando, R. Huirache-Acuña, L. Álvarez-Contreras, Z.D. Huang, W. Bensch, G. Berhault, J. Cruz, T.A. Zepeda, S. Fuentes, Influence of the activation atmosphere on the hydrodesulfurization of Co-Mo/SBA-15 catalysts prepared from sulfur-containing precursors, Appl. Catal. A Gen. 419–420 (2012) 95–101.

[146] Y. Yi, C.T. Williams, M. Glascock, G. Xiong, J. Lauterbach, C. Liang, Transformation of Mo and W thiosalts into unsupported sulfide catalysts: A temperature dependent in-situ spectroscopic investigation, Mater. Res. Bull. 56 (2014) 54–64.

[147] Y. Yi, B. Zhang, X. Jin, L. Wang, C.T. Williams, G. Xiong, D. Su, C. Liang, Unsupported NiMoW sulfide catalysts for hydrodesulfurization of dibenzothiophene by thermal decomposition of thiosalts, J. Mol. Catal. A Chem. 351 (2011) 120–127.

[148] R. Huirache-Acuña, G. Alonso-Núñez, F. Paraguay-Delgado, J. Lara-Romero, G. Berhault, E.M. Rivera-Muñoz, Unsupported trimetallic CoMoW sulfide HDS catalysts prepared by in situ decomposition of sulfur-containing precursors, Catal.

Today. 250 (2015) 28–37.

[149] R. Romero-Rivera, G. Berhault, G. Alonso-Núñez, M. Del Valle, F. Paraguay-Delgado, S. Fuentes, S. Salazar, A. Aguilar, J. Cruz-Reyes, Tungsten disulfide catalysts from tetraalkylammonium thiotungstates by ex situ activation, their properties and HDS activity, Appl. Catal. A Gen. 433–434 (2012) 115–121.

[150] L. Romero, M. Del Valle, R. Romero-Rivera, G. Alonso, M. Ávalos-Borja, S. Fuentes, F. Paraguay-Delgado, J. Cruz-Reyes, MoS_2 catalysts derived from n-methylenediammonium thiomolybdates during HDS of DBT, Catal. Today. 250 (2015) 66–71.

[151] Y. Espinoza-Armenta, J. Cruz-Reyes, F. Paraguay-Delgado, M. Del Valle, G. Alonso, S. Fuentes, R. Romero-Rivera, CoMoW sulfide nanocatalysts for the HDS of DBT from novel ammonium and alkyltrimethylammonium-thiomolybdatethiotungstate-cobaltate (II) precursors, Appl. Catal. A Gen. 486 (2014) 62–68.

[152] G. Alonso, M.H. Siadati, G. Berhault, A. Aguilar, S. Fuentes, R.R. Chianelli, Synthesis of tetraalkylammonium thiometallate precursors and their concurrent in situ activation during hydrodesulfurization of dibenzothiophene, Appl. Catal. A Gen. 263 (2004) 109–117.

[153] S. Ding, P. He, W. Feng, L. Li, G. Zhang, J. Chen, F. Dong, H. He, Novel molybdenum disulfide nanosheets-decorated polyaniline: Preparation, characterization and enhanced electrocatalytic activity for hydrogen evolution reaction, J. Phys. Chem. Solids. 91 (2016) 41–47.

[154] S. Liu, X. Zhang, H. Shao, J. Xu, F. Chen, Y. Feng, Preparation of MoS_2 nanofibers

by electrospinning, Mater. Lett. 73 (2012) 223–225.

[155] L.O. Aleman-Vazquez, E. Torres-Garcia, J.R. Villagomez-Ibarra, J.L. Cano-Dominguez, Effect of the particle size on the activity of MoOxCy catalysts for the isomerization of heptane, Catal. Letters. 100 (2005) 219–226.

[156] G. Alonso, J. Espino, G. Berhault, L. Alvarez, J.L. Rico, Activation of tetraalkylammonium thiotungstates for the preparation of Ni-promoted WS_2 catalysts, Appl. Catal. A Gen. 266 (2004) 29–40.

[157] S.P. Kelty, G. Berhault, R.R. Chianelli, The role of carbon in catalytically stabilized transition metal sulfides, Appl. Catal. A Gen. 322 (2007) 9–15.

Vitae

Name	:Abdulkadir Tanimu
Nationality	:Nigerian
Date of Birth	:6/22/1987
Email	:abdulkadir_tanimu@yahoo.com
Address	:Department of Chemistry, King Fahd University of Petroleum and Minerals
Academic Background	:BSc. Chemistry, Ahmadu Bello University, Zaria-Nigeria, 2009. MS. Chemistry, King Fahd University of Petroleum and Minerals, 2015.

Publications

- **Tanimu, A.**; Ganiyu, S. A.; Adamu, S.; Alhooshani, K. R. Synthesis, Application and Kinetic Modeling of CeOx-Si-CoMo Catalysts for Hydrodesulfurization of Dibenzothiophene**.** ***React. Chem. Eng.*** 2019, *4* (4), 724-737 (RSC_IF=4.641, Q1).

- **Tanimu, A.**; Jillani, S. M. S.; Alluhaidan, A. A.; Ganiyu, S. A.; Alhooshani, K. 4-Phenyl-1,2,3-Triazole Functionalized Mesoporous Silica SBA-15 as Sorbent in an Efficient Stir Bar-Supported Micro-Solid-Phase Extraction Strategy for Highly to Moderately Polar Phenols. ***Talanta*** 2019, *194*, 377–384. (Elservier_IF=4.244, Q1).

- **Tanimu, A.**; Alhooshani, K. Advanced hydrodesulfurization catalysts: A review of design and synthesis. ***Energy & Fuels*** 2019, *33*, 4, 2810–2838. (ACS_IF=3.024, Q2).

- Saleh, T. A.; Al-Hammadi, S. A.; **Tanimu, A.**; Alhooshani, K. Ultra-Deep Adsorptive Desulfurization of Fuels on Cobalt and Molybdenum Nanoparticles Loaded on Activated Carbon Derived from Waste Rubber. ***J. Colloid Interface Sci***. 2018, *513*. (Elservier_IF=5.091, Q1).

- **Tanimu, A.**; Ganiyu, S. A.; Muraza, O.; Alhooshani, K. Palladium Nanoparticles Supported on Ceria Thin Film for Capillary Microreactor Application. ***Chem. Eng. Res. Des***. 2018, *132*. (Elservier_IF=2.795, Q2).

- Jalilov, A. S.; **Tanimu, A.**; Ganiyu, S. A.; Alhooshani, K. Kinetic and Mechanistic Analysis of Dibenzothiophene Hydrodesulfurization on Ti-SBA-15–NiMo Catalysts. ***Energy & Fuels*** 2018, *32* (11), 11383–11389. (ACS_IF=3.024, Q2).

- Kazeem, T. S.; Lateef, S. A.; Ganiyu, S. A.; Qamaruddin, M.; **Tanimu, A.**; Sulaiman, K. O.; Sajid Jillani, S. M.; Alhooshani, K. Aluminium-Modified Activated Carbon as Efficient Adsorbent for Cleaning of Cationic Dye in Wastewater. ***J. Clean. Prod***. 2018, *205*, 303–312. (Elservier_IF=5.651, Q1).
- **Tanimu, A.**; Jaenicke, S.; Alhooshani, K. Heterogeneous Catalysis in Continuous Flow Microreactors: A Review of Methods and Applications. ***Chem. Eng. J***. 2017, *327*, 792–821. (Elservier_IF=6.735, Q1).
- Ganiyu, S. A.; Alhooshani, K.; Sulaiman, K. O.; Qamaruddin, M.; Bakare, I. A.; **Tanimu, A.**; Saleh, T. A. Influence of Aluminium Impregnation on Activated

Carbon for Enhanced Desulfurization of DBT at Ambient Temperature: Role of Surface Acidity and Textural Properties. ***Chem. Eng. J***. 2016, *303*, 489–500. (Elservier_IF=6.735, Q1).